International Journal of Acoustics and Vibration

A quarterly publication of the International Institute of Acoustics and Vibration

Volume 20, Number 1, March 2015

EDITORIAL

ARTICLES

INFORMATION

Editor's Space

22nd International Congress on Sound and Vibration (ICSV22)

It is our great pleasure to invite you and your accompanying persons to participate in the 22nd International Congress on Sound and Vibration (ICSV22), to be held from 12 to 16 July 2015 at Palazzo dei Congressi, Florence, Italy.

The ICSV22 is jointly organized by the International Institute of Acoustics and Vibration (IIAV) and the Acoustical Society of Italy (AIA), in cooperation with the National Research Council of Italy (IMAMOTER Institute) and the University of Florence.

Almost 1250 abstracts in the field of acoustics, noise, sound, and vibration from 64 countries have been accepted for presentation. Half of them are coming from Europe, 450 from Asia, 130 from North and Latin Americas, and the remaining from Australia, New Zealand, and Africa. The attendance of so many scientists and engineers around the world is an important opportunity for all participants to establish new collaborations, to exchange ideas, and to share their research results. With the purpose of collecting high-level scientific contributions, the peer review of full papers was offered to all the authors; therefore, more than 200 full papers are now under the peer-review process.

Florence, the magnificent renaissance city situated in the heart of Tuscany, ranked as one of the most beautiful cities in the world, easy-to-reach from various international airports, and very well connected by plane and high speed trains to all the main Italian and European cities, promises to be the perfect place for hosting ICSV scientific and social activities.

The venue of ICSV22 is a functional congress centre located walking distance from all the cultural attractions in Florence like Piazza della Signoria with the monumental city hall Palazzo Vecchio, the Uffizi Gallery, Duomo Square with the Cathedral of Santa Maria del Fiore, the Baptistery and the Giotto Tower, the medieval bridge Ponte Vecchio, and Accademia Gallery that holds Michelangelo's David, which is probably the most famous sculpture in the world.

The ICSV22 Scientific Programme is structured in 14 Subject Areas, covering traditional ICSV topics such as active noise and vibration control, signal processing and simulation, and machinery noise and vibration, as well as topics on environmental noise, vibration, and soundscape, occupational noise, and underwater and maritime noise. One subject area of the Scientific Programme addresses European projects, international projects, and education. The ongoing projects in different fields of acoustics and vibration will be presented, and one will be able to find information and partnerships for the next calls. The Scientific Programme will be enriched by seven distinguished plenary lectures: Dick Botteldooren, *Modeling and Monitoring the Effects of Environmental Sound in Private and Public Space*, Kirill Horoshenkov, *Porous Material Characterization via Acoustical Methods*, Roberto Pompoli, A*coustics of Italian Opera Houses: A Cultural Heritage*, Wim Van Keulen, *Experiencing Noise-Reducing Pavements*, Otto Von Estorff, *Recent Developments of BEM and FEM and Their Application to Real Life Acoustic Problems*, Lily M. Wang, *Room Acoustics Effects on Speech Comprehension of English-as-Second-Language Talkers and Listeners versus Native-English-Speaking Talkers and Listeners*, Semyung Wang, *Sound Focusing and its Practical Applications*.

Students and young experts in sound and vibration are especially welcome at ICSV22; they can find reduced fees, a best paper award, and other grants organized specifically for them. A scientific session on "movida" and noise control in young places of cities is part of the programme, and social activities and events are planned for young delegates, including sets of jazz and rock music performed by young acousticians from all over the world.

The ICSV22 Technical Exhibition is an interesting and important part of the Congress. It includes more than 40 exhibition spaces, where major companies will show their newest equipment, software, and materials. Technical workshops and technical visits will be added to the scientific programme.

During the day at ICSV22, many social and cultural activities are planned for all participants. Additional opportunities are available to better enjoy Florence and Tuscany. A large variety of pre- and post-congress tours to discover Florence, Tuscany, and the most artistic and cultural treasurers in Italy are available for all the ICSV22 delegates and accompanying persons. A special musical programme is provided for entertainment during the social and celebrative events, and many options are given to delegates to plan their own stay and visits including shopping in Florence, the capital of Italian fashion, and a visit to EXPO 2015 in Milan, one of the top international attractions of this year.

Along with the IIAV officers and the AIA Board, we hope you can attend ICSV22 and experience the cultural heritage of Florence.

We look forward to welcoming you in Florence this July.

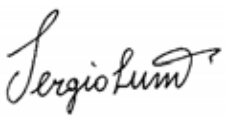

Eleonora Carletti **Sergio Luzzi**

ICSV22 General Chairs

Per Brüel's 100th Anniversary

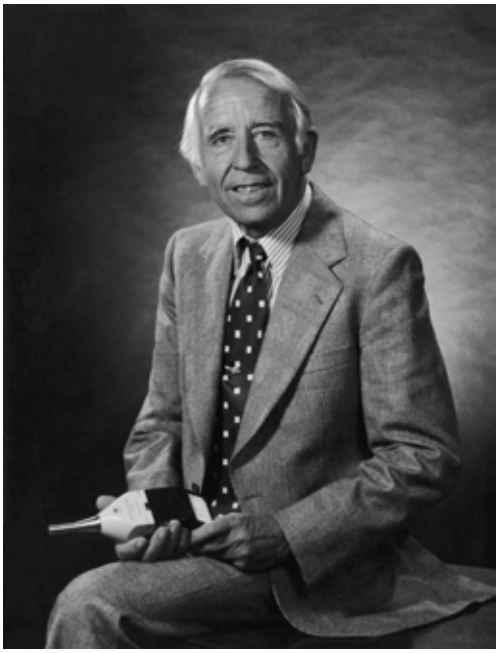

Per Brüel will celebrate his 100th birthday on March 6, 2015. The officers, directors and members of the International Institute of Acoustics and Vibration (IIAV) are honored to recognize the many pioneering contributions made by Per Brüel to the measurement of sound and vibration. He and the remarkable company he cofounded, Brüel & Kjær, are known all over the world. Per Vilhelm Brüel was born in Copenhagen, Denmark on March 6, 1915, but he attended school in the southern part of Jutland. In 1932, he went to college at the Polytechnic School (now the Danish Technical University) in Copenhagen studying physics and electronics and graduating with a master's degree in 1939. During his studies, he became the assistant to the famous professor, P. O. Pedersen, who together with Valdemar Paulsen created the world's first tape recorder. Dr. Brüel was drafted into the Danish Army in 1939 and constructed, at the military laboratory, the first acoustical analyser with a constant percentage bandwidth.

During college, Per Brüel met Viggo Kjær and they became lifelong friends. They decided to set up a company to develop instruments for acoustical measurements. This company, Brüel & Kjær, officially started in November 1942. However, there was a shortage of copper wires after the German occupation of Denmark. This was solved by taking some from a thick communications cable running under the sea from Copenhagen to Berlin, thus disrupting German communications. During the rest of the World War II, because of the German occupation of Denmark, Brüel had to spend most of the time in Sweden. Per Brüel was a close friend of Niels Bohr who was also living in Sweden during the war. Brüel would travel back to Denmark from time to time during this period and hide some of Bohr's documents on quantum physics among his own doctoral thesis papers on room acoustics which he was carrying back to his university. Brüel worked for a few years in the acoustical building material field in Sweden and he established the first acoustical laboratory in the Sweden at Chalmers Technical University in Gothenburg in 1944. The Brüel & Kjær company developed slowly in the period from 1942 to 1948 with the design and production of some new acoustical instruments. But in 1948, Brüel & Kjær purchased its first premises in Naerum, 15 km north of Copenhagen, and the company started to grow. In the Brüel & Kjær organization, Per Brüel took care of the development of new ideas, ran the feasibility laboratory and was in charge of sales. Viggo Kjær was responsible for all of the production planning, economics, financing, and staff etc.

In the 1950s, 1960s and 1970s, the Brüel & Kjær Company expanded rapidly and developed a whole range of sound and vibration instruments, including logarithmic level recorders, signal generators, frequency analyzers, measurement microphones, pre-amplifiers, calibrators, accelerometers, tapping machines and later digital parallel analyzers and dual-channel FFT analyzers capable of measuring sound intensity. By the late 1980's the company had the yearly turnover of 1 billion DKK (US$ 125,000,000) and the staff included 3,200 people. In a few short years the company had grown from modest beginnings to become the world leader in manufacturing and sale of acoustical instruments.

In the early days, Per Brüel personally delivered some instruments to customers in Denmark and Sweden on his Nimbus motorcycle. As the company expanded, Brüel & Kjær needed cars for deliveries and by the 1980's it had 30 company cars. Later with customers in Europe and further afield, airborne deliveries became necessary. Eventually Brüel & Kjær had two Piper Aztecs and two Beechcraft King Airs. Per Brüel personally took delivery of some of these aircraft from Wichita, Kansas and along with company pilots made instrument deliveries to customers. Per Brüel became such an enthusiastic pilot that, although Viggo Kjær used a bicycle to commute to work, Per Brüel used a company aircraft to commute from his summer home on Anholt Island.

In the late 1980's, due to overinvestment in a whole range of new acoustical instruments and the unexpected collapse of the Soviet Union, Brüel & Kjær became unprofitable. The subsequent loss of profitable markets in that country and other Eastern European countries had a strong negative financial effect and in 1992 Brüel & Kjær was sold to a German holding company, AGIV. It was subsequently split into several separate companies although with Brüel & Kjær Sound and Vibration Measurements A/S maintaining the core sound and vibration business. AGIV formed the Spectris Division to include Brüel & Kjær, which is profitable again and owned by a British company now operating under the name of Spectris.

Per Brüel did not stop his work on developing sound and vibration instruments after the sale of Brüel & Kjær. In 1992, he formed Brüel Acoustics and in 1994, Dr. G. Mario Mattia and Dr. Per V. Brüel founded Brüel Acoustics Srl in Rome, Italy. In the beginning, Dr. Brüel continued his development work during a five-year period of non-competition. The development work is still going on and the product range includes new instruments and sound absorbers. Per Brüel has many honors including six honorary doctorates. He was awarded the position of honorary fellow of the IIAV at the Sixth International Congress on Sound and Vibration (ICSV6) in Copenhagen in 1999.

Malcolm J. Crocker
Editor in Chief

Vibration Monitoring for Defect Diagnosis on a Machine Tool: A Comprehensive Case Study

Mouleeswaran Senthilkumar, Moorthy Vikram and Bhaskaran Pradeep

Department of Production Engineering, PSG College of Technology, Coimbatore 641 004, India

(Received 31 July 2012; revised 17 December 2013; accepted 26 February 2014)

Vibration monitoring and analysis of machine tools are carried out in industry to reduce maintenance cost and downtime. In this case study, the application of vibration monitoring and analysis was carried out on a lathe. The characteristic frequencies of tapered roller bearings, gear mesh frequencies, and belt drive frequencies were found to locate the source of vibration. Multi-harmonics of fundamental defect frequencies were observed. From the real-time observation, experimental prediction of defects has been found to be correct and accurate. This case study shows that vibration analysis plays a vital role in monitoring the condition of the machine tool.

NOMENCLATURE

N_b	Number of rollers
n	Revolutions per minute
D	Outer diameter, mm
d	Inner diameter, mm
T	Width, mm
C	Dynamic load rating, kN
C_o	Static load rating, kN
P_u	Fatigue load limit, kN
m	Mass, kg
Z	Number of gear teeth
N	Gear speed, rpm
F_{gm}	Gear meshing frequency, Hz
F_b	Belt drive frequency, Hz
d_p	Pulley diameter, mm
N_p	Pulley speed, rpm
l_b	Belt length, mm

1. INTRODUCTION

Vibration analysis is a measurement tool used to identify, predict, and prevent failures in machine tools. It involves the trending and analysis of machinery performance parameters to detect and identify problems before failure and extensive damage can occur. If problems can be detected early when the defects are minor and do not affect performance, and the nature of the problem can be identified while the machine runs, then repair time can be kept to a minimum, resulting in reduced machinery downtime. Therefore, vibration analysis is a technique that is employed to track machine operating conditions and trend deteriorations so as to reduce maintenance costs as well as downtime.[1] The vibration analysis technique consists mainly of vibration measurement and its interpretation. The vibration measurement is done by picking up signals from machines by means of vibration measurements. The signals are then processed using an FFT analyser to obtain the frequency spectrum. The results are mainly interpreted by relating the measured frequencies with their relevant causes such as unbalance, misalignment, bearing defects and resonance, etc. A case study on vibration-based maintenance in paper mills has been presented to improve accuracy and effectiveness.[2]

There are many case studies on vibration monitoring and analysis of rotating machineries. Vibrations associated with rolling element bearings, especially ball bearings have been discussed extensively,[3] while applied statistical moments to bearings defect detection.[4] Two case studies present on the defect diagnosis of rolling element bearings.[5,6] Another case study has analysed the vibration of a centrifugal pump and investigated the spike energy of bearings in order to find out the source of the vibration.[7] In vibration analysis, an artificial neural network has also been employed to monitor and diagnose rolling element bearings.[8] In vibration diagnosis, it is found that not only rolling elements but other sources of vibration exist as well. Vibration analysis of a motor-flexible coupling-rotor system subjected to misalignment and unbalance has been studied extensively.[9,10] Characteristics of the torsional vibrations of an unbalanced shaft were also analysed in another study.[11]

This case study analyses the vibration produced in a lathe during the real operation at different machining conditions. The study has been made to identify defects in three major sources of vibration, namely, rolling element bearings, gears, and belt drives.

2. EXPERIMENTAL SETUP AND VIBRATION MEASUREMENT

Experiments on PSG 141 lathes have been conducted using the accelerometer, and these experiments have discovered the vibrations that formed. The technical details of the lathe and the experimental conditions are as follows:

Machine tool :	PSG 141 lathe
Machine speed (rpm) :	38 60 71 90 115 140 200 250 228 360 450 580 740 800 1150 1600
Power :	Std. motor for main drive 1.1/2.2 kW (For 16 speeds) 1440/2880 rpm, 415 V, 3 phase, 50 Hz, AC

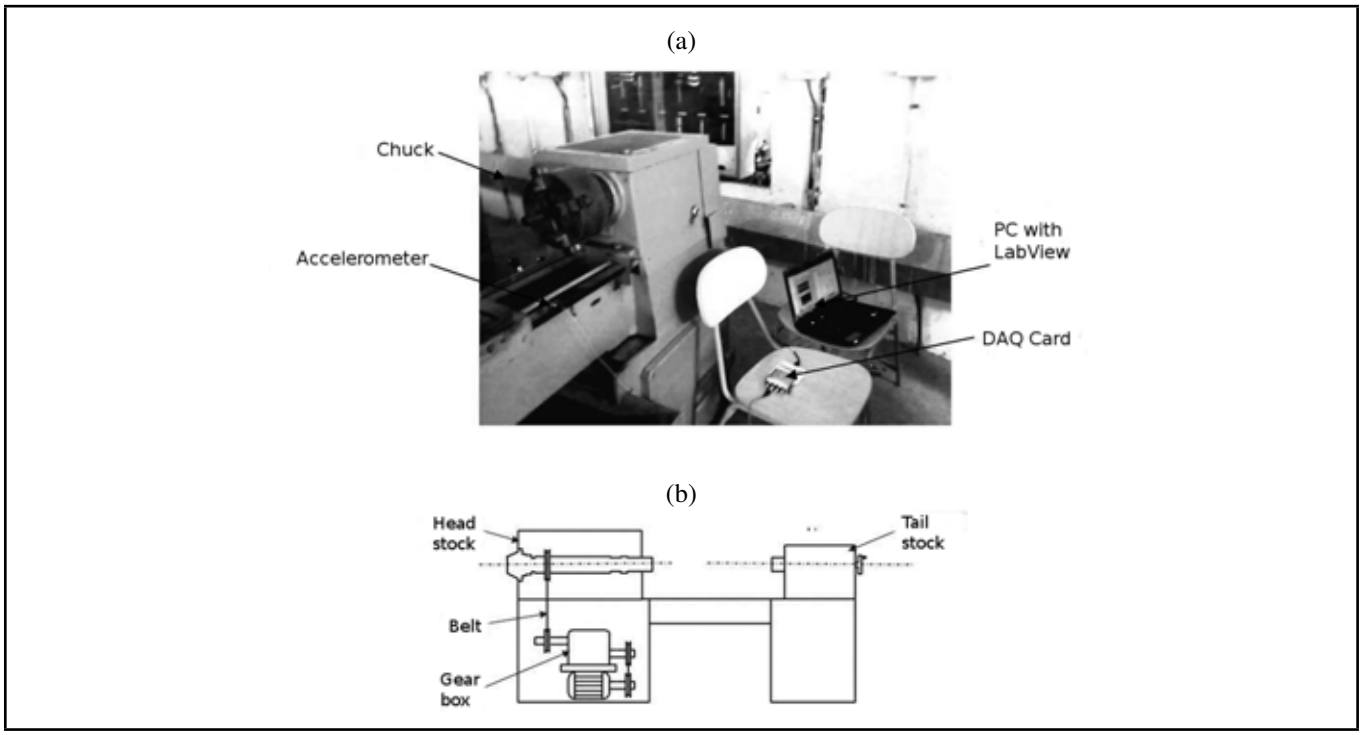

Figure 1. a) Experimental setup (Machine tool with data acquisition system); b) Schematic layout of drive system of the machine tool.

Height of centre :	177.5 mm
Admit between centres :	800 mm
Operation :	Turning
Component :	Cylindrical component of Figure 1 shows the experimental setup along with the position of the accelerometer. We collected the vibration data using the general purpose DYTRAN 3097A2 accelerometer with a sensitivity of 100 $\frac{mV}{g}$ in a frequency range of 0.3 Hz–10 kHz. Vibration measured in the vertical directions was dominant compared with the other two directions; hence they are only used to characterize the health of the machine tool. The accelerometer signals were taken to PC via the NI 9234 data acquisition card system using LabVIEW software.
	diameter 25 mm and length 70 mm
Depth of cut :	0.5 mm

The vibration of the machine tool is measured in three different locations: the lathe bed (simply supported), the head stock (bearing mountings), and the compound rest (tool and work piece interaction). These locations are vibration prone areas and result in higher vibration than other locations. The measurement is first taken in the lathe bed for different speeds. The peak frequencies appeared in the amplitude-versus-frequency spectrum, and all the speeds measured are the same and are found to be 50 Hz, 100 Hz, 150 Hz, 200 Hz, 350 Hz, 400 Hz and 450 Hz. The time-domain and frequency-domain data at 90 rpm and 800 rpm are shown in Figs. 2-5.

The frequency spectrums shown in Figs. 6-7 were taken on the head stock of the lathe. The peak frequencies obtained for four different spindle speeds (90, 200, 450 and 800 rpm) are found to be 70 Hz and 220 Hz, whereas the peak frequencies obtained for 1600 rpm are 160 Hz, 220 Hz, and 270 Hz.

Similarly, the vibration data for the compound rest was taken and is shown in Figs. 8-9. The peak frequencies that appeared for all the spindle speeds (90 rmp, 200 rmp, 450 rmp, 800 rmp, and 1600 rpm) are the same and are found to be 50 rmp, 100 rmp, 150 rmp, 250 rmp, 350 rmp, and 400 Hz.

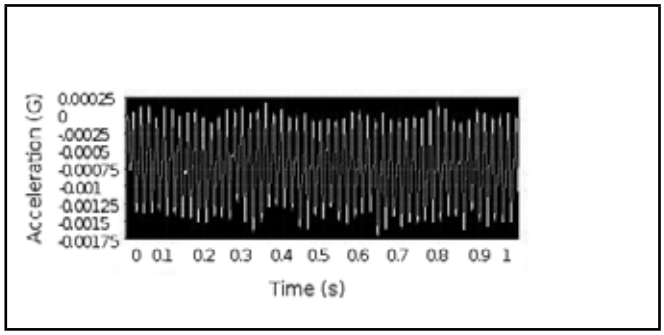

Figure 2. Time domain data of the lathe bed at 90 rpm.

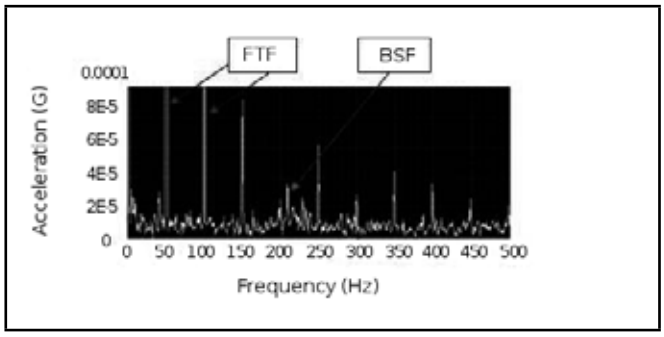

Figure 3. Frequency spectrum of the lathe bed at 90 rpm.

3. RESULTS AND DISCUSSION

Forces generated within the machine cause vibration. Sources of vibration in a typical machine tool like a lathe includes misalignment of couplings, bearings, unbalance of rotating components, looseness, deterioration of rolling element

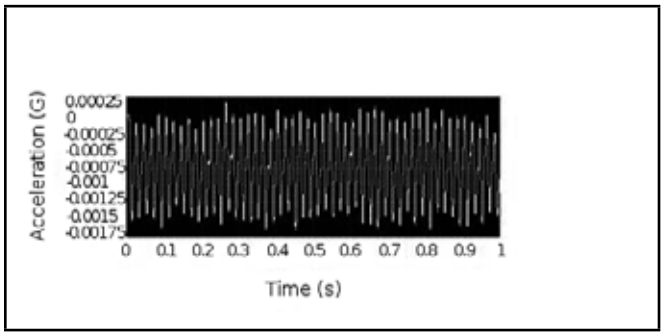

Figure 4. Time domain data of the lathe bed at 800 rpm.

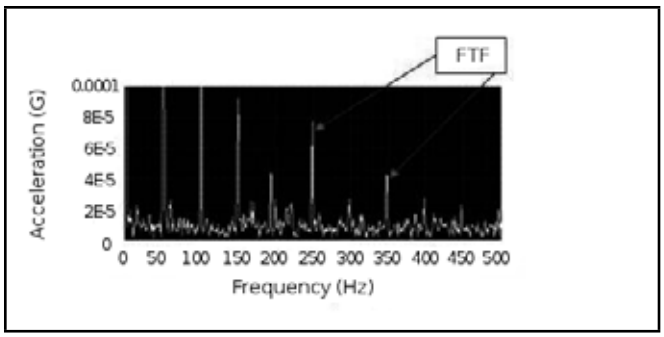

Figure 5. Frequency spectrum of the lathe bed at 800 rpm.

bearings, gear wear, resonance, and the eccentricity of rotating components such as V-pulleys or gears, etc. Therefore, it is important to calculate the characteristic frequencies of the three major sources of vibration in a machine tool, namely, the tapered roller bearing, the gear mesh, and the belt drive. The calculated characteristic frequencies are attempted to be matched with experimental peak frequencies. The faults in these elements caused peaks to develop at their characteristic frequencies, which indicate their possible presence. Referring to Fig. 1b, the belt drive connecting the motor and gear box provides a gear reduction ratio of 2.58. The drive connecting the gear box and the head stock results in a gear reduction ratio of 1.14.

3.1. Tapered Roller Bearing Defect Frequencies

Two tapered roller bearings are each installed at the front and rear ends of the lathe spindle. The front end of the spindle is fitted with the 32212 J2/Q bearing, and the rear end is fitted with the 32209 J2/Q bearing. Figure 10 shows the rolling el-

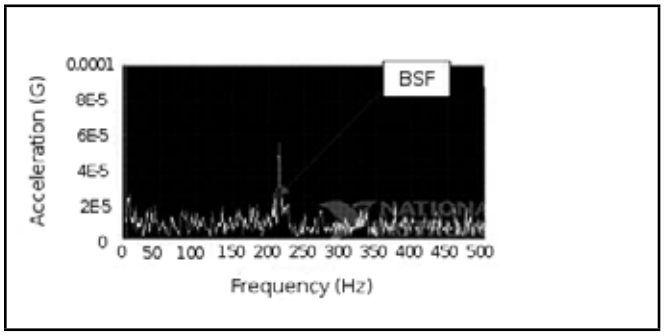

Figure 6. Frequency spectrum of the headstock at 90 rpm.

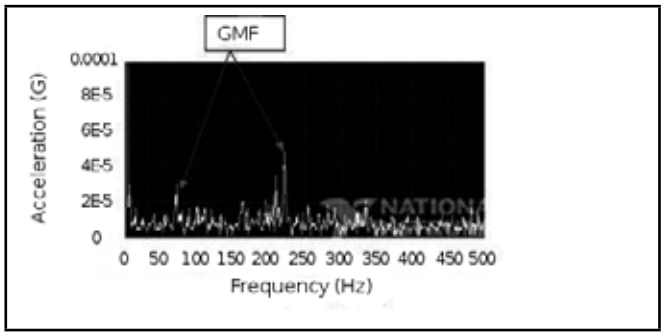

Figure 7. Multi-harmonics of the bearing defect frequencies at 450 rpm.

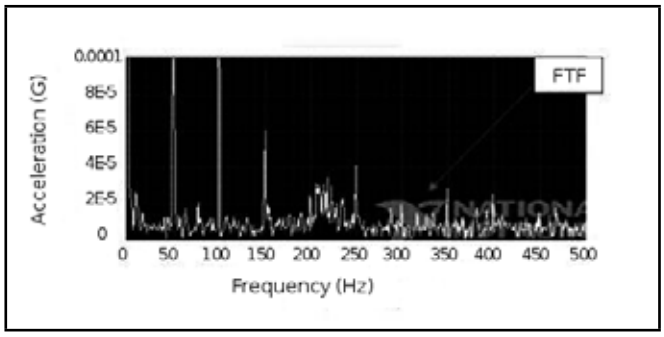

Figure 8. Frequency spectrum of the compound rest at 90 rpm.

ement bearing geometry. The main geometric dimensions are listed in Table 1. In a previous study, rolling element bearing defect frequencies are found out by using the Eqs. (1)-(4):[7]
Ball pass frequency of inner race way (BPFI):

$$\text{BPFI} = \left(\frac{N_b}{2} + 1.2\right) n, \text{Hz}. \tag{1}$$

Ball pass frequency of outer race way (BPFO):

$$\text{BPFO} = \left(\frac{N_b}{2} - 1.2\right) n, \text{Hz}. \tag{2}$$

Ball spin frequency (BSF):

$$\text{BSF} = \frac{1}{2}\left(\frac{N_b}{2} - \frac{1.2}{N_b}\right) n, \text{Hz}. \tag{3}$$

Fundamental train frequency of the cage or retainer (FTF):

$$\text{FTF} = \left(\frac{1}{2} - \frac{1.2}{N_b}\right) n, \text{Hz}. \tag{4}$$

The basic assumptions made are: all rollers are of equal diameter, pure rolling contact exists between rollers and the outer

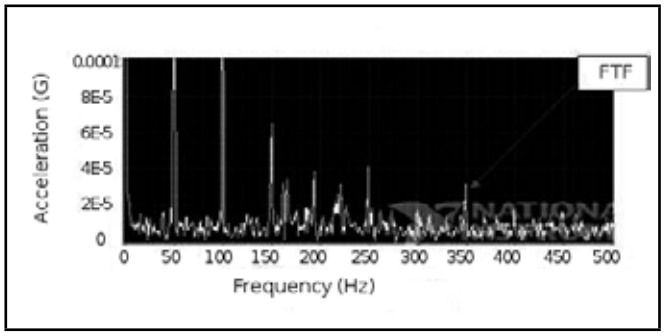

Figure 9. Frequency spectrum of the compound rest at 800 rpm.

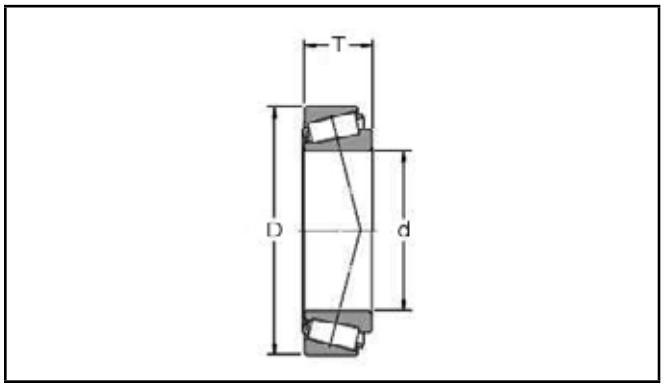

Figure 10. Rolling element bearing geometry.

Table 1. Geometric dimensions of the bearings of the head stock spindle.

Parameters	Front end 32212 J2/Q	Rear end 32209 J2/Q
D	110	85
d	60	45
T	29.75	24.75
N_b	19	19
C	146	91.5
C_o	160	98
P_u	18.6	11
m	1.15	0.58

race, no slipping occurs between the shaft and the bearing, and the outer race is stationary. Both these bearings have a contact angle of 0°. Also, as there is a very small thrust; it is neglected.

The spectrums were captured, and the certain defect related frequencies of the bearings have been identified and encircled in Table 2. Hence we tried to identify any such peaks there are in the spectrum. The harmonics (sub & super) of different spindle speeds are found out and tabulated in Table 2. It is found that the calculated fundamental bearing defect frequencies for the different speeds are found to be deviated from the experimentally measured peak frequencies. However, the superharmonics (1.5X and 2.5X) of the fundamental train frequency of the retainer were found to match with the peak frequencies at lower speeds. Subharmonics of the same were also found to match with the peak frequencies at higher speeds. Also, Figs. 3, 5, 8, and 9 indicate that the retainer is defective; hence, we anticipated that the retainer or cage would be defective.[7] So, the bearings were dismantled and examined. We identified the front end bearing as having defective retainers.

3.2. Gear Mesh Frequencies in Gear Box and Headstock

Apart from bearing characteristic frequencies, there are many other peak frequencies found from the spectrums. Therefore, it was necessary to track other defective elements like gears in the gear box and head stock. Fig. 11a shows the gear train arrangement in the lathe under study, whereas Fig. 11b depicts the inner view of the gear box. The identification of possible gear problems is fairly easy since the most common vibration frequencies will be equal to the harmonics of the gear meshing frequency. The gear meshing frequency (F_{gm}) is referred to as:[12]

$$F_{gm} = \frac{ZN}{60}, \text{Hz}. \tag{5}$$

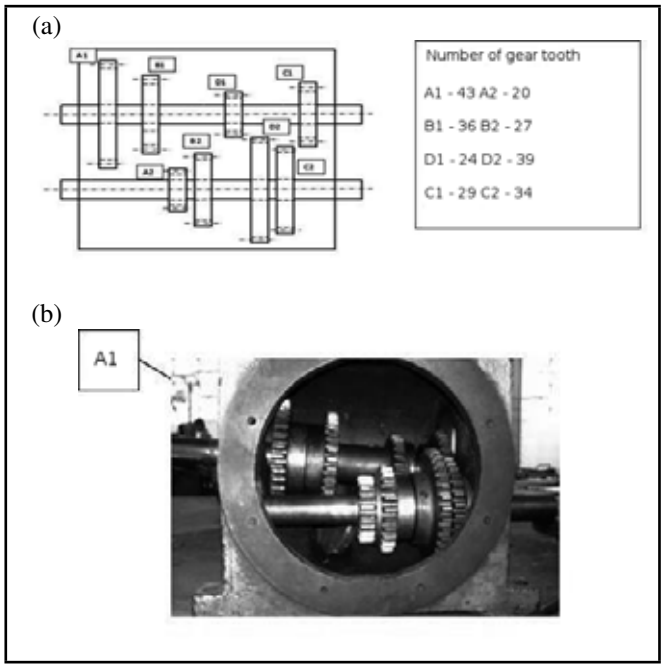

Figure 11. a) Gear train layout of main gear box; b) Inner view of main gear box.

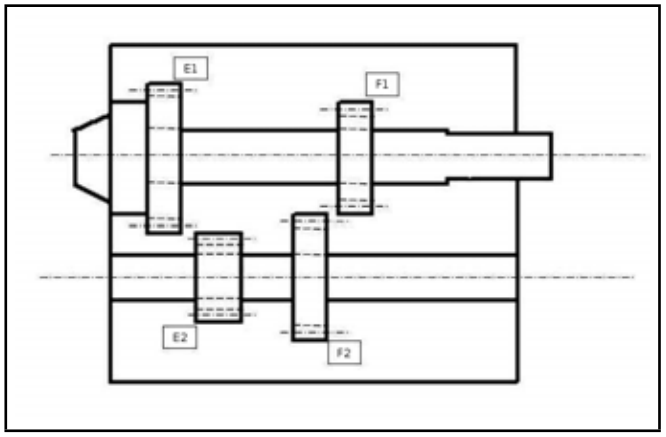

Figure 12. Gear box layout in head stock.

The experimental data at differetnt spindle speeds are tabulated in Table 3. Inspection of Table 3 shows that 150 Hz is equivalent to the 0.5X at 90 rpm and 0.25X at 200 rpm. At different speeds, the subharmonics of the gear meshing frequency also match with the peak frequencies. This indicates that the gears in the gear box are defective. Further evidence is required to identify the exact defective gear pairs. Table 4 depicts how the power and speed flow from the drive motor to the spindle. Different spindle speeds have been achieved by engaging different sets of gears in the gear box and the head stock as shown in Table 4. This will be helpful in identifying the faulty gear pairs that develop peak frequencies. Figure 12 shows the gear train arrangement in the head stock. Table 5 shows the harmonics of the gear meshing frequncy of the head stock.

From the Table 5, we observed that the subharmoincs of the gear mesh frequencies match with the peak frequenices at almost all speeds. It cleary depicts that the gears are defective in the head stock as well.

Table 2. Multi-Harmonics of bearing defect frequencies.

Defect	Subharmonics			Fundamental frequency (Hz)	Superharmonics		
	Spindle speed: 90 rpm						
	0.25X	**0.5X**	**0.75X**	**1X**	**1.5X**	**2X**	**2.5X**
BPFI	240.75	481.5	722.25	963	1444.5	1926	2407.5
BPFO	186.75	373.5	560.25	747	1120.5	1494	1867.5
BSF	106.16	212.32	318.48	424.65	636.97	849	1061.62
FTF	9.82	19.65	29.48	39.31	**58.96**	78.62	**98.27**
	Spindle speed: 200 rpm						
BPFI	535	1070	1605	2140	3210	4280	5350
BPFO	415	830	1245	1660	2490	3320	4150
BSF	235.82	471.84	707.6	943.68	1415.52	1887	2359.2
FTF	21.84	**43.68**	65.52	87.36	131.04	174	218.4
	Spindle speed: 450 rpm						
BPFI	1203.75	2407.5	3611.25	4815	7222.5	9630	12037.5
BPFO	933.75	1867	2801	3735	5602	7470	9338
BSF	530	1061	1592	2123.28	3184	4246	5308
FTF	**49.14**	**98.25**	**147.42**	196.56	294.84	**393.12**	491.4
	Spindle speed: 800 rpm						
BPFI	2140	4280	6420	8560	12840	17120	21400
BPFO	1660	3320	4980	6640	9960	13280	16600
BSF	943.68	1887.3	2831	3774.7	5662	7549	9436
FTF	87.36	174.7	262	**349.44**	524.16	698.8	873.6
	Spindle speed: 1600 rpm						
BPFI	4280	8560	12840	17120	25680	34240	42800
BPFO	3320	6640	9960	13280	19920	26560	33200
BSF	1887	3774	5662	7547	11324	15098	18873
FTF	174.7	**349.44**	524.16	698.08	1048.32	1397	1747

Table 3. Multi-harmonics of gear mesh frequencies in the gear box.

Spindle	**Subharmonics**				**Superharmonics**		
speeds(rpm)	**0.25X**	**0.5X**	**0.75X**	**1X**	**1.5X**	**2X**	**2.5X**
90	79	**158**	237.10	316.14	474.2	632.2	790.3
200	**158**	316.14	474.2	632.2	948.3	1264.5	1580.7
450	**92.98**	185.9	278.9	371.9	557.9	743.8	929.8
800	90.66	181.3	**271.9**	362.6	543.9	725.28	906
1600	181.32	362.6	543.9	725.29	1087	1450	1813

Table 6. Multi-harmonics of belt drive frequencies.

Spindle	**Subharmonics**				**Superharmonics**		
speeds (rpm)	**0.25X**	**0.5X**	**0.75X**	**1X**	**1.5X**	**2X**	**2.5X**
90	36.6	73.3	110	**146.6**	220	293.3	366
200	73.4	**146.8**	**220.2**	293.6	440.5	527	659
450	29.1	**58.2**	87.3	116.5	174.7	233	291
800	**50.8**	**101.7**	152.6	203.5	305.2	407	508
1600	**101**	203	305	407	610	814	1017

3.3. Belt drive frequencies

In order check whether or not the belt drive is the source of some vibrations, the belt drive system was also analysed. Vibration due to belt problems implies that there is something physically wrong with the belts themselves such as hard spots, missing chunks, or other belt deformities that produce dynamic forces with characteristic vibration frequencies, which are directly related to the rotating speed (rpm) of the belts.[13] Belt drive frequency is determined from:

$$F_b = \frac{\pi d N_p}{l_b}, \text{Hz}. \tag{6}$$

From the harmonics of the belt drive frequencies as given in Table 6, it was observed that 0.5X and 0.75X of 200 rpm appeared at 150 Hz and 220 Hz, 0.25X and 0.5X at 800 rpm both appeared at 50 Hz, and 0.25X of 1600 rpm appeared at 100 Hz. Hence a defect in the belt has been found out, and the defective belt is shown in Fig 13.

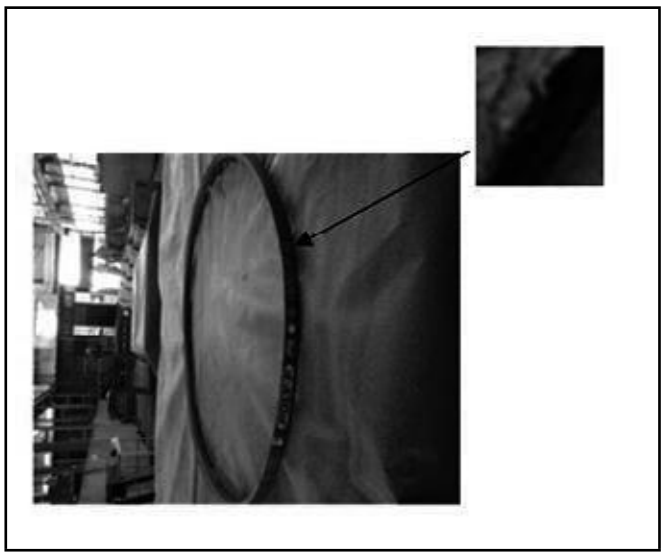

Figure 13. Defective belt in the drive system.

Table 4. Drive (gear pair) engagement for different spindle speeds.

Input Motor speed (rpm)	Engagement of 1st Belt drive	Gears Engaged in Gear Box	Engagement of 2nd Belt drive	Gears Engaged in Head Stock	Spindle Speed (rpm)
1440	✓	C1-C2	✓	E1-E2	90
2880	✓	C1-C2	✓	E1-E2	200
2880	✓	A1-A2	✓	F1-F2	450
1440	✓	D1-D2	✓	F1-F2	800
2880	✓	D1-D2	✓	F1-F2	1600

Table 5. Multi-harmonics of gear mesh frequencies.

Spindle	Subharmonics				Superharmonics		
speeds(rpm)	0.25X	0.5X	0.75X	1X	1.5X	2X	2.5X
90	38.28	**76.56**	114.84	**153.13**	229.69	306.26	382.82
200	**76.56**	**153.13**	229.7	306.27	459.4	612.54	765.675
450	**113.91**	227.82	**341.73**	455.64	683.46	911.28	1139.1
800	198.98	**397.9**	596.96	795.95	1193.92	1591.9	1989.8
1600	**397.97**	795.95	1193.92	1591.9	2387.8	3183.8	3979.75

4. CONCLUSION

In this study, the defect diagnosis of a machine tool (lathe) using the spectrum analysis technique is carried out. The bearing defect frequencies were evaluated and compared with the measured data, which indicates defects in the cage of the tapered roller bearing. Harmonics of gear mesh frequencies were calculated, and it was discovered that defective gear pairs in the gear box and the head stock existed. By calculating the belt drive frequency and its harmonics, defects in the belt drive were also confirmed. Hence, a recommendation of dismantling the lathe drive system and the replacement of the bearing, the defective gear pairs, and the belt drive was sent to the maintenance group.

REFERENCES

[1] Renwick, J. T. and Babson, P. E. Vibration analysis-a proven technique as a predictive maintenance tool, *IEEE Tran. Ind. Appl.*, **21**(2), 324–32, (1985).

[2] Al-Najjar, B. Accuracy, effectiveness and improvement of vibration-based maintenance in paper mills: case studies, *J. Sound Vib.*, **229**(2), 389–410, (2000).

[3] Gohar, R. and Akturk, N. Vibrations associated with ball bearings, *ImechE*, 43–64, (1998).

[4] Martin, H. R. and Honarvar, F. Application of statistical moments to bearing failure detection, *Applied Acoustics*, **44**, 67–77, (1995).

[5] Heng, R. B. W. and Nor, M. J. M. Statistical analysis of sound and vibration signals for monitoring rolling element bearing condition, *Applied Acoustics*, **53**(1-3), 221–226, (1998).

[6] Orhan, S., Akturk, N., and Celik,V. Vibration monitoring for defect diagnosis of roller element bearings as a predictive maintenance tool: comprehensive case studies, *NDT&E International* **39**, 293–298, (2006).

[7] Fathi, N and Mayo, F. Beating phenomenon of multi harmonics defect frequencies in rolling element bearing: case study from water pumping station, *World Academy of Science, Engineering and Technology*, **57**, (2009).

[8] Alguindigue, I. E., Buczak, L. A., and Uhrig, R.E. Monitoring and diagnosis of rolling element bearings using artificial neural networks, *IEEE Trans Ind Electron*, **40**(2), 209–17, (1993).

[9] Xu, M. and Marangoni, R. D. Vibration analysis of a motor-flexible coupling-rotor system subject to misalignment and unbalance, part II: experimental validation. *J. Sound Vib.*, **176**(5), 681–694, (1994).

[10] Senthil kumar, M. and Sendhil kumar, S. Effects of misalignment and unbalance in a vibration analysis of rotor-bearing systems, *National Journal of Technology*, **8**(1), (2012).

[11] Haung, D. G., Characteristics of torsional vibrations of a shaft with unbalance, *J. Sound Vib.*, **308**, 692–698, (2007).

[12] Dalpiaz G., Rivola A. and Rubini Dynamic modelling of gear systems for condition monitoring and diagnostics, *Proc. Congress on Technical Diagnostics*, Bologna, Italy, (1996).

[13] Cornelius, S. and Paresh, G. Practical Machinery Vibration Analysis and Predictive Maintenance, *Elsevier*, (2004).

Free Vibration Analysis of a Rectangular Duct with Different Axial Boundary Conditions

Pruthviraj Namdeo Chavan and B. Venkatesham

Department of Mechanical Engineering, Indian Institute of Technology Hyderabad, Ordnance Factory Estate, Yeddumailaram, 502205, A.P., India.

(Received 18 August 2012; revised 27 March 2014; accepted 7 May 2014)

This paper describes the free vibration analysis of a rectangular duct by using the Rayleigh-Ritz method. Static beam functions are used as admissible functions in the Rayleigh-Ritz method. These basis functions are the static solutions of a point-supported beam under a series of sinusoidal loads. The unique advantage of using this method is that it allows for the consideration of different axial boundary conditions of a duct. Computational results are validated with existing literature data for a simply supported rectangular duct and the finite element method (FEM) for other axial boundary conditions. A validated analytical model is used for generating natural frequency data for different dimensions of rectangular ducts. Further curve fitting has been done for the generated data, and an empirical relation has been presented to calculate the first fundamental natural frequency for different material properties of ducts and different axial boundary conditions, which can be used for any dimensions of the duct within the specified range.

1. INTRODUCTION

Heating, Ventilation, and Air Conditioning (HVAC) systems extensively use ducts of different sizes and shapes that are connected in series or in parallel for air-handling purposes. The most prominent duct shapes are circular, rectangular, and elliptical. Noise generated from air handling units propagates in the axial and transverse directions of a duct. Noise radiated from ducts in the transverse direction is called breakout noise. Rectangular ducts have the highest breakout noise compared to a circular duct's cross-section due to lower stiffness. The breakout noise from these ducts has an impact at lower frequencies. The coupling of acoustic duct modes and structural duct modes plays a critical role in generating noise in the transverse direction. The first step in understanding structural-acoustic coupling is to calculate the natural frequencies and mode shapes of the structural components. The research interest in this paper is the free vibration analysis of rectangular ducts.

Different methods have been proposed in literature for free vibration analysis of polygonal ducts. S. Azimi et al. and G. Yamada et al. used the receptance method.[1,2] H. P. Lee used the Rayleigh-Ritz method for calculating the natural frequencies and the mode shape of cylindrical polygonal ducts, in which sinusoidal functions are used as admissible functions.[3] T. Irea, et al. used the transfer matrix method for free vibration analysis of prismatic shells.[4] Sai Jagan Mohan et al. used the Finite Element Method (FEM) to calculate the duct natural frequencies and the mode shape.[5] They used group theoretical analysis to characterize duct modes. Existing literature results have only considered simply supported boundary conditions in the axial direction of the duct. According to current research, there is no work reported for the other axial boundary conditions. So in the present paper, the Rayleigh-Ritz method, which is capable of considering different axial boundary conditions, is used for calculating the natural frequencies of rectangular ducts.

A good amount of literature is available for the Rayleigh-Ritz methods with different admissible functions. Selection of proper admissible functions provides variation in the Rayleigh-Ritz method. Admissible function varies based on applications like rectangular plates, rectangular plates with intermediate supports, etc. Zhou Ding used the Rayleigh-Ritz method for natural frequency analysis of rectangular plates with a set of static beam functions as admissible functions.[6] D. Zhou et al. used a set of static beam functions for free vibration analysis of rectangular plates with intermediate supports.[7] In the present paper, rectangular ducts are modelled as unfolded plates with rotational springs, and the creases are modelled as intermediate supports. The set of static beam functions are extended for the rectangular ducts. In the Rayleigh-Ritz method, validity and accuracy are entirely dependent on the choice of the admissible functions.[8] These static beam functions are the static solutions of the point-supported beams under sinusoidal loads.

Calculated results from this method are validated with the data from the literature and with the FEM results. The validated analytical model is used to generate the engineering data for the rectangular ducts with different side ratios (height to width or width to height of the duct) and with different aspect ratios (perimeter of the duct cross section to length of the duct). These ratios are taken as four-step values (0.25, 0.5, 0.75, and 1). Further curve fitting has been done for generated engineering data results, and an empirical relation has been developed to calculate the first fundamental frequency. This empirical relation can be used to calculate the first fundamental frequency for any combination of an aspect ratio and a side ratio between a range of 0.25 to 1 with a prediction accuracy of 95%.

Figure 1 shows the rectangular duct with dimensions of L_1, L_2, and L_3 in X, Y, and Z directions, respectively. The reference coordinate system is also shown in Fig. 1.

2. THE RAYLEIGH-RITZ METHOD

The main advantage of this present Rayleigh-Ritz method with the static beam function as an admissible function is that

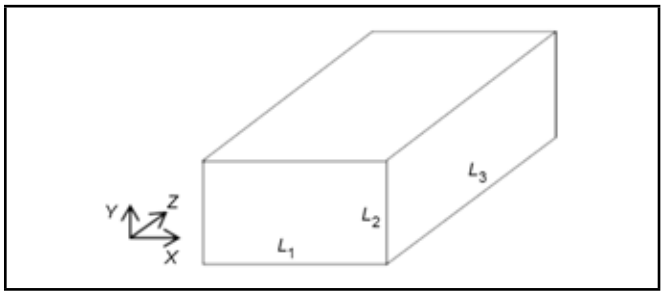

Figure 1. A schematic diagram of a rectangular duct.

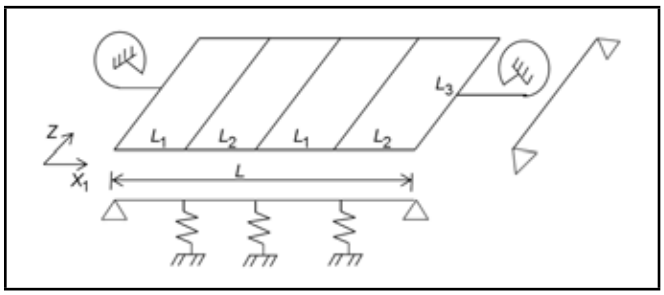

Figure 2. An unfolded plate representation of a simply supported rectangular duct.

it has the capability to choose boundary conditions in the axial direction. The different axial boundary conditions considered are Simple-Simple (S-S), Clamped-Clamped (C-C), Clamped-Simple (C-S), and Clamped-Free (C-F).

Figure 2 shows the unfolded representation of the rectangular duct shown in Fig. 1. It consists of four flat plates connected side-by-side with intermediate supports that are represented, and the ends with torsional springs as shown in Fig. 2. Thus, it can be approximated as a beam with three intermediate supports in the X_1-direction and a simple supported beam in the axial direction (Z-direction).

2.1. The Rayleigh-Ritz Approach

For the free vibration analysis of plate, the deflection w can be expressed as

$$w(x,y,t) = W(x,y)e^{i\omega t}; \tag{1}$$

where ω is the eigenfrequency of plate vibration, t is the time, and $i = \sqrt{-1}$. Assuming,

$$\xi = x/L; \qquad \eta = z/L^3. \tag{2}$$

The mod shape function $W(\xi,\eta)$ can be expressed in terms of the series function as follows,

$$W(\xi,\eta) = \sum_{m=1}^{\infty}\sum_{n=1}^{\infty} A_{mn}\phi_m(\xi)\psi_n(\eta); \tag{3}$$

where $\phi_m(\xi)$ and $\psi_n(\eta)$ are the admissible functions in the circumferential and axial directions, respectively. A_{mn} are unknown coefficients. By minimizing the total energy for thin plates as follows

$$\frac{\partial}{\partial A_{mn}}\left(U_{\max} - T_{\max}\right) = 0; \tag{4}$$

$U_{\max}$ and $T_{\max}$ are maximum potential and kinetic energies for the thin plates obtained by using the vibration theory of thin plates. Equation (4) leads to the eigenfrequency equation, which is given as

$$\sum_{m=1}^{\infty}\sum_{n=1}^{\infty}\left[C_{mnij} - \lambda^2 E_{mi}^{(0,0)}F_{nj}^{(0,0)}\right]A_{mn} = 0; \tag{5}$$

where

$$\begin{aligned} C_{mnij} &= E_{mi}^{(2,2)}F_{nj}^{(0,0)} + E_{mi}^{(0,0)}F_{nj}^{(2,2)}/\gamma^4 + \\ &\quad \nu\left(E_{mi}^{(0,2)}F_{nj}^{(2,0)} + E_{mi}^{(2,0)}F_{nj}^{(0,2)}/\gamma^2\right) + \\ &\quad 2(1-\nu)\left(E_{mi}^{(1,1)}F_{nj}^{(1,1)}/\gamma^2\right); \\ \lambda^2 &= \rho h\omega^2 L_3^4/H; \\ \gamma &= L/L_3; \\ E_{mi}^{(r,s)} &= \int_0^1 \left(d^r\phi_m/d\xi^r\right)\left(d^s\phi_i/d\xi^s\right)d\xi; \\ F_{nj}^{(r,s)} &= \int_0^1 \left(d^r\psi_n/d\eta^r\right)\left(d^s\psi_j/d\eta^s\right)d\eta; \end{aligned} \tag{6}$$

$\rho =$ density, $h =$ thickness, $L =$ perimeter of rectangular duct, and $H = Eh^3/(12*(1-\nu^2))$.

As discussed, the validity and accuracy of the Rayleigh-Ritz method entirely depends upon the choice of the admissible function. The appropriate admissible function should at least satisfy the geometrical boundary conditions and, if possible, all the boundary conditions. In the presented method, these admissible functions are taken as a set of static beam functions. So,

$$\begin{aligned} \phi_m(\xi) &= y_m(\xi); \\ \psi_n(\eta) &= y_n(\eta); \end{aligned} \tag{7}$$

$y_m(\xi)$ and $y_n(\eta)$ are the m^{th} and n^{th} static beam functions in the X_1 and Z directions, respectively. These functions satisfy the geometrical boundary conditions and the zero deflection condition at the line supports.

2.2. Static Beam Functions

The static beam functions for the rectangular plate with three intermediate supports in X_1-direction are given in the references.[7] The static beam function in the axial direction can be considered as the deflection of a beam with end supports.[6] The deflection $y(\xi)$ of the beam in the circumferential direction can be written as

$$y_m(\xi) = \sum_{k=0}^{3} C_k^m \xi^k + \sum_{j=1}^{3} P_j^m \frac{(\xi-\xi_j)^3}{6}U(\xi-\xi_j) + \sin(m\pi\xi). \tag{8}$$

The deflection $y(\eta)$ of the beam in the axial direction can be written as

$$y_n(\eta) = \sum_{k=0}^{3} C_k^n \eta^k + \sin(n\pi\eta); \tag{9}$$

where P_j^m $(j = 1,2,3)$ and C_k^m $(k = 0,1,2,3)$ are unknown coefficients, and $U(\xi-\xi_j)$ is a Heaviside function.

By observing Eqs. (8) and (9), the second series term is missing in Eq. (9) because the plate has intermediate supports in the circumferential direction and also continues in the axial direction.

The unknowns in Eqs. (8) and (9) can be uniquely decided by using the boundary conditions and zero deflection conditions at the intermediate supports. This can be written in the matrix form as $W(\xi,\eta) = \sum_{m=1}^{\infty}\sum_{n=1}^{\infty} A_{mn}\phi_m(\xi)\psi_n(\eta)$.

$$\begin{bmatrix} \mathbf{A} & \mathbf{D} \\ \mathbf{T} & \mathbf{G} \end{bmatrix} \begin{bmatrix} \mathbf{C}^m \\ \mathbf{P}^m \end{bmatrix} = \begin{bmatrix} \mathbf{R}^m \\ \mathbf{S}^m \end{bmatrix}; \tag{10}$$

where $\mathbf{A}$ is $J \times 4$ matrix, $\mathbf{T}$ is 4×4 matrix, and they refer to the first series terms of equations. $\mathbf{D}$ is $J \times J$ matrix, $\mathbf{G}$ is $4 \times J$ matrix, and they refer to the second series terms of the equation. $\mathbf{R}^m$ is $J \times 1$ matrix, $\mathbf{S}^n$ is 4×1 matrix, and they refer to the third term of the equation for the boundary conditions of the beam. $\mathbf{C}^m$ and $\mathbf{P}^m$ are unknown coefficient matrices as follows:

$$\mathbf{C}^m = \begin{bmatrix} C_0^m & C_1^m & C_2^m & C_3^m \end{bmatrix}^T;$$
$$\mathbf{P}^m = \begin{bmatrix} P_1^m & P_2^m & P_3^m \end{bmatrix}^T. \tag{11}$$

Generally $\mathbf{A}$, $\mathbf{D}$ and $\mathbf{R}^i$ matrices are given as

$$\mathbf{A} = \begin{bmatrix} 1 & \xi_1 & \xi_1^2 & \xi_1^3 \\ 1 & \xi_2 & \xi_2^2 & \xi_2^3 \\ \vdots & \vdots & \vdots & \vdots \\ 1 & \xi_J & \xi_J^2 & \xi_J^3 \end{bmatrix};$$

$$\mathbf{R}^m = \begin{bmatrix} -\sin(m\pi\xi_1) \\ -\sin(m\pi\xi_2) \\ \vdots \\ -\sin(m\pi\xi_J) \end{bmatrix};$$

$$\mathbf{D} = \begin{bmatrix} 0 & 0 & 0 & \cdots & 0 \\ \frac{(\xi_2-\xi_1)^3}{6} & 0 & 0 & \cdots & 0 \\ \frac{(\xi_3-\xi_1)^3}{6} & \frac{(\xi_3-\xi_2)^3}{6} & 0 & \cdots & 0 \\ \vdots & \vdots & \vdots & \vdots & \vdots \\ \frac{(\xi_J-\xi_1)^3}{6} & \frac{(\xi_J-\xi_2)^3}{6} & \cdots & \frac{(\xi_J-\xi_{J-1})^3}{6} & 0 \end{bmatrix}; \tag{12}$$

where J is the number of intermediate supports that are three in the circumferential direction and zero in the axial direction. So in the axial direction the matrices $\mathbf{A}$, $\mathbf{D}$, $\mathbf{G}$, $\mathbf{R}^m$, and $\mathbf{P}^m$ will be zero.

Clamped, simply supported, and free-boundary conditions are denoted by C, S, and F. The elements of the matrices $\mathbf{T}$, $\mathbf{G}$, and $\mathbf{S}_i$ according to the boundary conditions of the beam are

- $T_{11} = T_{22} = 1$, $S_2^n = -n\pi$ for the beam with C as the left end;
- $T_{11} = 1$, $T_{23} = 2$ for the beam with S as the left end;
- $T_{13} = 2$, $T_{24} = 6$, $S_2^n = (n\pi)^2$ for the beam with F as the left end;
- $T_{31} = T_{32} = T_{33} = T_{34} = 1$, $T_{42} = 1$, $T_{43} = 3$, $G_{3j} = (1-\xi_j)^3/6$, $G_{4j} = (1-\xi_j)^2/2$, $S_4^n = -n\pi(-1)^n$ for the beam with C as the right end;
- $T_{31} = T_{32} = T_{33} = T_{34} = 1$, $T_{43} = 2$, $T_{44} = 6$, $G_{3j} = (1-\xi_j)^3/6$, $G_{4j} = 1-\xi_j$ for the beam with S as the right end;
- $T_{33} = 2$, $T_{34} = 6$, $T_{44} = 6$, $G_{3j} = 1-\xi_j$, $G_{4j} = 1$, $S_4^n = (n\pi)^3(-1)^n$ for the beam with F as the right end.

Table 1. Comparison of the first five natural frequencies of a rectangular duct with S-S boundary conditions.

Sr. No.	Static Beam Method	Lee Paper[3] Results	Transfer Matrix Method	FEM Results
1	97.97	97.97	97.87	97.87
2	113.16	113.16	113.04	113.03
3	129.81	129.82	125.47	126.81
4	138.76	138.76	138.62	138.59
5	141.41	141.41	140.05	139.88

Table 2. Comparison of the first five natural frequencies of a rectangular duct with C-C boundary conditions.

Sr. No.	Static Beam Method	FEM Results
1	99.27	99.16
2	117.98	117.79
3	130.79	128.32
4	145.27	143.93
5	148.43	148.19

Table 3. Comparison of the first five natural frequencies of a rectangular duct with C-S boundary conditions.

Sr. No.	Static Beam Method	FEM Results
1	98.57	98.46
2	115.39	115.24
3	130.26	127.53
4	143.19	141.76
5	143.34	143.11

Table 4. Comparison of the first five natural frequencies of a rectangular duct with C-F boundary conditions.

Sr. No.	Static Beam Method	FEM Results
1	94.15	93.65
2	104.69	104.30
3	125.83	125.18
4	127.45	—
5	135.32	132.10

3. RESULTS AND DISCUSSIONS

To illustrate the validity and the accuracy of the methods, some numerical results have been presented and compared with the literature results and the FEM results. Lack of literature data for other than simply supported axial boundary conditions motivates validation with the results from the FEM analysis. Typical dimensions of duct and material properties used in the calculation are $L_1 = 0.4$ m, $L_2 = 0.3$ m, $L_3 = 1.5$ m, and the thickness $h = 0.005$ m. The material properties are: Young's modulus $E = 71$ GPa, Poisson's ratio $\nu = 0.29$, and density $\rho = 2770$ kg/m^3.

Tables 1 to 4 consist of comparisons of the natural frequency for a simple supported rectangular duct with aluminium materials. Table 1 shows the results comparison of different methods for an aluminium rectangular duct. As mentioned earlier, the Rayleigh-Ritz method with static beam functions as admissible functions is capable of incorporating other boundary conditions. These results are compared with the FEM analysis results. Tables 2, 3, and 4 show a comparison of the results for the different boundary conditions like C-C, C-S, and C-F, respectively for the aluminium rectangular duct.

FEM analysis has been carried out using commercial software (ANSYS),[9] in which shell elements are used with 30 elements per side. The Block Lanczos modal analysis scheme is used for calculating natural frequencies.

Results for the S-S axial boundary conditions are compared with the Lee paper, which also uses the Rayleigh-Ritz method but with different admissible functions.[3] The values match ex-

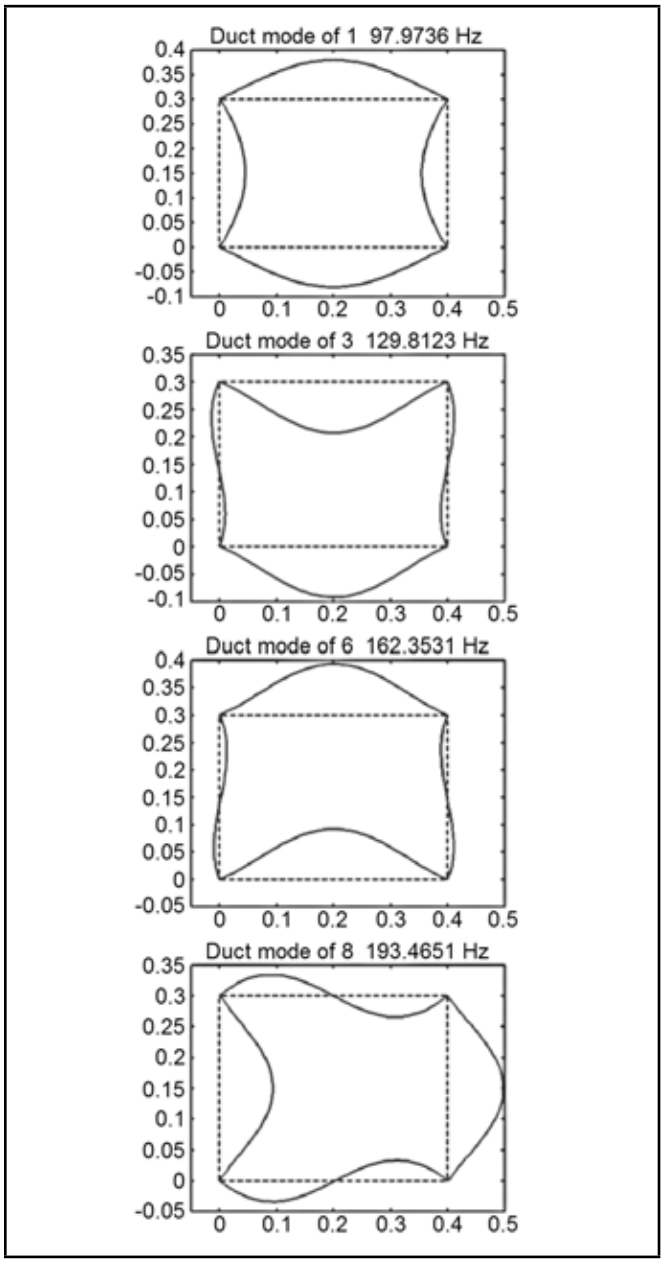

Figure 3. Mode shapes for the 1st, 3rd, 6th, and 8th natural frequencies of a rectangular duct with S-S boundary conditions.

actly with the values given by the present method (can be seen from first two columns of Table 1). The results are also compared with the transfer matrix method and the FEM results. The error observed is less than 5%. So a good amount of accuracy can be seen within these results. The same thing can be observed for the other axial boundary conditions. Results are shown in Tables 2, 3, and 4. The mode shapes are plotted and are shown in Fig. 3. Dominantly, the symmetric-symmetric (S-S) and symmetric-antisymmetric (S-AS) modes can be observed at the first few frequencies, and the antisymmetric-antisymmetric (AS-AS) modes can be observed at higher frequencies.

3.1. Engineering Data

Now this validated analytical model is used to generate values of a non-dimensional frequency parameter (λ) for different standard dimensions of the rectangular ducts. The dimensions of the ducts are divided into two ratios, one is a side ratio represented by 'S_1.' The other one is an aspect ratio represented by 'S.' The non-dimensional frequency (λ) values have been given for the different combinations of these ratios. The ratios used are 0.25, 0.5, 0.75, and 1. According to the dimension of the duct, one has to decide both of the ratios, then, from the table, select the appropriate λ value for the combination of these ratios. Eq. (13) can be used to calculate the natural frequencies in Hz from this non-dimensional value. This non-dimensional frequency parameter is independent of the material properties except for the Poisson's ratio, which is used as 0.29 to generate these values. Frequency (f) in Hz is given by

$$f = \frac{\lambda}{2\pi \times L_3^2}\sqrt{\frac{Eh^2}{12\rho\,(1-\nu^2)}}; \tag{13}$$

where L_3 and h are the length and thickness of the duct, respectively, and E, ρ, and ν are Young's modulus, density, and Poisson's ratio, respectively.

Tables 5 to 8 contain the values of λ for the first four natural frequencies of the rectangular duct. This data is generated for different combinations of aspect ratios and side ratios and also for different axial boundary conditions like S-S, C-C, C-S, and C-F, respectively.

Table 5. The non-dimensional frequency parameter (λ) for the S-S axial boundary condition.

Mode no.	$S_1\downarrow \ \backslash \ S\rightarrow$	0.25	0.5	0.75	1
1	0.25	1678.81	424.56	192.37	111.19
2		1698.35	444.75	213.57	130.32
3		1731.41	480.53	227.03	133.55
4		1779.04	503.55	245.79	150.33
1	0.5	2066.62	522.62	236.72	136.69
2		2090.51	546.78	261.36	161.90
3		2130.53	588.06	295.12	168.77
4		2187.11	647.61	304.25	189.31
1	0.75	2409.82	609.41	276.02	159.34
2		2437.71	637.34	304.05	187.50
3		2484.11	684.12	351.20	211.54
4		2549.40	750.01	370.74	233.18
1	1	2536.54	641.52	290.61	167.78
2		2566.14	671.13	320.21	197.39
3		2615.41	720.48	369.56	246.74
4		2684.52	789.57	438.65	254.14

Table 6. The non-dimensional frequency parameter (λ) for the C-C axial boundary condition.

Mode no.	$S_1\downarrow \ \backslash \ S\rightarrow$	0.25	0.5	0.75	1
1	0.25	1679.71	426.02	194.49	114.12
2		1701.64	450.18	221.69	132.86
3		1739.22	492.66	228.86	144.41
4		1790.91	504.81	252.95	160.12
1	0.5	2067.81	524.15	238.81	139.48
2		2094.34	552.26	269.08	171.01
3		2139.32	600.20	296.77	171.96
4		2200.11	657.45	320.45	197.92
1	0.75	2411.15	611.05	278.14	162.07
2		2441.91	643.01	311.65	197.15
3		2494.03	696.64	367.04	213.58
4		2563.62	769.22	372.31	240.96
1	1	2537.91	643.21	292.76	170.52
2		2570.52	676.93	327.85	206.98
3		2625.82	733.28	385.44	256.09
4		2699.31	808.97	447.52	261.29

3.2. Empirical Relation

In the above section, the non-dimensional frequency parameter (λ) has been given for different duct geometry dimensions,

Table 7. The non-dimensional frequency parameter (λ) for the C-S axial boundary condition.

Mode no.	$S_1 \downarrow \ \backslash \ S \rightarrow$	0.25	0.5	0.75	1
1	0.25	1679.23	425.22	193.32	112.46
2		1700.02	447.36	217.33	131.43
3		1735.07	486.24	227.84	138.50
4		1784.83	504.12	249.11	154.78
1	0.5	2067.24	523.31	237.67	137.93
2		2092.51	549.47	265.01	166.55
3		2134.62	593.78	295.86	169.76
4		2193.55	656.79	311.88	193.27
1	0.75	2410.47	610.15	276.98	160.56
2		2439.91	640.18	307.70	192.02
3		2488.83	690.04	358.68	212.45
4		2556.35	759.26	371.44	236.80
1	1	2537.11	642.28	291.58	169.01
2		2568.42	674.05	323.90	201.91
3		2620.36	726.50	377.07	255.02
4		2691.81	798.94	446.67	255.68

Table 8. The non-dimensional frequency parameter (λ) for the C-F axial boundary condition.

Mode no.	$S_1 \downarrow \ \backslash \ S \rightarrow$	0.25	0.5	0.75	1
1	0.25	1673.84	419.56	187.35	106.12
2		1687.01	433.38	201.87	121.26
3		1714.45	462.46	222.62	125.87
4		1777.71	499.18	232.96	139.24
1	0.5	2060.52	516.49	230.60	130.58
2		2076.94	533.24	247.76	148.15
3		2109.71	567.12	282.94	164.01
4		2152.16	616.66	290.38	177.96
1	0.75	2402.53	602.24	268.88	152.23
2		2419.63	621.66	288.55	172.15
3		2450.82	660.51	327.82	206.34
4		2506.91	719.04	365.55	211.42
1	1	2528.80	633.90	283.02	160.24
2		2549.34	654.50	303.83	181.26
3		2590.37	695.72	345.11	222.43
4		2651.32	756.99	407.09	248.42

Table 9. Values of constant 'λ_0' in an empirical Equation (14).

Axial boundary condition	Value of constant
S-S	169
C-C	171.5
C-S	170
C-F	165

from which one can calculate the first four natural frequencies directly for standard-dimension ducts. In this section, the empirical relation has been presented, which will be useful to get the non-dimensional frequency parameter (λ) for any combination of aspect ratios between 0.25 to 1 and side ratios between 0.25 to 1. This empirical relation has been formed by performing curve fitting for the above generated data. The empirical relation is of the form

$$\lambda = \lambda_0 \times S^{-1.96} \times S_1^{0.31}; \tag{14}$$

where λ_0 is constant, which depends on the axial boundary condition. Table 9 represents the values of constant 'λ_0' for different cases.

This empirical relation is useful for calculating the first fundamental frequency of a rectangular duct with different axial boundary conditions.

4. CONCLUSIONS

Free vibration analysis of rectangular ducts with different axial boundary conditions is important for understanding the vibration behaviour of these ducts in HVAC systems. A procedure is developed to calculate natural frequencies and mode shapes of a rectangular duct with different axial boundary conditions based on the Rayleigh-Ritz method. The Rayleigh-Ritz method, with a set of static beam admissible functions, has been used to consider different axial boundary conditions. This is one of the distinct advantages of using the proposed method. The results have been presented for the typical rectangular-duct dimensions. Proposed model results are validated through comparison of the known values in the literature and the results from the FEM method. Results are in agreement with accuracy more than 95%. This validated analytical model has been used to generate the engineering data, which will help engineers calculate the first four natural frequencies for different rectangular-duct dimensions. The empirical relation has been proposed based on engineering data. It will be helpful to calculate the first fundamental frequency of a rectangular duct for any combination of aspect ratios and side ratios in the range of 0.25 to 1 and also for different axial boundary conditions.

ACKNOWLEDGEMENT

The authors would like to thank the Indian Institute of Technology Hyderabad, for providing the required resources to conduct the current research work.

REFERENCES

[1] Azimi S, Soedel W., and Hamilton J.F. Natural frequencies and modes of cylindrical polynomial ducts using receptance method, *Journal of Sound and Vibration*, **109** (1), 79–88, (1986).

[2] Yamad G. and Kobayashi K. Comments on natural frequencies and modes of cylindrical polygonal ducts using receptance methods, *Journal of Sound and Vibration*, **115**, 363–364, (1987).

[3] Lee H. P., Natural frequencies and modes of cylindrical polygonal ducts, *Journal of Sound and Vibration*, **164**, 182–187, (1993).

[4] Irea T., Yamada G., and Ida H. Free vibration of longitudinally stiffened prismatic shells with and without partitions, *Journal of Sound and Vibration*, **102** (2), 229–241, (1985).

[5] Mohan S. J. and Pratap R. A natural classification of vibration modes of polygonal ducts based on group theoretical analysis, *Journal of Sound and Vibration*, **269**, 745–764, (2004).

[6] Zhou, D. Natural frequencies of rectangular plates using a set of static beam functions in Rayleigh-Ritz method, *Journal of Sound and Vibration*, **189** (1), 81–87, (1996).

[7] Zhou, D. and Cheung, Y. K. Free vibration of line supported rectangular plates using a set of static beam functions, *Journal of Sound and Vibration*, **223** (2), 231–245, (1996).

[8] Venkatesham B., Tiwari, M., and Munjal M. L., Prediction of breakout noise from a rectangular duct with compliant walls, *International Journal of Acoustics and Vibration*, **16** (4), 180–190, (2011).

[9] ANSYS 13, User Manual, ANSYS Inc.

Application of Linear Prediction, Self-Adaptive Noise Cancellation and Spectral Kurtosis in Identifying Natural Damage of a Rolling Element Bearing in a Gearbox

Cristóbal Ruiz-Cárcel, Enrique Hernani-Ros, Yi Cao, Michael Corsar and David Mba

School of Engineering, Cranfield University (UK); Building 52, Cranfield University, Bedfordshire, MK43 0AL, UK

Pramesh Chandra

Moog Aircraft Group, Wolverhampton (UK), Wobaston Road, Wolverhampton, WV9 5EW, UK

(Received 20 September 2012; revised 17 December 2013; accepted 26 February 2014)

The ability to detect and diagnose faults in rolling element bearings is crucial for modern maintenance schemes. Several techniques have been developed to improve the ability of fault detection in bearings using vibration monitoring, especially in those cases where the vibration signal is contaminated by background noise. Linear Prediction and Self-Adaptive Noise Cancellation are techniques which can substantially improve the signal to noise ratio of the signal, improving the visibility of the important signal components in the frequency spectrum. Spectral Kurtosis has been shown to improve bearing defect identification by focusing on the frequency band with a high level of impulsiveness. In this paper the ability of these three methods to detect a bearing fault is compared using vibrational data from a specially designed test rig that allowed fast natural degradation of the bearing. The results obtained show that the Spectral Kurtosis was able to detect an incipient fault in the outer race of the bearing much earlier than any other technique.

NOMENCLATURE

$a(k)$	Weight attached to each observation in LP
ANC	Adaptive Noise Cancelling
e	Output in ANC and SANC
f	Frequency
GM	Gear mesh frequency
H	Filter length
IRD	Inner race defect frequency
K	Kurtosis
LF	Line Frequency
LP	Linear prediction
n	Time point
N	Number of past samples considered in the calculation of R_τ
n_0	Reference noise
n_1	Uncorrelated eference noise
ORD	Outer race defect frequency
p	Number of past samples considered in LP
R_τ	Autocorrelation function
S	Signal of interest in ANC/SANC
SAN	Self-Adaptive Noise Cancellation
SK	Spectral Kurtosis
SNR	Signal to Noise Ratio
SS	Shaft speed frequency
W	Vector of filter coefficients
w	Filter weights in ANC and SANC
x	Random signal
$\hat{x}(n)$	Predictable part of signal x at
$y(n)$	Filter output
Δ	Time delay
Δf	Frequency band width
μ	Forgerring factor
μ	Average value
σ	Standard deviation

1. INTRODUCTION

Rolling element bearings are important components in rotating machinery. By monitoring the vibration signature of bearings, it is possible to obtain important information about their condition and use this information to improve the maintenance strategy. Diagnostic techniques based on vibration are mainly concerned with the extraction of defect features in the acquired signal, which can be related to the healthy or defective state of vital parts in a machine. Many different diagnostic methods have been successfully used to identify machine faults, processing the vibration signal in the time or frequency domain, in order to locate and quantify any existing damage. In complex machines the signal acquired is normally inclusive of additive background noise from other machine components or subsystems, which can make it difficult or sometimes impossible to identify the fault patterns in the signal.

In the case of bearings, the fault is produced typically by the damage of the surface of the inner or outer race or the rolling elements. When a damaged surface contacts another rolling surface, a force impulse is generated, which excites resonances in the bearing and the machine.[1] The successive impacts generate a vibration signal, which often has an impulsive repeti-

tive nature that is easy to identify in the presence of low background noise. In a real machine, the background noise can mask the bearing fault components of the signal, especially in gearboxes because the gear meshing can generate a strong level of vibration.[2] For this reason, many different methodologies of signal processing have been developed in order to facilitate the detection of defects, particularly in bearings.

Some examples of classic techniques used to enhance bearing fault features in vibration signals are linear prediction (LP), self-adaptive noise cancellation (SANC), cyclostationarity, Hilbert-Huang transform (HHT), and wavelet transform (WT). LP is based on the estimation of the deterministic part of a signal as a linear combination of the past inputs and outputs of the system, while SANC aims to minimize the noise in the manipulated signal by recursively adapting the filtration parameters.[3] Cyclostationarity studies the periodicities of the different features of machine vibration signals using the cyclic autocorrelation function and spectral correlation density.[4] HHT can be used to decompose a non-stationary and nonlinear signal into intrinsic mode functions and obtain instantaneous frequency data,[5] and WT can be applied on non-stationary signals to increase the frequency resolution at low frequencies and reduce noise in raw signals.[6] All of these techniques have been already applied by various researchers for the detection and diagnosis of bearing and gearbox faults.

In this investigation, three diagnostic techniques, LP, SANC and SK were applied in identifying a bearing defect in a gearbox where the bearing degradation happened naturally in a specially designed test rig. LP and SANC have been successfully used as de-noising tools in different applications for many years.[7,8] Nevertheless, even nowadays many researchers are exploring their capabilities to reduce background noise and enhance the fault features in a signal to improve the fault detection and diagnosis in bearings.[9–15] On the other hand, SK is a relatively new methodology that is able to enhance the fault signature in a signal by focusing in the frequency band with a higher level of impulsiveness.[16–18] This technique has been demonstrated to be very effective, especially for bearing fault detection, and many researchers have reported its benefits.[19–24]

The aim of this paper is to compare the performance of these methodologies in detecting a bearing fault during the early stages of natural degradation and show the benefits of SK over more stablished denoising techniques. For this purpose, these three methodologies have been applied on a vibrational signal acquired from a particular gearbox where the bearings failed much earlier than the theoretical life calculated for the loading conditions. Analysis of acquired vibration signals associated with different stages of bearing degradation proved to be ideal for this comparative study. This was principally because the bearing defect frequency was only evident at the final stage of degradation. Thus, the study presented will explore whether or not these techniques can offer the ability to identify the presence of the defect earlier.

2. THEORETICAL BACKGROUND

2.1. Linear Prediction

The estimation of a dynamic system output and its later analysis is one of the most important problems in signal processing. Different techniques have been employed by several researchers in a wide range of applications such as neurophysics, electrocardiography, geophysics, and speech communication.[7] One of the most powerful estimation models is based on the assumption that the value of a signal x at the time n can be obtained as a linear combination of past inputs and outputs of the system. Those models which use the information from only the past system outputs are called all-pole or autoregressive models, and were first used by Yule in an investigation of sunspot numbers.[25] LP is one of those methods where the objective is to predict or estimate the future output of a system based on the past output observations. The complete mathematical development and a compilation of the different LP approaches have been presented by Makhoul.[7]

In vibration-based diagnostics, LP is a method that allows the separation of the deterministic or predictable part of a signal from the random background noise using the information provided by past observations.[14,26] If it is assumed that the background noise is totally random, by applying this method, it is possible to eliminate the background noise and thus improve the signal-to-noise ratio. This technique is based on the principle that the value of the deterministic part of a signal can be predicted as a weighted sum of a series of previous values:

$$\hat{x}(n) = -\sum_{k=1}^{p} a(k) \cdot x(n-k); \tag{1}$$

where $\hat{x}(n)$ is the predictable part of the n$^{\text{th}}$ sample of the signal x, p is the number of past samples considered, and $a(k)$ are the weights attached to each past observation. The weighting coefficients can be obtained at each step, n, by a linear operation from the autocorrelation function R_τ of the time series $x(n)$, which can be efficiently solved using the Yule-Walker equation:[27]

$$\begin{bmatrix} R_0 & R_1 & \cdots & R_{p-1} \\ R_1 & R_0 & \cdots & R_{p-2} \\ \vdots & \vdots & \ddots & \vdots \\ R_{p-1} & R_{p-2} & \cdots & R_0 \end{bmatrix} \cdot \begin{bmatrix} a_1 \\ a_2 \\ \vdots \\ a_p \end{bmatrix} = \begin{bmatrix} -R_1 \\ -R_2 \\ \vdots \\ -R_p \end{bmatrix}; \tag{2}$$

where,

$$R_\tau = \frac{1}{N} \sum_{t=\tau}^{N} x(t-\tau) \cdot x(t). \tag{3}$$

N is the number of past samples considered at each step, in this case only p past samples were considered for each $\hat{x}(n)$ prediction for computational reasons, but all the available past samples at each time point were used in the calculation of the values R_τ.

The results of the algorithm depend on the number of past observations p considered. Small values of p produce a poor prediction, giving a result of negligible improvement in the signal-to-noise ratio, while very high values of p affect the computational cost negatively, over restrain the prediction, and tend to reduce even the main components of the signal. For this particular investigation, several analyses were carried out using different numbers of past samples in order to establish the value p for each test case, which optimizes the signal-to-noise ratio of the output signal.

2.2. Self-Adaptive Noise Cancellation

Adaptive noise cancelling (ANC) is another technique used to reduce the background noise in a signal and increase the

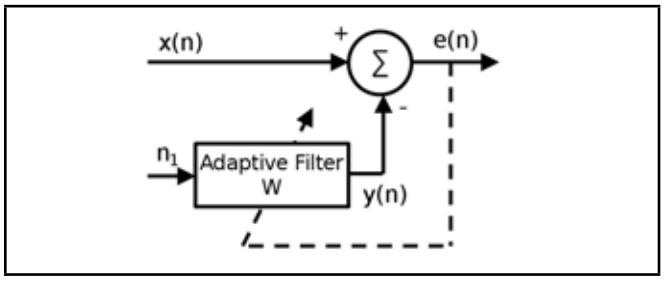

Figure 1. ANC algorithm.

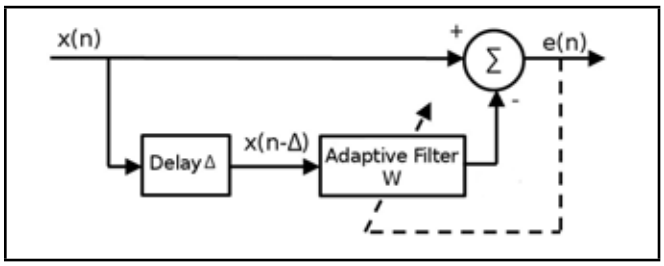

Figure 2. SANC algorithm.

signal-to-noise ratio, improving the visibility of the different signal components in the frequency spectrum. The first work in ANC was performed by Howells and Applebaum at the General Electric Company between 1957 and 1960. The first ANC system was designed and built at Stanford University in 1965.[8] Since then, this method has been successfully applied to a number of additional problems including electrocardiography, cancelling noise in speech signals, cancelling antenna sidelobe interferences, etc.[8]

The general ANC concept is shown in Fig. 1, and a basic explanation of the method was given by Chaturvedi et al.:[28] the input $x(n)$ composed by the signal of interest S and additive noise n_0 is received at the primary sensor. A reference noise n_1 (which must be related to the noise n_0 in some unknown way but is not coherent with the signal S) is received at the reference sensor. The reference input is then adaptively filtered to match n_0 as closely as possible, which is then subtracted from the primary input $x(n) = S + n_0$ to produce the system output $e = S + n_0 - y$. This output contains the signal plus residual undesirable noise. The adaptive filter acts to minimize, indirectly, the average power of this residual noise at the system output e. The output is fed back to the adaptive filter, and the filter weights are adjusted at each calculation step to minimize the total output power of the system. It can be demonstrated that minimizing the total output power minimizes the output noise power or, in other words, maximizes the output signal-to-noise ratio.[8]

The problem of this method applied to bearing fault detection in real applications is that it is not always easy to identify the source of noise n_1, which is correlated with the noise n_0 (common source) but not with the fault signal. Chaturvedi et al.[28] presented an example where the method was applied to detect an induced bearing fault in a gearbox using two sensors; one was placed in the surroundings of the bearing housing to obtain the main signal, and another sensor was placed at a remote location in the casing of the gearbox to obtain the reference signal. To solve this issue, a further development of ANC was formulated using a delayed version of the primary signal.[8] This latter version was named the self-adaptive noise cancellation (SANC), and the schematic concept is represented in Fig. 2. The time delay Δ, which is fixed, forces the delayed version of the input signal to become uncorrelated with the primary signal, introducing a phase difference. The adaptive filter responds firstly by compensating for the phase shift so that the sinusoidal components cancel each other at the output, and secondly by removing as much noise as possible to minimise the output error.[29] As it happens in the original ANC, the output error is then fed back to the adaptive filter to adjust recursively the filter weights w in order to minimize the total output power and thus, the output noise power. There are many adaptation rules to do this, the most well-known is the least mean square:[8]

$$w_i^{n+1} = w_i^n + \mu \cdot e(n) \cdot x(n - \Delta - i); \tag{4}$$

where the parameter μ (forgetting factor, strictly positive) controls the stability and rate of convergence of the process, and the subscript i differentiates each of the H weighting coefficients of the filter. The recursive weight calculation starts with a random value for each weight w_i. The output of the filter $y(n)$ can be calculated as:

$$y(n) = W^T(n) \cdot X(n - \Delta); \tag{5}$$

where W is a vector containing the H weighting coefficients w_i, and $X(n - \Delta)$ is another vector containing the H components of the delayed signal immediately preceding the sample n. The output $e(n)$ is easily obtained from:

$$e(n) = x(n) - y(n). \tag{6}$$

As shown by Eq. (4), the performance of the SANC algorithm clearly depends on the choice of three parameters: the time delay Δ, the filter length H, and the forgetting factor μ. The influence of these parameters was investigated by Ho et al.[30] who suggested some parameter selection guides. Δ should be large enough to ensure that the delayed signal becomes uncorrelated with the original, and H should be chosen to cancel all the broadband components of the delayed signal. In both cases, if the selected value for the parameter is too large, it will lead to computation problems. Ho[30] stated that the forgetting factor depends mainly on the filter order H. In this particular investigation, the parameters Δ, H, and μ were selected after several tests with the aim of optimizing the signal-to-noise ratio of the output signal. From these tests it was concluded that the selection of μ is crucial for the process performance: very small variations on this parameter can change the output signal, from no noise reduction effect if the selected value is too high, to distortion of the main signal components when it is too low. This influence can be seen in Fig. 3 where the SANC was applied to a representative signal acquired during the tests using different values for the forgetting factor μ. It is always important to check the convergence of the filter weights to ensure optimal performance.

2.3. Spectral Kurtosis and Envelope Analysis

Kurtosis is defined as the degree of peakness of a probability density function $p(x)$, and mathematically it is defined as the normalized fourth moment of a probability density function:[31]

$$K = \frac{\int_{-\infty}^{\infty} [x - \mu]^4 p(x) dx}{\sigma^4}; \tag{7}$$

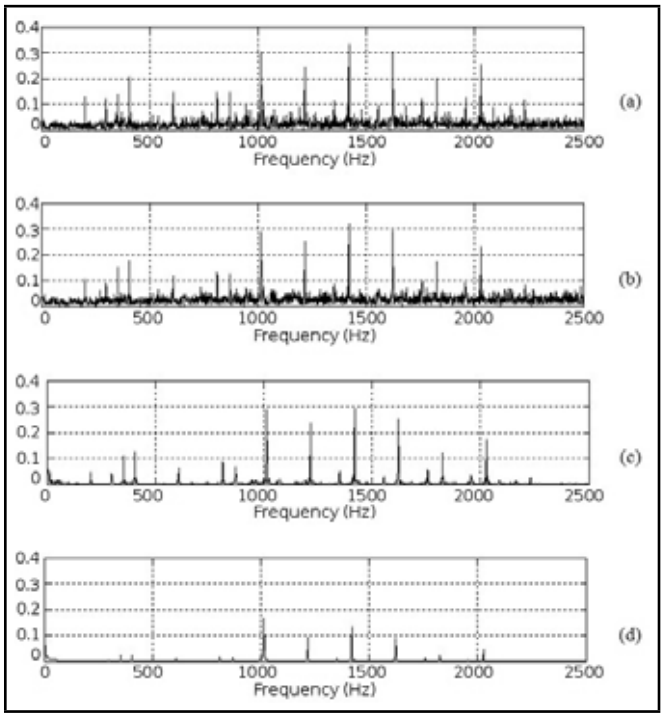

Figure 3. Effect of the forgetting factor μ on the SANC results. (a):original spectrum; (b) signal processed through SANC using $\mu = 0.0001$; (c) signal processed through SANC using $\mu = 0.00001$; (d) signal processed through SANC using $\mu = 0.000001$.

where x is the signal of interest with average μ and standard deviation σ.

As mentioned earlier, in real applications background noise often masks the signal of interest, and, as a result, the kurtosis is unable to capture the peakness of the fault signal, giving usually low kurtosis values. Therefore, in applications with strong background noise, the kurtosis as a global indicator is not useful, and it gives better results when it is applied locally in different frequency bands.[17] This technique is named spectral kurtosis (SK).

The SK was first introduced by Dwyer[32] as a statistical tool, which can locate non-Gaussian components in the frequency domain of a signal. This method is able to indicate the presence of transients in the signal and show their locations in the frequency domain. It has demonstrated to be effective even in the presence of strong additive noise.[17] The basic principle of this method is to calculate the kurtosis at different frequency bands in order to identify non stationarities in the signal and determine where they are located in the frequency domain. Obviously the results obtained strongly depend on the width of the frequency bands Δf in which the analysis is performed and its influence was analysed by Antoni.[18]

The kurtogram is basically a representation of the calculated values of the SK as a function of f and Δf.[33] However, the exploration of the whole plane (f, Δf) is a complicated computation task difficult to deal with, though Antoni[18] suggested a methodology for the fast computation of the SK. In this approach, at each bandwidth level, the number of filtered sequences is increased by a factor 2, and the kurtogram is finally estimated by computing the kurtosis of all sequences.

The importance of the kurtogram relies on the fact that it allows the identification of the frequency band where the SK is maximum, and this information can be used to design a filter that extracts the part of the signal with the highest level of impulsiveness. Antoni et al.[17] demonstrated how the optimum filter which maximizes the signal-to-noise ratio is a narrowband filter at the maximum value of SK. Therefore the optimal central frequency and bandwidth of the band-pass filter are found as the values of f and Δf which maximise the kurtogram. The filtrated signal can be finally used to perform an envelope analysis, which is a widely used technique for identification of modulating frequencies related with bearing faults. In this investigation the SK computation and the subsequent signal filtration and envelope analysis was performed using original Matlab code programmed by Jérôme Antoni.

This investigation assesses the merits of these three techniques in identifying a natural degraded bearing under conditions of relatively large background noise.

3. EXPERIMENTAL SET UP

The vibrational data used in this investigation was obtained from a specially designed gearbox test rig. The gearbox type employed is a part of the transmission driveline on the actuation mechanism of secondary control surfaces in civil aircrafts. The bearing of this gearbox failed in an endurance test at around 30% of its total expected life (around 3000 hours), making it an ideal candidate for this investigation where fast natural degradation of the bearing was needed. The rig was built originally to identify the origin of premature failure in order to modify the gearbox design. The acquired vibrational signal was used in this investigation to find traces of the fault during the early stages of degradation, which is an obvious advantage from a maintenance point of view.

This gearbox, whose basic cross section is shown in Fig. 4, has two bevel gears with 17 teeth on each gear, generating a transmission ratio of 1:1. Each gear is supported by two angular contact bearings with 12 balls each and a contact angle of 40°, mounted in a back-to-back configuration. The main dimensions of the bearing and the attached bearing defect frequencies can be seen in Table 1 and Table 2 respectively. The test rig was built trying to emulate the actual transmission system used in the aircraft, and it is schematically represented in Fig. 5. The transmission is driven by an electric motor with a nominal speed of 710 rpm. An electric load motor placed at the opposite side of the test rig was used to apply different loads used during the experiment. In order to simulate the actual loading conditions expected during the life of the gearboxes, the test rig was subjected to a mixture of seven different types of flight load cycles derived from the actual flight data and loads. These load cycles include the simulation of takeoff and landing with different flap positions, ground maintenance, etc. The expected bearing life for these loading conditions was around 3000 hours. Figure 6 shows a typical type 3 load profile, which was chosen as an illustrative example because it contains several speed changes and the highest torque is applied in this particular load cycle. The loading conditions of each cycle type applied are explained in Table 3, which specifies the number of times each cycle was applied during the experiment for the expected bearing life, the duration of each cycle, and the maximum torque applied in each case.

The experiment ran continuously for 24 hours a day over a duration of 36 days, but at certain points during the test run the rig was stopped for visual inspection for damage in the bearings. The gearbox was always then reassembled and the se-

Table 2. Main Defect Frequencies and Harmonics (Hz).

Harmonic	1X	2X	3X	4X	5X	6X
Shaft speed frequency (SS)	11.8	23.7	35.5	47.3	59.2	71
Gear mesh frequency (GM)	201.2	402	604	805	1006	1207
Inner race defect frequency(IRD)	83.2	166	250	333	416	499
Outer race defect frequency (ORD)	58.8	118	176	235	294	353
Cage defect frequency	4.9	9.8	14.7	19.6	24.5	29.4
Ball spin frequency	25.6	51.2	76.8	102	128	154
Rolling element defect frequency	51.2	102	154	205	256	307

Table 3. Load cycles characteristics summary.

Cycle type	1	2	3	4	5	6	7	8	9
Number of repetitions during bearing life	18296	22869	4574	462	462	2200	6600	4620	41580
Duration (sec)	131	131	131	350	42	71	268	52	52
Torque max. (Nm)	126.1	126.1	158.6	126.1	126.1	42.8	42.8	12.4	97.7

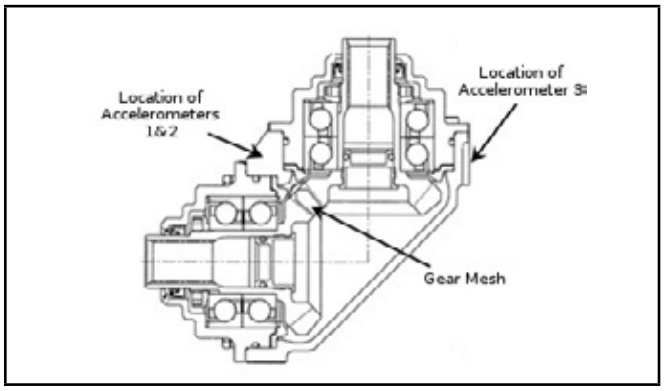

Figure 4. Gearbox Section.

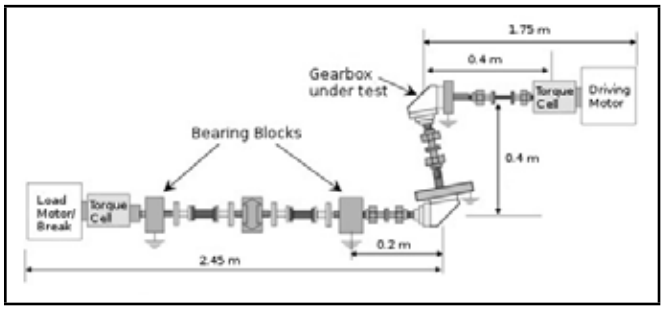

Figure 5. Layout of the test rig.

quence continued. Figure 7 shows a detail of the bearing outer race during a visual inspection undertaken one month after the experiment started, covering 24% of the estimated bearing life.

Three accelerometers were mounted in the gearbox at locations identified in Fig. 4, two of them placed on the top of the gearbox measuring acceleration in the vertical plane and a third one placed on the casing measuring the acceleration in the horizontal plane. The selected accelerometers (Omni Instruments model RYD81D) had an operating frequency range of 10 Hz to 10 kHz. These accelerometers were connected to signal conditioners (model Endevco 2775A) that were at-

Table 1. Bearing Main Dimensions.

No. of rolling elements	12
Ball Diameter (B_d)	0.4063"
Contact Angle (Φ)	40°
Pitch Diameter (P_d)	1.811"
Input Shaft Speed	710 rpm
Gear Teeth	17

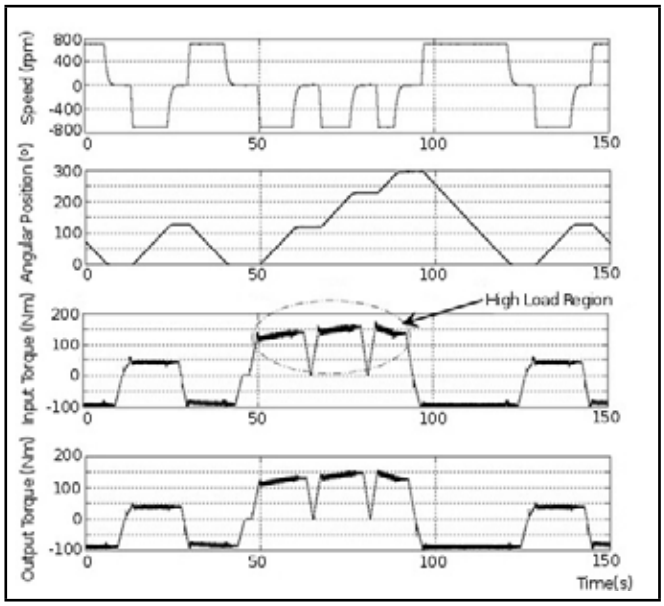

Figure 6. Type 3 load cycle profile.

tached to an NI USB 6009 data acquisition device. This digital data was filtered, windowed, and stored in the computer using Dasylab version 10.0, and finally it was exported for its final manipulation in Matlab R2010A. Other than the vibration data, various parameters were monitored and stored at the same time and with the same sampling frequency: angular position of the input shaft, input and output torque, and shaft speed.

The experiment started running on 19 July 2010 and the vibration measurements were taken on the 19 August 2010, 22 August 2010, and finally on 24 August 2010. For each measurement case, a total 1,048,569 points were acquired at a sampling rate of 5 kHz, which resulted in a measurement length of approximately 3.5 minutes; sufficiently long to cover a whole loading cycle. The stored data was then analysed, selecting groups of 8,192 data samples in the region of constant speed where maximum load was applied (Fig. 6). After a preliminary data analysis it was decided to always use the signal acquired by the third channel in the next steps of the analysis. This signal comes from the accelerometer which measures acceleration in the horizontal plane, and the characteristics found in the signal spectrum were representative of what was observed in the other channels.

The visibility of the main signal components is usually measured using the signal-to-noise ratio (SNR). This concept is widely used in electronics to evaluate the performance of dif-

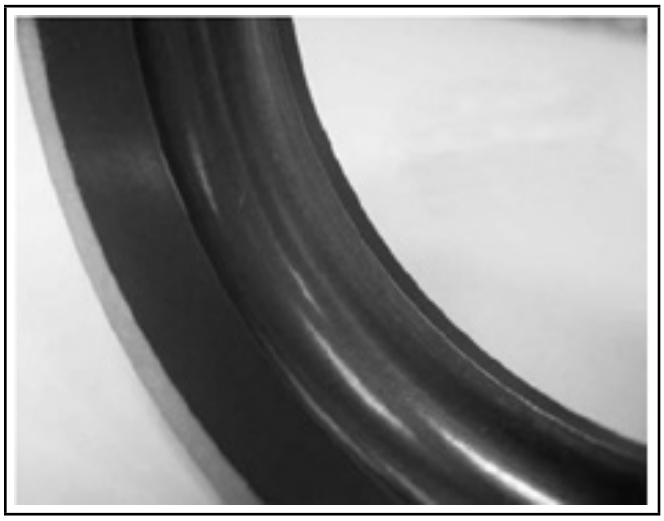

Figure 7. Detail of bearing outer race after one month.

ferent electronic devices such as amplifiers or radio receivers because it gives a measure of the signal quality. In those applications, the signal-to-noise ratio is calculated as the ratio between the power of the signal and the power of the background noise. Another definition of SNR is the ratio between the average amplitude of the main signal components μ, and the standard deviation of the background noise σ, which is equivalent to the reciprocal of the coefficient of variation.[34] This alternative definition is used in those applications where it is difficult to differentiate between the main signal and the background noise such as image processing, and this definition was employed in this investigation. The average amplitude of the main signal components was calculated in each case as the average amplitude of the visible peaks associated with the characteristic defect frequencies (Table 2), while the rest of the components with significant lower amplitude were considered as background noise. In order to estimate the average amplitude of the main signal components, the amplitude attached to each characteristic frequencies of the rig (Table 2) and its harmonics, was calculated for each spectrum. Obviously, because not all the possible defects were present at all times, it was necessary to determine whether there is a visible peak at each of those defect frequencies or not for each measurement. The assumption made was to consider main signal components only those peaks whose amplitude in the spectrum is at least 3 times the average amplitude across the whole frequency range. This average was calculated excluding the amplitudes related with the defect frequencies. Using this procedure, it was possible to separate the main peaks in the spectrum attached to the known defect frequencies and the rest of the components in the spectrum, considered as background noise. According to this definition, each case that studied the improvement in the signal-to-noise ratio was measured as a percentage comparing the SNR of the manipulated signal against the SNR of the raw signal.

4. RESULTS OBTAINED

Once the experiment was carried out, the data acquired was processed using the methodologies mentioned in Section 2. The results obtained for each measurement are plotted in this section with the following format:

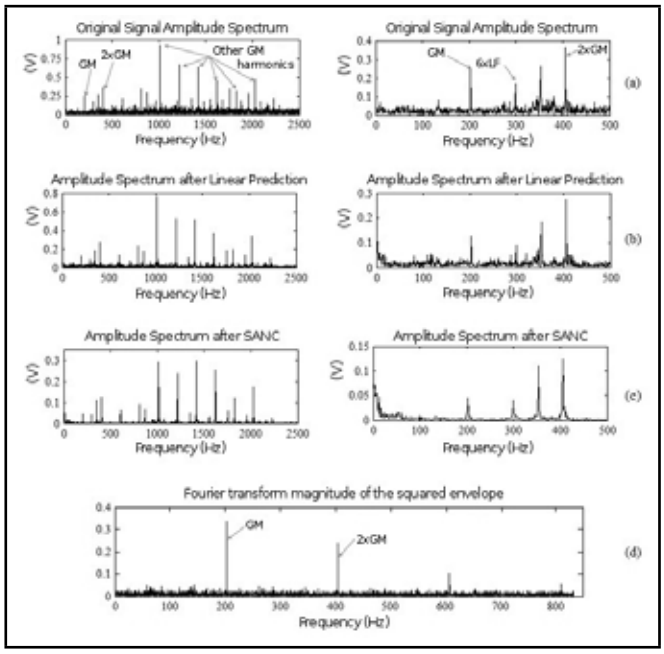

Figure 8. Results obtained from the first observation (19/08/10)

a) Amplitude spectrum of the original signal

b) Amplitude spectrum of the signal obtained by LP

c) Amplitude spectrum of the signal obtained by SANC

d) Magnitude of the squared envelope of the signal obtained by filtration in the frequency band of the maximum SK

The spectrums of the original signal and the signals obtained by LP and SANC are represented twice. The left plot corresponds to the spectrum covering a frequency range of 0–2500 Hz which contains the gear mesh components and its harmonics. The right plot covers the region of 0–500 Hz, where it is easier to identify the typical defect frequencies. The available frequency range of the squared envelope of the signal obtained by filtration after the kurtosis analysis depends on the filter parameters, different for each analysis. The kurtograms of the different observations and the main information extracted taken can be seen in Annex 1.

4.1. First Observation (19/08/2010)

For this observation, the LP analysis (Fig. 8(b)) was performed using 200 past samples for each prediction, and the parameters selected for the self-adaptive filter (Fig. 8(c)) were: delay $\Delta = 100$ samples, filter order $H = 1000$, and forgetting factor $\mu = 0.00001$. The maximum kurtosis found was 2.4, at a frequency band centred in 2083.33 Hz and a bandwidth of 833.3 Hz.

4.2. Second Observation (22/08/2010)

For the second observation, the LP analysis (Fig. 9(b)) was performed using 200 past samples for each prediction, and the parameters selected for the self-adaptive filter (Fig. 9(c)) were: delay $\Delta = 500$ samples, filter order $H = 1000$ and forgetting factor $\mu = 0.00005$. The maximum kurtosis found was 2.4 at a frequency band centred in 2083.33 Hz and a bandwidth of 833.3 Hz.

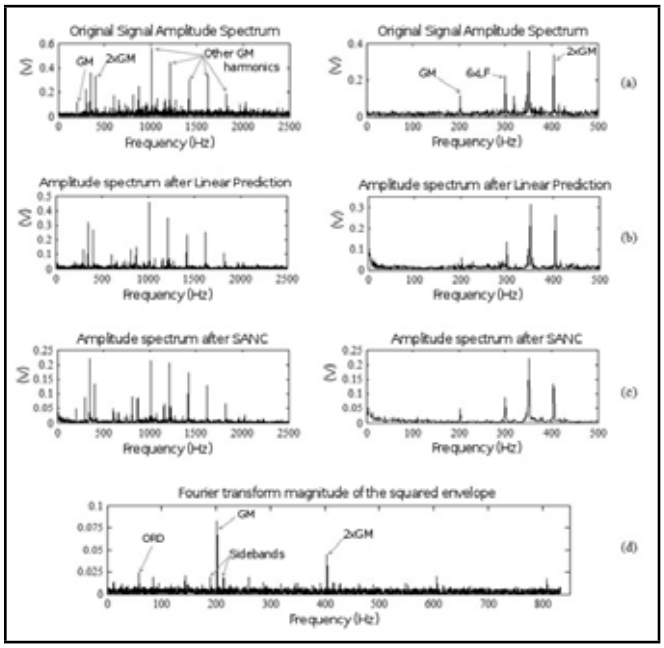

Figure 9. Results obtained from the second observation (22/08/10)

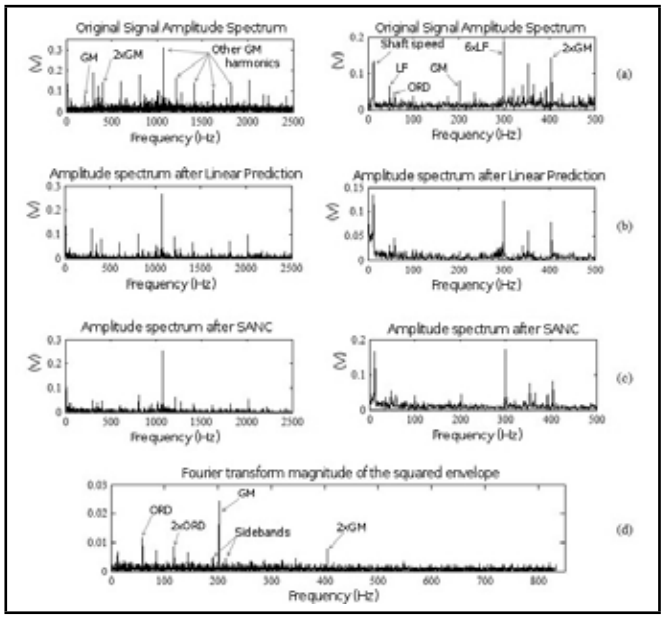

Figure 10. Results obtained from the third observation (24/08/10).

4.3. Third Observation (24/08/2010)

For the third observation, the LP analysis (Fig. 10(b)) was performed using 200 past samples for each prediction, and the parameters selected for the self-adaptive filter (Fig. 10(c)) were: delay $\Delta = 500$ samples, filter order $H = 1000$, and forgetting factor $\mu = 0.0001$. The maximum kurtosis found was 1.7, at a frequency band centred in 2083.33 Hz and a bandwidth of 833.3 Hz.

5. RESULTS AND DISCUSSION

The first measurement (19/08/10, Fig. 8) was acquired one month after the start of the experiment, which corresponds approximately to 24% of the expected bearing life. The spectrum of the original signal is clearly dominated by the gear mesh frequency ($\sim$202 Hz) and its harmonics. However, looking closely to the lower frequencies (the right column) it is possible to see a peak around 352 Hz, which is close to the 6^{th} harmonic of the outer race defect frequency (ORDF), but any defect in the outer race at this point was ruled out by visual inspection (see Fig. 7). The presence of this peak is attributed to a natural frequency of the structure or a consequence of deformation due to the three-point clamping during grinding the outer ring, and it will be present in all the stages of the experiment. There is also a component at 300 Hz, which corresponds to the 6^{th} harmonic of the 50 Hz line frequency (LF). This was corroborated by the fact that this peak appears even for those analyses carried out using data from the load cycle region where the motor speed was 0, indicating that this is a parasite component coming from the electrical grid.

From the analysis and observations of Fig. 8, background noise was reduced by LP and especially by SANC, increasing clearly the signal-to-noise ratio compared with the original signal, which are 2.6% and 42.9%, respectively (see Table 4), and facilitating the identification of the different signal components. The amplitude of the main peaks in the frequency spectrum were also reduced in magnitude, but this is not significant in terms of component identification because the signal contains the same main components at a better signal-to-noise ratio. No new peaks masked by the background noise were identified. The envelope obtained after the signal filtration at the maximum kurtosis frequency band shows clearly that the signal is dominated by the gear mesh frequency, but at this moment it does not provide any information of an incipient fault in the system.

The original spectrum of the second measurement taken three days after the first one (see Fig. 9) shows more or less the same components noted in the first observation, with the difference being that there is a reduction in the amplitude of the peaks, and the background noise is slightly lower. No new signal components are identified by LP or SANC, despite the fact that the background noise reduction is considerable, with an improvement of the 14.4% and 16.5%, respectively, in the signal-to-noise ratio in comparison with the original signal (see Table 4). The most interesting result of this analysis is the signal envelope obtained after the filtration at the maximum kurtosis band: apart from the typical gear mesh frequency and harmonics, it is possible to identify a new peak at the frequency of 58.4 Hz, indicating an incipient fault in the outer race of the bearing, in addition to sidebands around the gear mesh frequency at 190.2 Hz and 214 Hz. The distance between them and the gear mesh frequency is approximately 12 Hz, the shaft speed. It is important to emphasize the fact that (d) in Figs. 7, 8, and 9 represents the spectrum of the squared envelope of the filtered signal, not the spectrum of the filtered signal itself.

On 24 August 2010, the last data capture was performed (see Fig. 10). The first observation to note is that the amplitude of the different components is lower in this case. This is due to the fact that this measurement was done during a loading cycle type where the maximum transmitted torque was lower (40 Nm) than in the previous measurements (125 Nm). Even under these low torque conditions and despite the reduction in amplitude, all previously noted peaks were evident in the spectrum, in addition to a clear peak at 58.8 Hz, indicating the defect in the outer race of the bearing. Moreover, several sidebands around the harmonics of the gear mesh frequency,

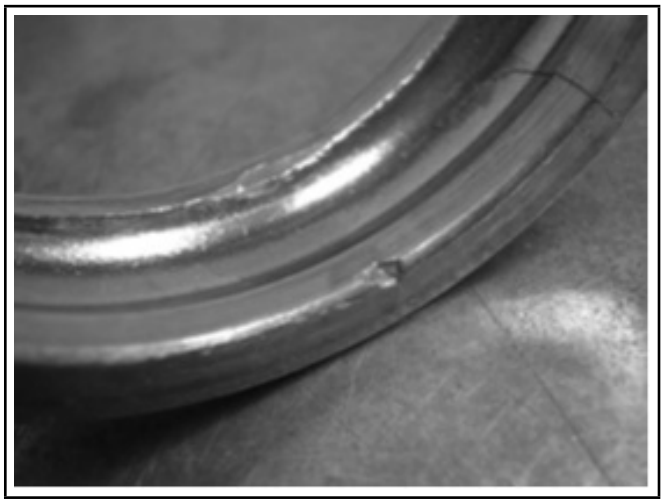

Figure 11. Bearing outer race degradation after 36 days.

Table 4. Maximum Kurtosis location.

Observation	Method	μ	σ	SNR
1	Original	0.2001	0.0190	10.5315
	LP	0.1004	0.0093	10.8054
	SANC	0.0612	0.0041	15.0496
	SK	0.0570	0.0054	10.6368
2	Original	0.1304	0.0120	10.8667
	LP	0.0701	0.0056	12.4314
	SANC	0.0548	0.0043	12.6596
	SK	0.0158	0.0014	11.1926
3	Original	0.0886	0.0087	10.18391
	LP	0.0487	0.0040	12.1750
	SANC	0.0353	0.0023	15.4082
	SK	0.0081	0.0008	9.6747

separated by the shaft frequency, were noted, showing that probably the bearing failure was causing a shaft misalignment, which affected the gear mesh. The spectrum of the squared envelope showed the peak at 58.8 Hz and a second harmonic of it at 117.9 Hz, indicating the fault in the outer race that was confirmed after by visual inspection of the component (Fig. 11).

6. CONCLUSION

This investigation shows the results of the application of three different vibration-based analysis methodologies for bearing diagnosis: LP, SANC, and SK together with envelope analysis. These techniques are typically used for applications where strong background noise masks the mechanical signature of a machine, making the identification of the fault source challenging. This is the case of the experiment presented in this investigation. LP, and particularly, the SANC showed its capability to reduce the background noise and facilitate the identification of the different components in the signal spectrum, but in this specific application they did not identify the defect on a bearing earlier than the SK.

The latter technique demonstrated the ability to identify the defect earlier than all other methods. This method is thus a very powerful tool for the early detection of faults in bearings, even for those applications where strong background noise from other sources in the machine masks the characteristic fault components in the frequency domain.

ACKNOWLEDGEMENTS

Financial support from the Marie Curie FP7-ITN project "Energy savings from smart operation of electrical, process and mechanical equipment– ENERGY-SMARTOPS," Contract No: PITN-GA-2010-264940 is gratefully acknowledged

REFERENCES

[1] Ho, D. and Randall, R. B. Optimization of bearing diagnostic techniques using simulated and actual bearing fault signals, *Mechanical Systems and Signal Processing*, **14** (5), 763–788, (2000).

[2] Tan, C. C. An Adaptive Noise Cancellation Approach for Condition Monitoring of Gear Box Bearings, *International Tribology Conference, no 87/18*, Melbourne, Victoria, 360–365, (1987).

[3] Randall, R. B. and Antoni, J. Rolling element bearing diagnostics – A tutorial, *Mechanical Systems and Signal Processing*, **25** (2), 485–520, (2011).

[4] Behzad, M., Bastami, A. R. and Mba, D. Rolling bearing fault detection by short-time statistical features, *Proceedings of the Institution of Mechanical Engineers, Part E: Journal of Process Mechanical Engineering*, **226** (3), 229–237, (2012).

[5] Li, H., Zhang, Y. and Zheng, H. Hilbert-Huang transform and marginal spectrum for detection and diagnosis of localized defects in roller bearings, *Journal of Mechanical Science and Technology*, **23** (2), 291–301, (2009).

[6] Li, F., Meng, G., Ye, L. and Chen, P. Wavelet transform-based higher-order statistics for fault diagnosis in rolling element bearings, *JVC/Journal of Vibration and Control*, **14** (11), 1691–1709, (2008).

[7] Makhoul, J. Linear Prediction: A Tutorial Review, *Proceedings of the IEEE*, **63** (4), 561–580, (1975).

[8] Widrow, B., Glover Jr., J. R. and McCool, J. M. Adaptive noise cancelling: principles and applications, *Proceedings of the IEEE*, **63** (12), 1692–1716, (1975).

[9] Da Silva, S. and Dias Junior, M. Statistical damage detection in a stationary rotor systems through time series analysis, *Latin American Applied Research*, **37** (4), 243–246, (2007).

[10] Dron, J. -., Rasolofondraibe, L., Chiementin, X. and Bolaers, F. A comparative experimental study on the use of three denoising methods for bearing defect detection, *Meccanica*, **45** (2), 265–277, (2010).

[11] Lu, B., Nowak, M., Grubic, S. and Habetler, T. G. An adaptive noise-cancellation method for detecting generalized roughness bearing faults under dynamic load conditions, *2009 IEEE Energy Conversion Congress and Exposition, ECCE 2009*, 1091, (2009).

[12] Sawalhi, N. and Randall, R. B. Helicopter gearbox bearing blind fault identification using a range of analysis techniques, *Australian Journal of Mechanical Engineering*, **5** (2), 157–168, (2008).

[13] Sui, W. and Zhang, D. *DWT-based adaptive filter and its application on canceling noise in mechanical signals*, (2010).

[14] Wang, W. Autoregressive model-based diagnostics for gears and bearings, *Insight: Non-Destructive Testing and Condition Monitoring*, **50** (8), 414–418, (2008).

[15] Patel, V. N., Tandon, N. and Pandey, R. K. Improving defect detection of rolling element bearings in the presence of external vibrations using adaptive noise cancellation and multiscale morphology, *Proceedings of the Institution of Mechanical Engineers, Part J: Journal of Engineering Tribology*, **226** (2), 150–162, (2012).

[16] Antoni, J. The spectral kurtosis: A useful tool for characterising non-stationary signals, *Mechanical Systems and Signal Processing*, **20** (2), 282–307, (2006).

[17] Antoni, J. and Randall, R. B. The spectral kurtosis: Application to the vibratory surveillance and diagnostics of rotating machines, *Mechanical Systems and Signal Processing*, **20** (2), 308–331, (2006).

[18] Antoni, J. Fast computation of the kurtogram for the detection of transient faults, *Mechanical Systems and Signal Processing*, **21** (1), 108–124, (2007).

[19] Chen, J., Zi, Y., He, Z. and Yuan, J. Improved spectral kurtosis with adaptive redundant multiwavelet packet and its applications for rotating machinery fault detection, *Measurement Science and Technology*, **23** (4), (2012).

[20] Li, H., Zheng, H. and Tang, L. Bearing fault diagnosis based on kurtogram of dual-tree complex wavelet packet transform, *Zhendong yu Chongji/Journal of Vibration and Shock*, **31** (10), 13–18, (2012).

[21] Bechhoefer, E., Kingsley, M. and Menon, P. Bearing envelope analysis window selection using spectral kurtosis techniques, *2011 IEEE International Conference on Prognostics and Health Management, PHM 2011 - Conference Proceedings*, (2011).

[22] Lei, Y., Lin, J., He, Z. and Zi, Y. Application of an improved kurtogram method for fault diagnosis of rolling element bearings, *Mechanical Systems and Signal Processing*, **25** (5), 1738–1749, (2011).

[23] Wang, Y. and Liang, M. An adaptive SK technique and its application for fault detection of rolling element bearings, *Mechanical Systems and Signal Processing*, **25** (5), 1750–1764, (2011).

[24] Su, W., Wang, F., Zhang, Z., Guo, Z. and Li, H. Application of EMD denoising and spectral kurtosis in early fault diagnosis of rolling element bearings, *Zhendong yu Chongji/Journal of Vibration and Shock*, **29** (3), 18–21, (2010).

[25] Yule, G. U. On a method of investigating periodicities in disturbed series, with special reference to Wolfer's sunspot numbers, *Philosophical Transactions of the Royal Society of london*, **226-A**, 267–298, (1927).

[26] Randall, R. B. 3.6.3 Linear Prediction, in John Wiley and Sons (ed.) *Vibration-based condition monitoring: Industrial, aerospace and automotive applications*, 2011th ed, Wiley, Singapore, 122–125, (2011).

[27] Ljung, L. 10.1 Linear Regressions and Least Squares, in Pentrice-Hall (ed.) *System identification: Theory for the user, 2nd ed, Pentrice-Hall, New Jersey*, 321–324, (1999).

[28] Chaturvedi, G. K. and Thomas, D. W. Bearing fault detection using adaptive noise cancelling, *Trans.ASME J.Mech.Des.*, **104** (2), Apr. 1982, 280–289, (1982).

[29] Antoni, J. and Randall, R. B. Unsupervised noise cancellation for vibration signals: Part I - Evaluation of adaptive algorithms, *Mechanical Systems and Signal Processing*, **18** (1), 89–101, (2004).

[30] Ho, D. and Randall, R.B. Effects of time delay, order of FIR filter and convergence factor on self adaptive noise cancellation, *Fifth International Congress on Sound and Vibration*, Adelaide, 945–952, (1997).

[31] Randall, R. B. 3.1. Probability Distribution and Density, in John Wiley and Sons (ed.) *Vibration-based condition monitoring: Industrial, aerospace and automotive applications*, Wiley, Singapore, (2011), 63–66.

[32] Dwyer, R. F. Detection of Non-Gaussian Signals by Frequency Domain Kurtosis Estimation, *ICASSP, IEEE International Conference on Acoustics, Speech and Signal Processing - Proceedings*, **2**, 607, (1983).

[33] Randall, R. B. 5.3 Spectral Kurtosis and the Kurtogram, in John Wiley and Sons (ed.) *Vibration-based condition monitoring: Industrial, aerospace and automotive applications*, Wiley, Singapore, (2011), 122–125.

[34] Smith, S. W. *The scientist and engineer's guide to digital signal processing*, 1st ed, California Technical Publishing, California, (1997).

ANNEX 1: INFORMATION PROVIDED BY THE KURTOGRAM

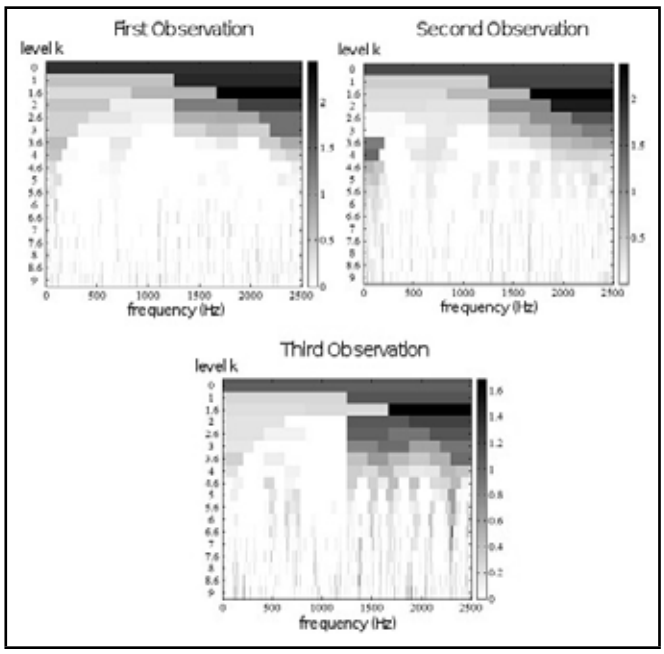

Figure 12. Kurtograms of the different observations.

Table 5. Maximum Kurtosis location.

Observation	Fc(Hz)	Δf(Hz)	K max	Frequency Band(Hz)
1	2083.33	833.3	2.4	1666.7-2500
2	2083.33	833.3	2.4	1666.7-2500
3	2083.33	833.3	1.7	1666.7-2500

Seismic Control of Continuous Bridges Using Variable Radius Friction Pendulum Systems and Viscous Fluid Dampers

A. Krishnamoorthy

Department of Civil Engineering, Manipal Institute of Technology, Manipal, 576 104, Karnataka, India

(Received 28 December 2012; revised 19 September 2013; accepted 5 March 2014)

This paper investigates the performance of a variable radius friction pendulum system (VRFPS) with supplementary damping using viscous fluid dampers (VFD) to control the seismic response of bridges. A VRFPS is similar to a frictional pendulum system (FPS), but the curvature of the sliding surface is varied, and it becomes the function of the sliding displacement. The bridge is seismically isolated with a VRFPS between the superstructure and the pier, and a VFD is added between the abutment and superstructure. Effectiveness of the proposed system is studied for a three-span continuous bridge isolated with a VRFPS and VFD hybrid system. The performance of a proposed system is compared to a corresponding performance of a hybrid system consisting of a conventional FPS with a VFD. The results of the numerical simulation showed that supplementary damping reduces the seismic response of the isolated bridge. Further, a hybrid system consisting of a VRFPS and a VFD is found to be more effective than a FPS and a VFD hybrid system for seismic control of bridges.

1. INTRODUCTION

Bridges are susceptible to damage when subjected to major earthquakes. The damage to the bridge structure occurs primarily in the piers, which results in the collapse of the bridge super structure. In recent years, seismic isolation devices such as rubber bearings or sliding bearings have been used to improve the seismic response and to reduce the damage of bridges for both new and retrofitting applications. These devices are placed between the superstructure and pier. The friction pendulum system (FPS) proposed by Zayas et al.[1] is recognized as an effective isolation device to reduce the seismic effects of buildings and bridges. In this system the sliding and restoring mechanisms are integrated in one unit in which the sliding surface takes a spherical shape.[2] However, the restoring stiffness, which is proportional to the curvature of the sliding surface will inevitably introduce a constant isolation frequency to the isolated structure.[3] This frequency remains constant during the earthquake ground motion due to the spherical sliding surface. A resonant problem may occur when the structure resting on the FPS is subjected to near-fault earthquake ground motions characterized by low frequency and high intensity. In one of the approaches, to overcome this problem, a sliding surface with variable frequency has been suggested.[2–4] In this system, the shape of the sliding surface of the FPS is made non-spherical by varying the curvature of the sliding surface with isolator displacement. These isolators are found to be effective in reducing the forces transferred to the structure at all intensities of excitations without showing any resonance problems. However, the sliding surface of these isolators is flatter than the FPS system. This induces large sliding displacement for low frequency and high intensity earthquakes, resulting in expensive loss of space for a seismic gap. In another approach, to overcome the resonance problem, various additional seismic control devices such as passive viscous fluid dampers[5,6] and active or semi-active variable stiffness or variable damping devices have been augmented[7–11] to the FPS or rubber bearings. Although, the active or semi-active devices by varying the properties like stiffness or viscosity are found to be more effective compared to passive devices, such systems are relatively complex since they require special hardware, sensors, and constant maintenance. On the other hand, passive devices are easy to maintain since they do not require any additional power and sophisticated equipment. Several analytical and experimental studies carried out on isolated buildings and bridges demonstrated a reduction in bearing displacement when additional passive damping devices are added to the FPS or rubber bearings. However, the major drawback of passive dampers with the FPS is their inability to adjust the parameters during the earthquake in response to seismic excitations. To overcome this problem, a FPS with a variable frequency is proposed in the present study instead of a FPS with a constant frequency. In the case of a variable frequency FPS, the frequency varies in response to seismic excitation due to the geometry of the isolator without the need of any external power. A new isolator known as a variable radius friction pendulum system (VRFPS) is proposed, and its effectiveness is investigated when additional passive damping using a viscous fluid damper (VFD) is added. A VRFPS isolator is used to overcome the resonance problem of the FPS associated with near-fault characteristics, and an additional passive damping device is used to reduce the sliding displacement of the isolator. Krishnamoorthy[12] studied the effectiveness of the VRFPS with a VFD for seismic isolation of space-frame structures. In this study, the effectiveness of the proposed isolator with a VFD is investigated to control the seismic response of a continuous bridge. The mechanical behaviour of a VRFPS is similar to that of a FPS. The difference between the VRFPS and a FPS is that the radius of the curvature is constant in the case of a FPS whereas it varies with the sliding displacement in the case of the VRFPS. For the pro-

posed isolator, the radius of the curvature along the sliding surface is varied using an exponential function. A VFD is placed between the abutments and superstructure, and a VRFPS is placed between the pier and superstructure. To study the effectiveness of the proposed system, the response of the bridge isolated with a VRFPS and a VFD system is compared with the response of a bridge isolated with a FPS and a VFD system under similar conditions.

2. GEOMETRY OF THE PROPOSED SLIDING SURFACE

In the case of a conventional FPS, the radius of the curvature, R, of the isolator is constant. Due to this, it may encounter a resonance problem at a low frequency. In order to overcome this limitation, an isolator with a varying radius of curvature along the sliding surface is proposed. Two similar devices, a variable frequency pendulum isolator (VFPI) and a variable curvature friction pendulum system (VCFPS) have been proposed respectively by Pranesh and Sinha[2] and Tsai et al.[4] The sliding surface of the VFPI is based on the expression of an ellipse, and the concave sliding surface of the VCFPS is based on subtracting a specific function from the expression of the FPS sliding surface. However, varying the radius exponentially with the sliding displacement proposed in this study can get the equation to describe the concave sliding surface of the VRFPS. The geometry of the isolator proposed in this study is similar to the geometry proposed by Krishnamoorthy[12] to isolate the space frame structure. The geometry of the VRFPS is chosen in such a way that its radius is similar to the radius of the FPS system at the centre of the sliding surface, and it increases with the sliding displacement and becomes infinity at a large sliding displacement. An expression to vary the radius exponentially with sliding displacement is found to be satisfactory in meeting the above requirement. For the proposed sliding surface, the radius of the curvature is a function of the sliding displacement x, and is given by the expression

$$R(x) = C\left(\exp\left(x\right) - 1\right) + R. \tag{1}$$

In the above equation, the sliding displacement x is expressed in meters, and C is the parameter to describe the variation of curvature of the concave surface. R is the radius of curvature, in meters, at the centre of VRFPS (at $x = 0$).

For a mass, m, sliding on a smooth curved surface of geometry, $y = f(x)$, restoring force, F_R, can be expressed by the following two equations as proposed by Pranesh and Sinha:[2]

$$F_R = mg\frac{dy}{dx} \tag{2}$$

and

$$F_R = m\omega_r^2 x; \tag{3}$$

where, ω_r is the isolator frequency and is equal to $\sqrt{\frac{g}{R}}$ (R, is the radius of curvature of the sliding surface). For the proposed isolator, radius R, and isolator frequency, ω_r, is varying and is a function of sliding displacement, x.

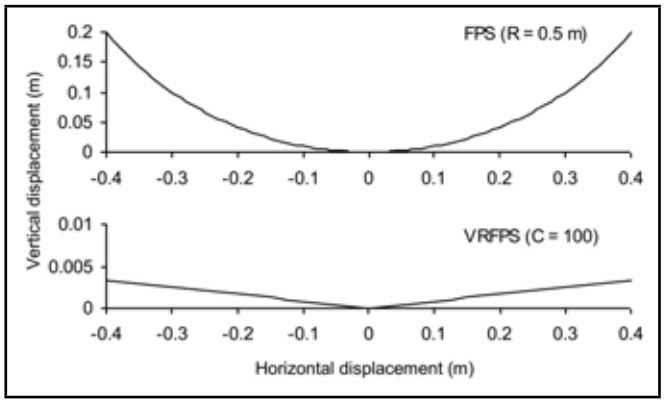

Figure 1. Geometry of VRFPS and FPS isolators.

From Eqs. (2) and (3):

$$\frac{dy}{dx}(x) = \frac{x}{R(x)}, \quad \text{i.e.} \quad \frac{dy}{dx}(x) = \frac{x}{C\left(\exp\left(x\right) - 1\right) + R};$$
$$y(x) = \int \frac{x\,dx}{C\left(\exp\left(x\right) - 1\right) + R}. \tag{4}$$

The above equation defines the geometry of the sliding surface. The vertical displacement, y, at sliding displacement, x, can be obtained by integrating the above equation numerically. Figure 1 shows the sliding surface of the VRFPS with the initial radius $R = 0.5$ m and $C = 100$. The sliding surface of the FPS with a constant radius $R = 0.5$ m is also shown in the same figure. The radius of curvature of the VRFPS increases as compared to the FPS while increasing the sliding displacement. Also, as evident from Fig. 1, the VRFPS is relatively flatter than the FPS.

3. ANALYTICAL MODELLING

Figure 2 shows the three-span continuous bridge considered for the study. The bridge is seismically isolated with the VRFPS between the superstructure and the pier and with the VFD between abutments and superstructure. The VRFPS is modelled as a fictitious spring of stiffness, k_b. The super structure between the supports, each pier, and each sliding bearing are considered as an element interconnected at the joints. One end of the spring is connected to the superstructure while the other end is connected to the top of the pier. When the system is in a non-sliding phase, the stiffness of the fictitious spring is considered as a large value so that the relative displacement between the super structure and the pier at the interface is zero whereas when the system is in sliding phase, the stiffness of the fictitious spring is considered as zero to allow the sliding of the super structure at the interface. The super structure, pier, and isolator are modelled as an element with one horizontal degree of freedom at each node. The stiffness matrix of the super structure, the stiffness of the pier, and the stiffness of the sliding bearing, k_b, are added to obtain the stiffness matrix, K, of whole bridge structure. The mass of the super structure and pier is lumped at the nodes. The overall dynamic equation of the equilibrium for the bridge structure can be expressed in matrix notation as

$$[M]\{\ddot{u}\} + [C]\{\dot{u}\} + [K]\{u\} = \{F(t)\}; \tag{5}$$

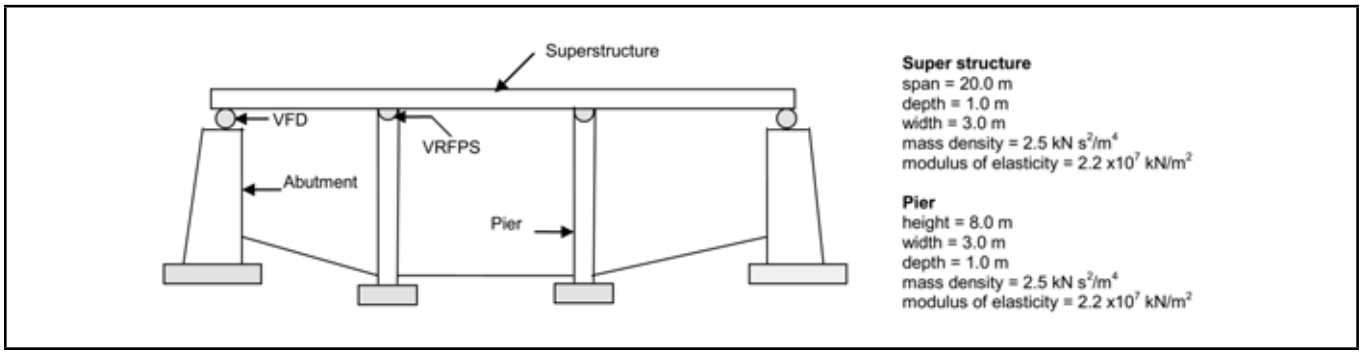

Figure 2. Three-span continuous bridge considered for the study.

where $[M]$ and $[C]$ are the mass matrix and damping matrix, respectively; $\{\ddot{u}\}$, $\{\dot{u}\}$, $\{u\}$ are the acceleration, velocity, and displacement vectors relative to the ground at nodes; $\{F(t)\}$ is the nodal load vector; and $\{u\} = \{u_1, u_2, u_3, \ldots, u_n\}$, where n is the number of nodes.

The nodal load vector $\{F(t)\}$ for the non-sliding phase, is obtained using the equation

$$\{F(t)\} = -[M]\{I\}\ddot{u}_g(t). \tag{6}$$

Whereas, for the sliding phase,

$$\{F(t)\} = -[M]\{I\}\ddot{u}_g(t) + \{F_r\}. \tag{7}$$

In this case, $\{I\}$ is the influence vector, and $\ddot{u}_g(t)$ is the ground acceleration. $\{F_r\}$ is the nodal load vector due to the isolator force. This force mainly consists of two components: i) restoring force due to the component of the weight of the superstructure on each isolator and ii) the frictional force. Frictional force, F_s, is the maximum frictional resistance offered by the sliding surface and is equal to the product of the weight of the superstructure, W, on each isolator and the friction coefficient μ (i.e. $F_s = \mu W$). The restoring force is the product of the stiffness of the isolator (due to gravity) and relative displacement between the super structure and the pier.

At the degrees of freedom corresponding to the super structure,

$$F_r = -k_r u_r - F_s \operatorname{sgn}(\dot{u}_r); \tag{8}$$

and at the degrees of freedom corresponding to the pier,

$$F_r = k_r u_r + F_s \operatorname{sgn}(\dot{u}_r); \tag{9}$$

where k_r is the stiffness of isolation provided through its gravity ($k_r = m\frac{g}{R(x)}$). u_r and $\dot{u}_r$ are the displacement and velocity of the superstructure relative to the pier (i.e., $u_r = u_{\text{super structure}} - u_{\text{pier}}$); sgn denotes the signum function.

4. NUMERICAL EXAMPLES

An example of a three-span continuous bridge has been considered in order to study the effectiveness of the proposed hybrid isolator system as shown in Fig. 2. The bridge is isolated between the pier and the superstructure using the VRFPS isolator, and a supplementary damping is provided using the VFD between the abutment and the pier. Geometric and material properties considered for the study are shown in Fig. 2. The time period of the non-isolated bridge is equal to 0.47 s. The damping ratio of the bridge is 5 percent, and the coefficient of friction of the sliding material is 0.05. The isolator constant, $C = 100$ and initial radius, $R = 0.5$ m are considered for the proposed VRFPS isolator. For comparison, the FPS with a radius 0.5 m (time period, $T = 1.43$ s) is considered. Acceleration records used for numerical simulation are the three commonly used earthquake ground motions. They are:

i) N-S component of El Centro earthquake (Imperial Valley, 1940)

ii) E-W component of Northridge earthquake (Newhall, 1994)

iii) Chi-Chi earthquake at station TCU075 (Taiwan, 1999)

The wave forms of these three records are shown in Figs. 3a, 3b, and 3c. The first record of the El Centro earthquake shown in Fig. 3a has been used to simulate the response of many earthquake engineering structures. Since the El Centro earthquake has no long period characteristics, it is used to represent a far-field earthquake in this study. On the other hand, the Northridge and Chi-Chi earthquakes shown in Figs. 3b and 3c exhibit a long period pulse like wave forms, and hence, these two earthquakes are used in this study to represent the near-fault earthquakes. In order to show the effectiveness of the VRFPS to the earthquake ground motion, the base shear at the pier foot along with the sliding displacement of the superstructure and the residual displacement of the isolator are examined. The base shear is directly proportional to the forces exerted in the bridge system due to the earthquake ground motion. On the other hand, the sliding displacement of the super structure is crucial from the design point of view of the isolation system and the expansion joints.[13] Residual displacement is the displacement of the isolator relative to the displacement of the pier at the end of earthquake. For isolation to be effective, residual displacement is needed to be minimal. Residual displacement equal to zero ensures that the superstructure comes to its original position at the end of earthquake. In the first step, the performance of the VRFPS isolator considered for the present study without the VFD is compared with the performance of the FPS isolator without the VFD to investigate the advantages of the proposed VRFPS isolator system with a conventional FPS. In the next step, the effect of adding a VFD to the VRFPS isolator is studied. The performance of the VRFPS with a VFD is also compared with the performance of the FPS with a VFD to investigate the relative advantages of a VRFPS over a FPS after adding additional damping using the VFD. A parametric study by varying the damping coefficient

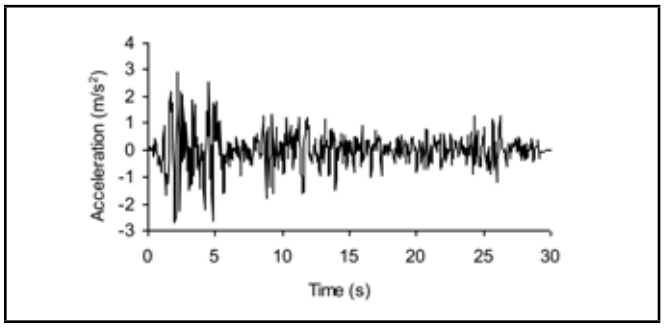

Figure 3a. El Centro earthquake.

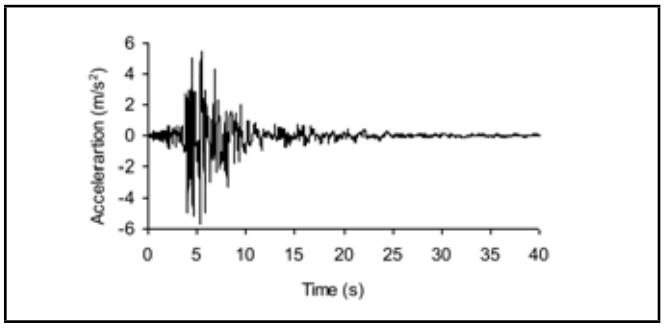

Figure 3b. Northridge earthquake.

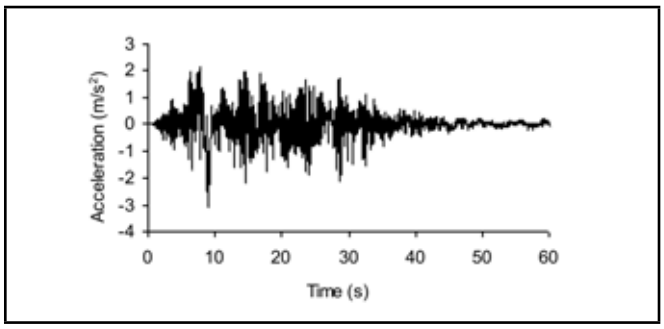

Figure 3c. Chi-Chi earthquake.

of the VFD is also carried out to investigate the efficiency of the proposed system for various values of the damping coefficients. For this, the performance of the VRFPS with a VFD is compared with the performance of the FPS with a VFD at various damping coefficients of the VFD.

4.1. Effect of Geometry of the Sliding Surface

The geometrical property of the proposed isolator is defined by the isolator constant, C, in Eq. (1). The effect of C on the performance of the isolator is studied for the Chi-Chi earthquake ground motion. Figure 4 shows the peak response of the base shear, sliding displacement, and residual displacement for various values of C. As shown in the figure, the base shear is comparatively larger and the residual displacement is nearly equal to zero at lower values of C. The base shear decreases, and the residual displacement increases with an increase in the value of C. The sliding displacement is comparatively larger for the values of C, ranging from 5 to 50. Based on the criteria of a low base shear and a small residual displacement, the value of C from 50 to 200 is recommended for the proposed isolator. For the present analysis, the value of C equal to 100 is considered.

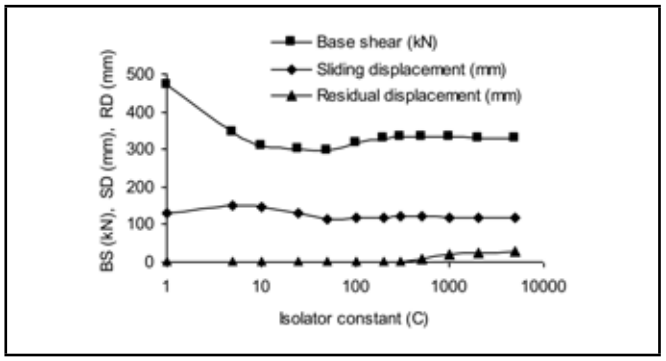

Figure 4. Variation of response with isolator constant.

4.2. Time History Response of the Isolated Bridge without VFD

The time history response obtained for a bridge structure isolated with a VRFPS only (i.e. without VFD) is presented in Figs. 5a, 5b, 5c, and 5d. For comparison, the time history response of a bridge isolated with a FPS without the VFD is also shown in the same figures. In this case, the response for the El Centro earthquake is obtained for two cases. The first case is for the recorded ground acceleration (medium intensity) whereas for the second case, the recorded ground acceleration is multiplied by an intensity factor of 2.0 (high intensity). Comparison of the response of the VRFPS with a FPS shows that the base shear is almost similar for both the systems for the El Centro earthquake of medium intensity whereas the bridge with the VRFPS experiences a significantly lower base shear for the high intensity El Centro earthquake, Northridge earthquake, and Chi-Chi earthquake. This indicates that the far-field excitations of high intensity and the near-fault excitations severely affect the performance of the FPS isolator. Interestingly, the peak base shear for the VRFPS is almost similar (varies from 223.2 kN–371.6 kN for VRFPS against 277.6 kN–682.9 kN for FPS) for all the four excitations, clearly demonstrating the advantages of the VRFPS to overcome the resonance problem that occurs in a FPS and its effectiveness for excitations of high intensity and for near-fault earthquakes. The time history response of sliding displacement shows a slightly larger maximum displacement for the VRFPS compared to the FPS. However, the residual displacement for both the systems is identical and is almost equal to zero, clearly demonstrating their ability to bring the structure to its original position. Thus, it is evident that the VRFPS isolator is more effective than the FPS isolator since the VRFPS reduces the base shear significantly for high intensity and near-fault earthquakes without much of an increase in the sliding displacement. The VRFPS is also effective in restoring the structure to its original position.

4.3. Time History Response of the Isolated Bridge with the VFD

It may be noted from the Figs. 5b, 5c, and 5d that the structure isolated with the VRFPS and FPS isolators slides considerably during the earthquake. Moreover, the sliding displacement of the VRFPS isolator is larger than that of the FPS isolator. For the isolation to be effective, the sliding displacement is to be within the limit. Hence, to reduce the sliding displace-

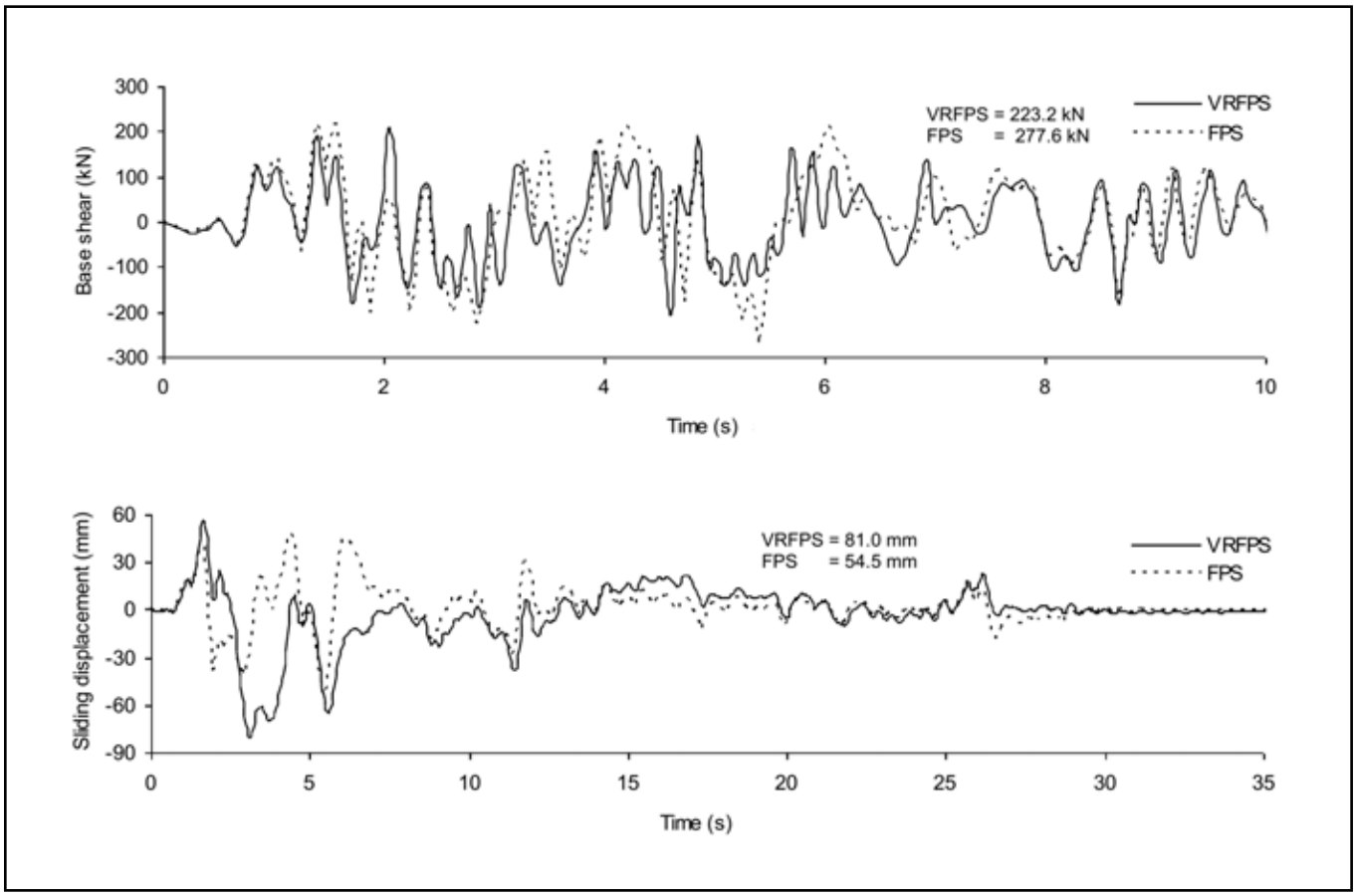

Figure 5a. Response of isolated bridge without VFD to El Centro earthquake of medium intensity.

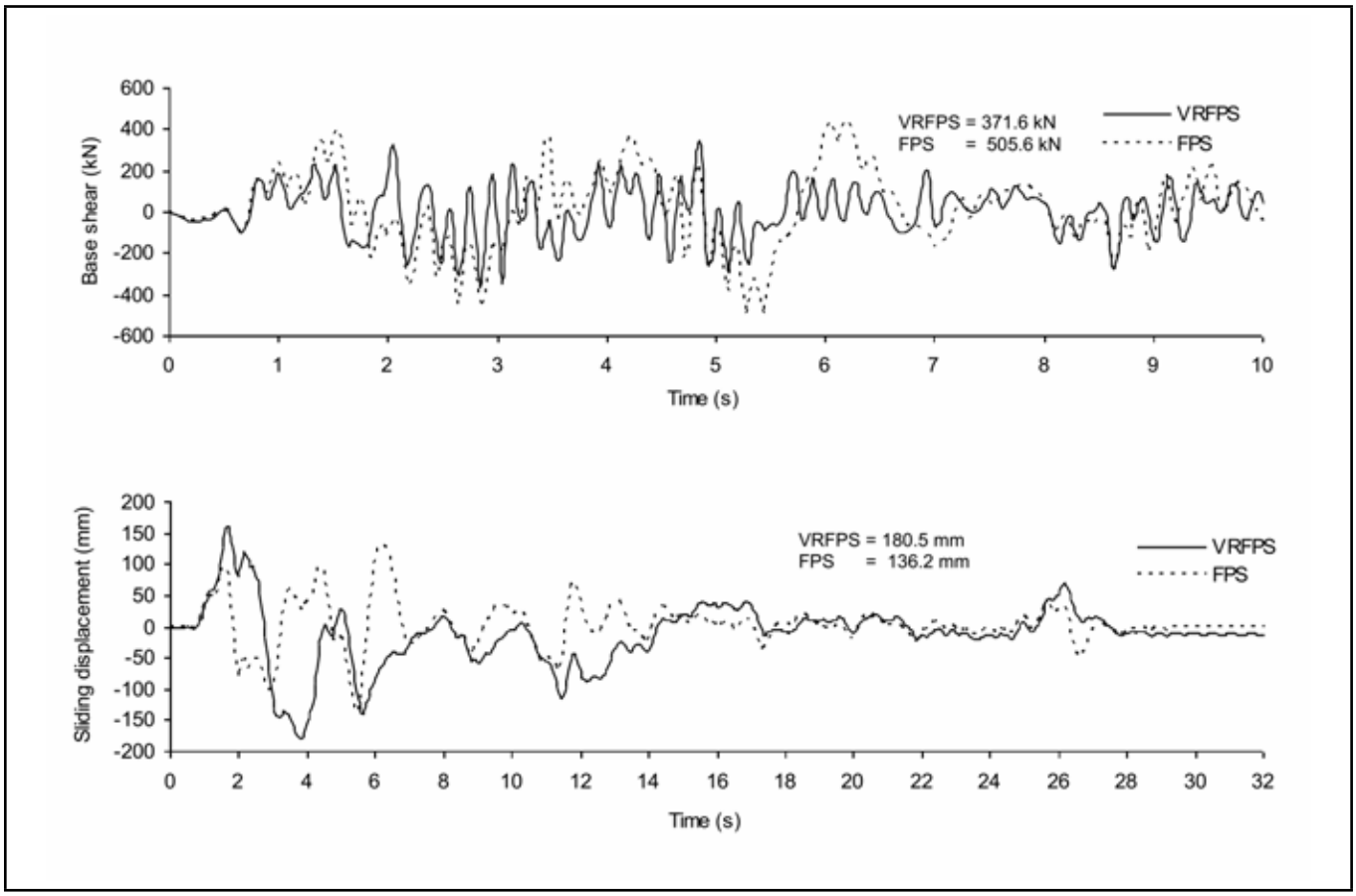

Figure 5b. Response of isolated bridge without VFD to El Centro earthquake of high intensity.

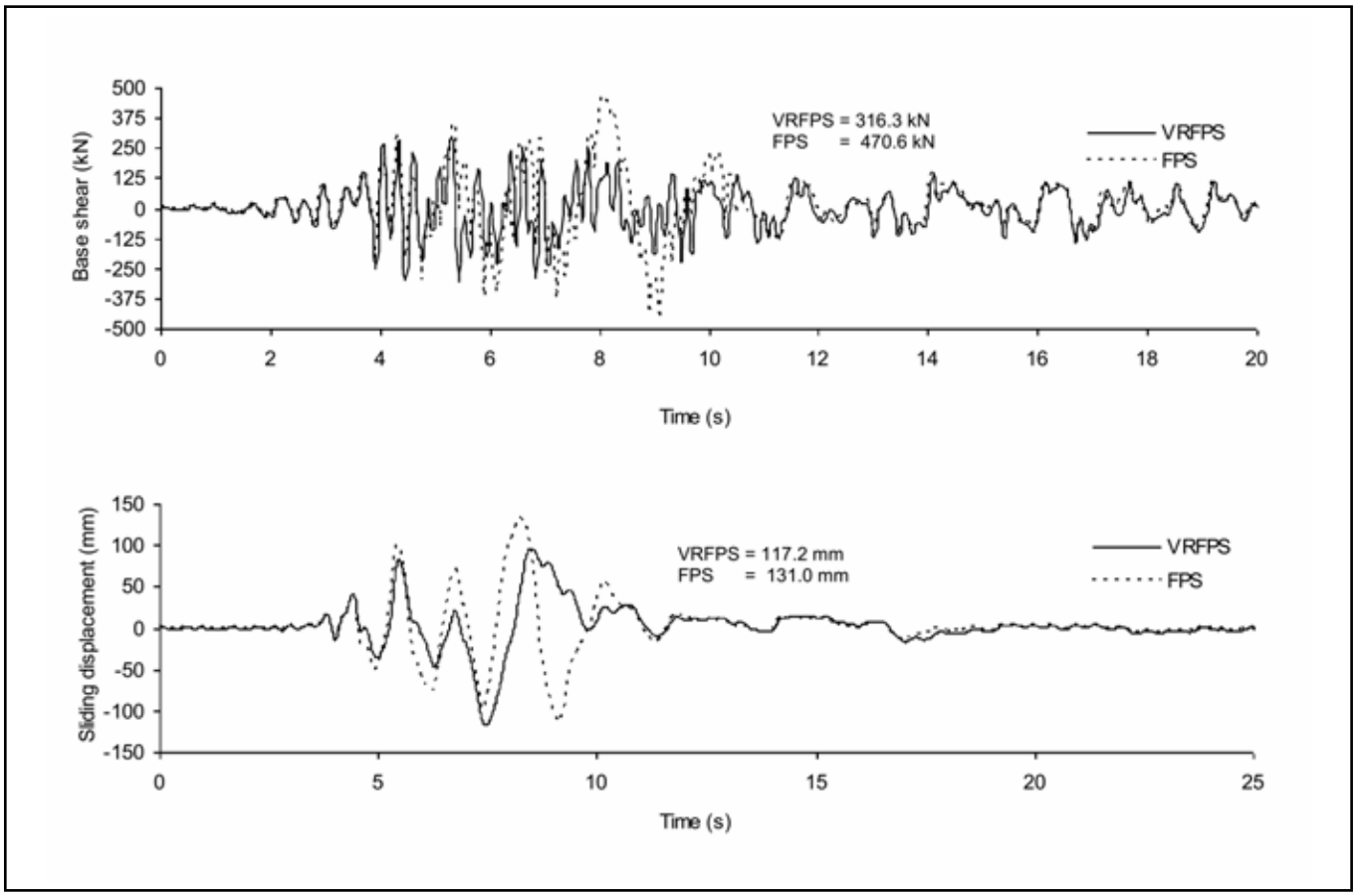

Figure 5c. Response of isolated bridge without VFD to Northridge earthquake.

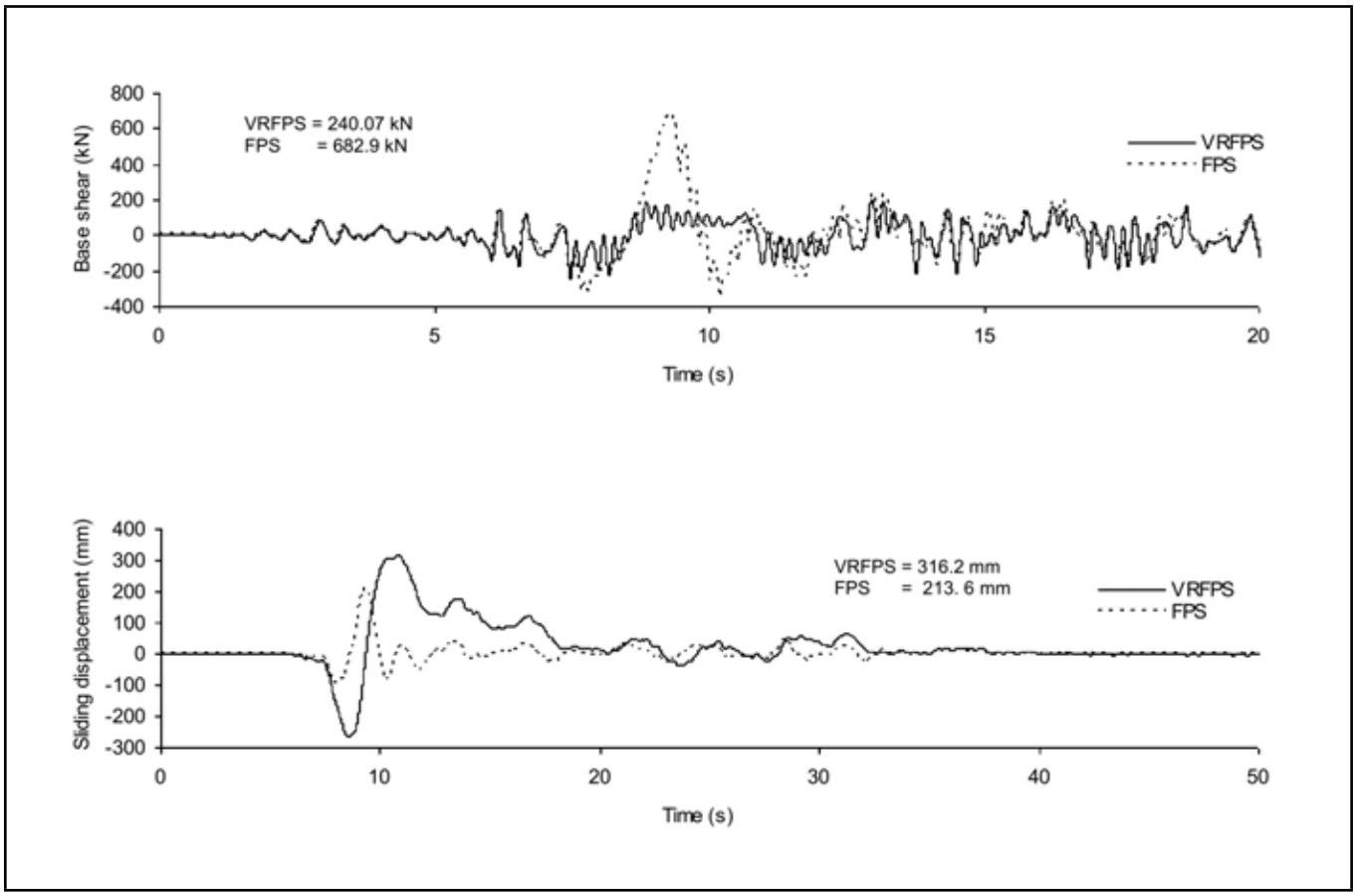

Figure 5d. Response of isolated bridge without VFD to Chi-Chi earthquake.

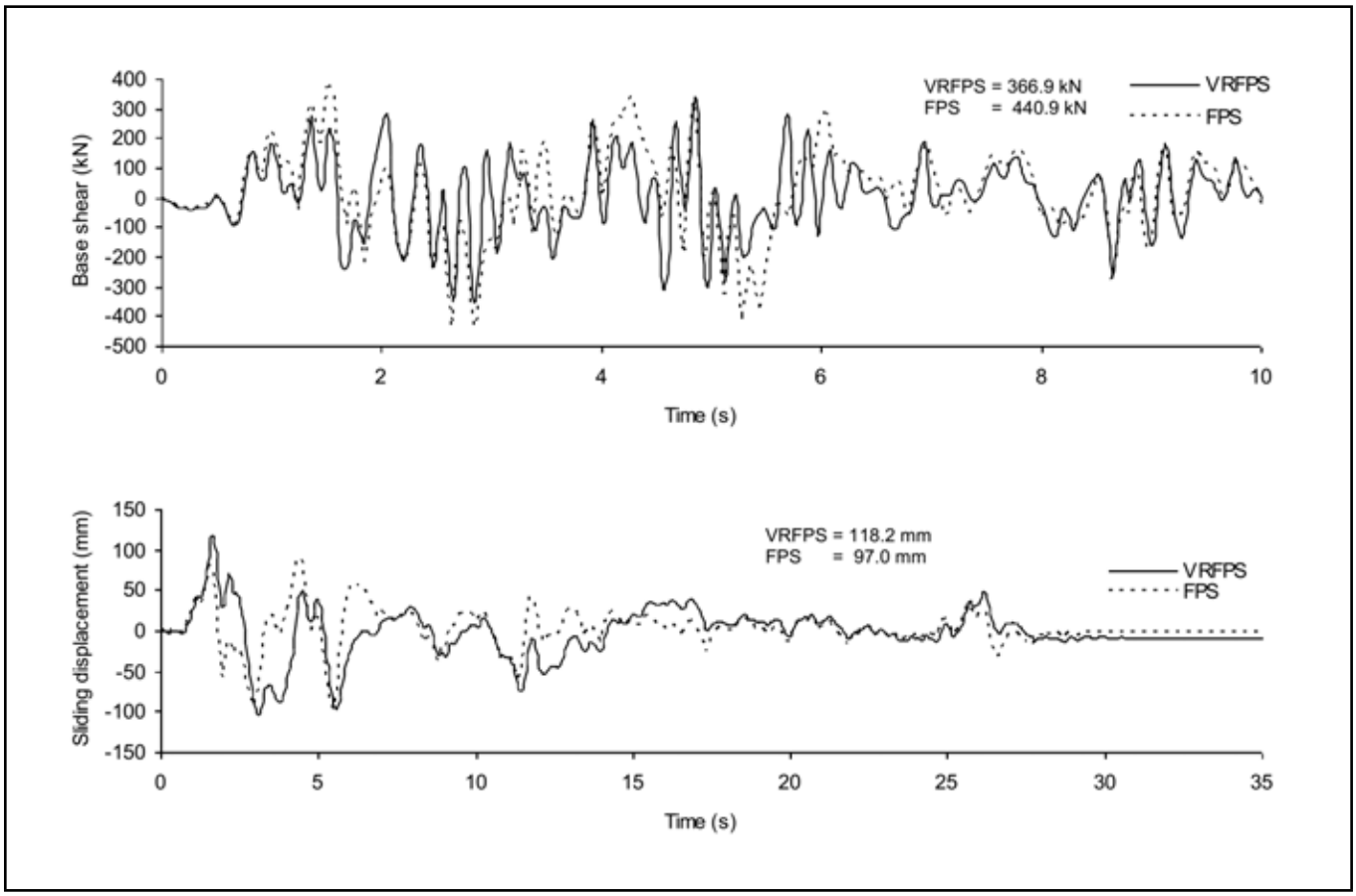

Figure 6a. Response of isolated bridge with VFD to El Centro earthquake of high intensity.

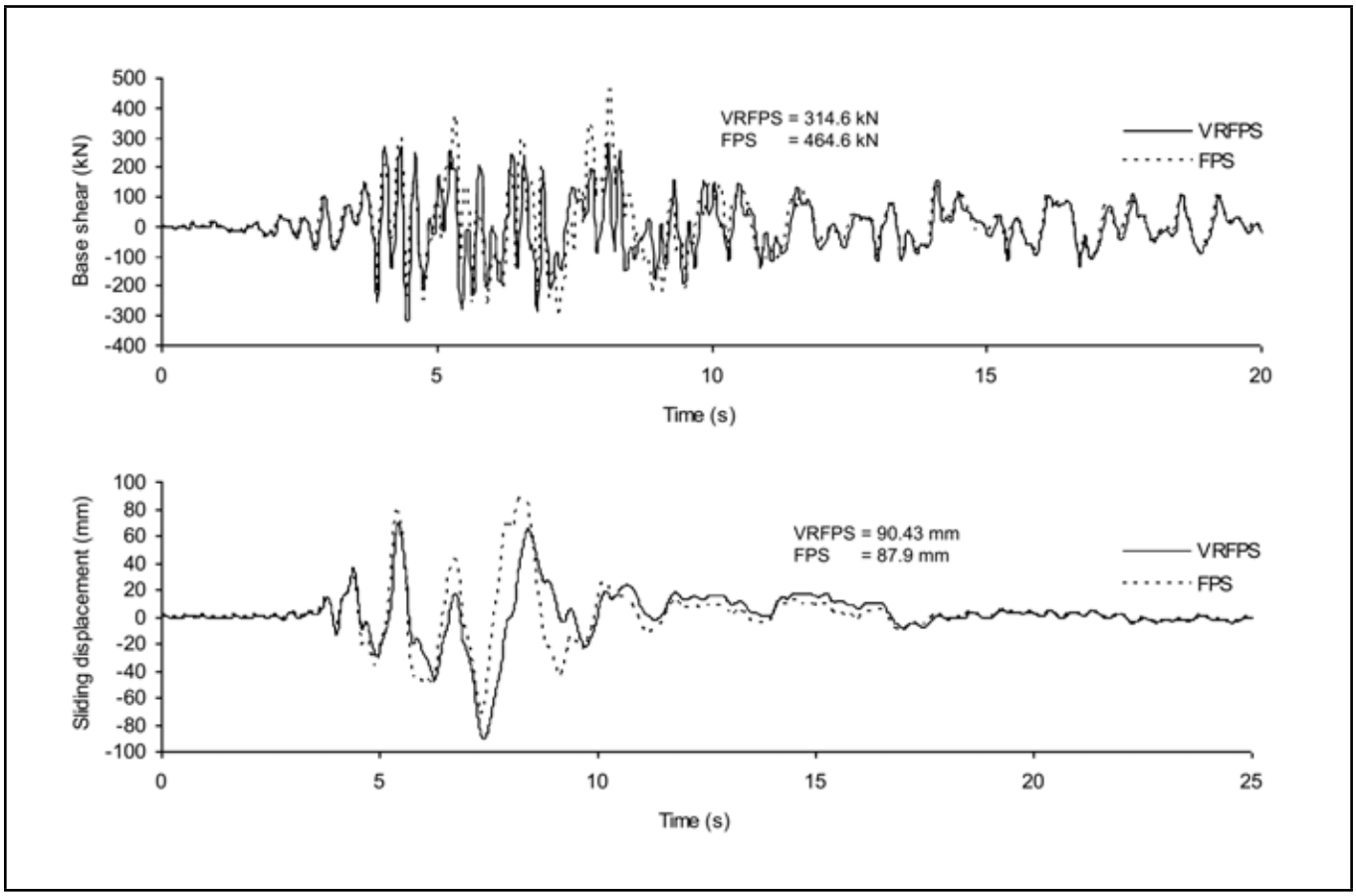

Figure 6b. Response of isolated bridge with VFD to Northridge earthquake ground motion.

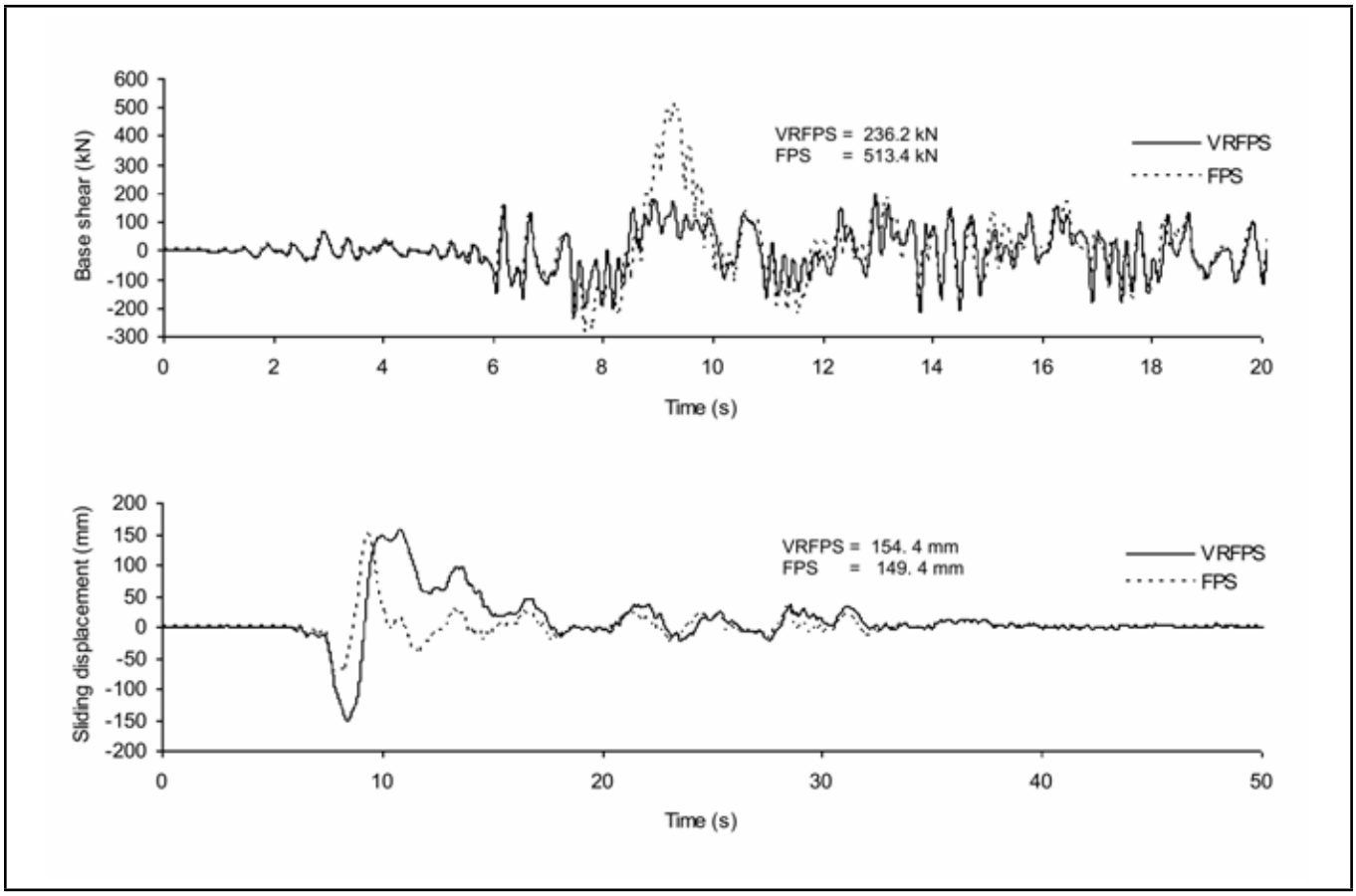

Figure 6c. Response of isolated bridge with VFD to Chi-Chi earthquake.

ment, a VFD system is placed between the superstructure and abutment, as already explained. The damping coefficient equal to 400 kNs/m is considered for the VFD. The time history response of the isolated bridge with the VFD system is shown in Figs. 6a, 6b, and 6c. It can be observed from the Figs. 5b, 5c, and 5d, and Figs. 6a, 6b, and 6c that the reduction in the displacement response is remarkable for the isolated bridge due to the addition of a passive hybrid system. Without the VFD, the sliding displacement of the VRFPS is larger than that of the FPS for the El Centro and the Chi-Chi earthquakes whereas for the Northridge earthquake, the sliding displacement of the FPS is larger than that of the VRFPS. However, the sliding displacement of both the systems is almost similar when additional passive damping is added for the VRFPS and the FPS isolators. The base shear reduces slightly due to the addition of the VFD for the FPS whereas for the VRFPS, the base shear will not change much due to the addition of the VFD. Overall, it can be observed from the time history plot of Figs. 6a, 6b, and 6c that the base shear of the bridge with the VRFPS is considerably lesser than that of the bridge with a FPS at an almost similar sliding displacement. Hence, again, a hybrid system consisting of the VRFPS and the VFD is more effective than a hybrid system consisting of the FPS and the VFD since the base shear of the bridge with the VRFPS is considerably lesser than that of a bridge with the FPS at an almost similar sliding and residual displacement when a passive hybrid, a VFD system, is added. The combined property i) variable frequency of the FPS and ii) additional damping of the VFD is effective to reduce the base shear of the FPS without increasing the sliding and residual displacement.

4.4. The Seismic Response of an Isolated Bridge with the VFD for a Various Damping Coefficient of the VFD

The effectiveness of a hybrid system consisting of the VRFPS isolator and the VFD to isolate the bridge structure is investigated for various values of the damping coefficient of the VFD. In addition to the base shear, sliding displacement, and residual displacement, the effectiveness of the proposed system for deck acceleration (acceleration of superstructure) is also investigated in this study. In the case of bearings with additional viscous dampers, relatively large forces may develop in dampers, and correspondingly large forces may be transmitted through the damper connections to the abutments and superstructure. Hence, the effect of the damping coefficient on the damping force is also considered for this study. Also, in this case, the response of the VRFPS is compared with the response of the pure friction (PF) system. Figures 7a, 7b, and 7c show the base shear, deck acceleration, sliding displacement, damping force, and residual displacement for various values of the damping coefficient. The damping coefficient of the VFD is varied from 0 to 1000 kNs/m. The corresponding variation of the damping ratio is from 0 to 0.9 for the FPS isolator. It may be noted that due to the variation in stiffness with sliding displacement, the damping ratio is not constant for the VRFPS during the earthquake. Hence, the responses in these figures are plotted in terms of the damping coefficient instead of the damping ratio. In these figures the response of the bridge at a zero damping coefficient corresponds to the response of the bridge isolated only with the VRFPS isolator (i.e. without the

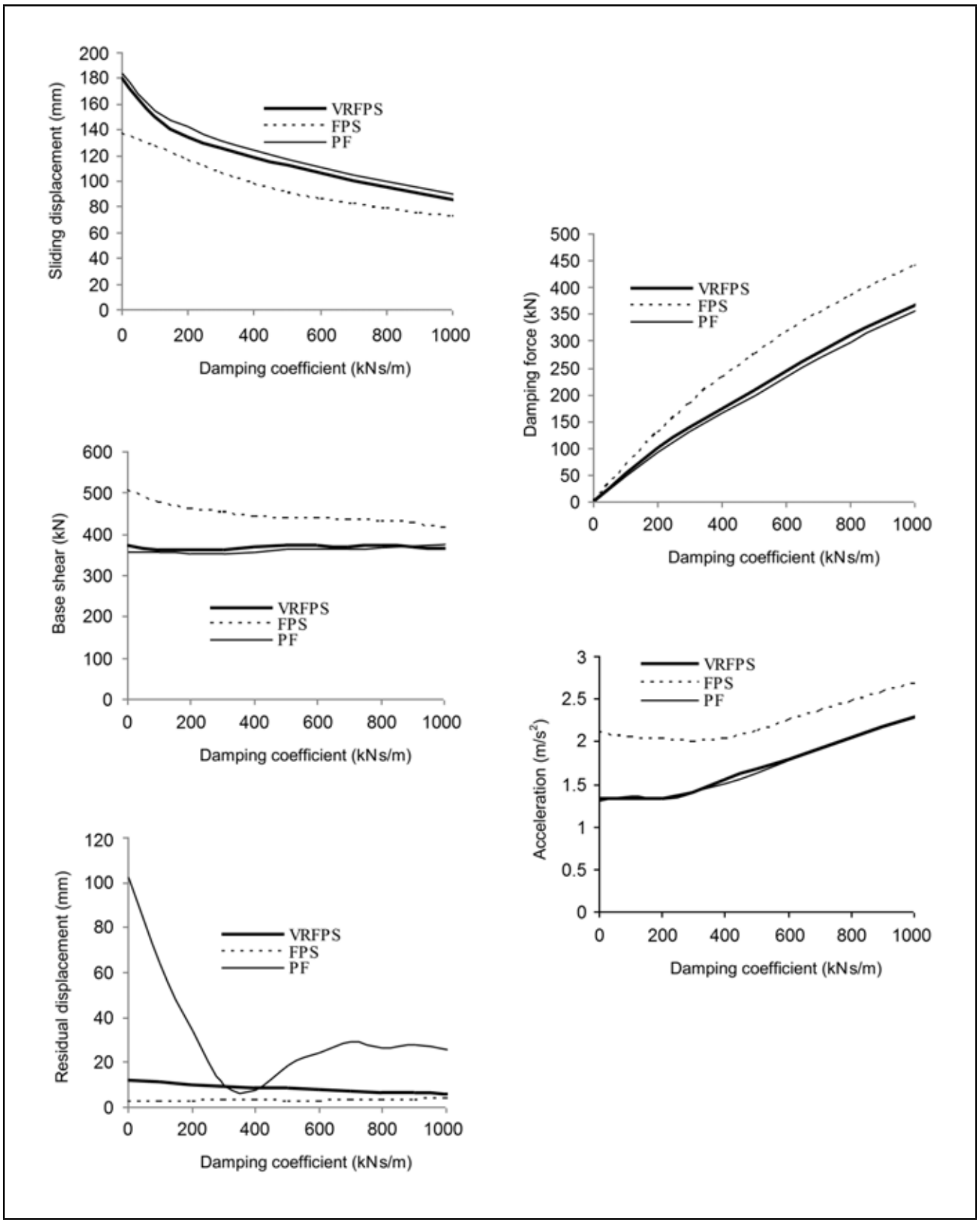

Figure 7a. Variation of response with damping coefficient for El Centro earthquake of high intensity.

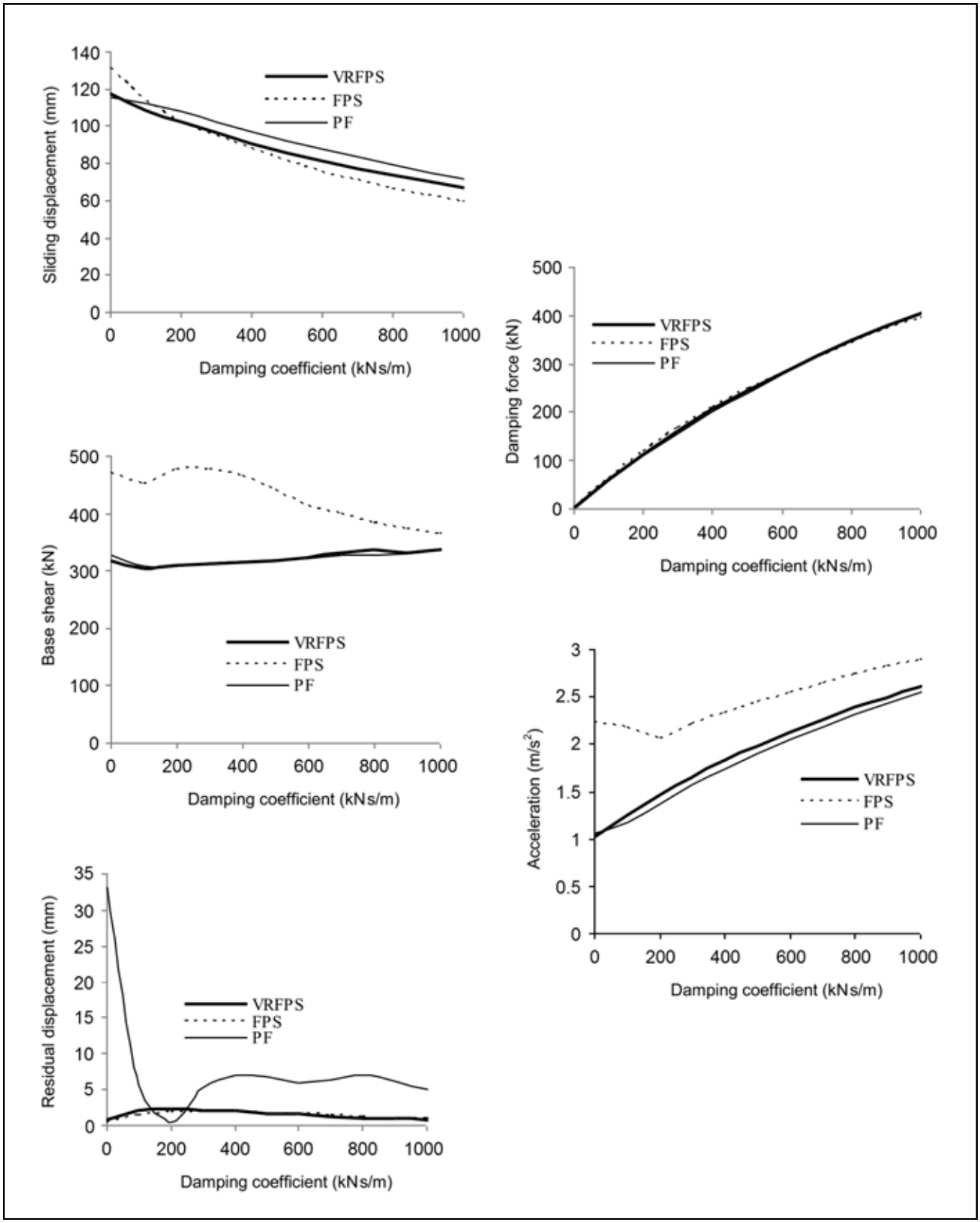

Figure 7b. Variation of response with damping coefficient for Northridge earthquake.

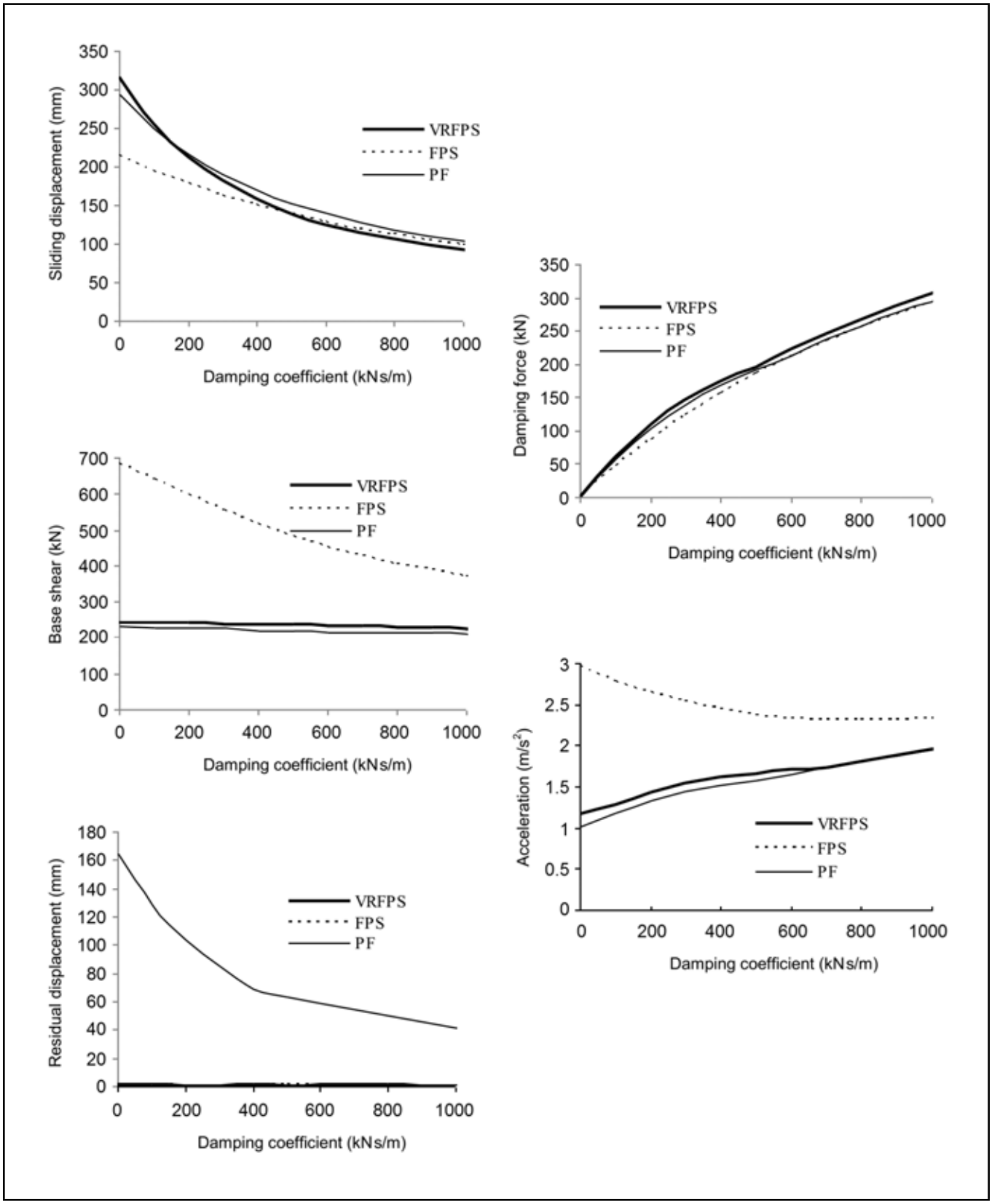

Figure 7c. Variation of response with damping coefficient for Chi-Chi earthquake.

VFD). From Figs. 7a, 7b, and 7c, the significant characteristic of all the three isolators is the sharp reduction in the sliding displacement with the damping coefficient. Without the passive damping system, the sliding displacement of the VRFPS is more than that of the FPS for the El Centro and Chi-Chi earthquake whereas for the Northridge earthquake, the sliding displacement of the FPS is more than that of the VRFPS. However, at a damping coefficient of about 400 kNs/m (corresponding to the damping ratio of 0.3 for FPS), the sliding displacement of both the isolators is almost similar. The response of the base shear shows that the base shear for the FPS decreases with an increase in the damping coefficient, reaches a minimum value, and then remains almost constant. However, for the VRFPS, the base shear will not vary much with the damping coefficient. The deck acceleration for the FPS initially decreases marginally, reaches a minimum value, and then increases with a further increase in the damping coefficient. The deck acceleration for the VRFPS, however, increases with an increase in the damping coefficient and is lesser compared to the deck acceleration of the FPS for all the values of the damping coefficient. Thus, combining the response of the base shear, deck acceleration, and sliding displacement, it is noteworthy that, for the damping coefficient more than about 400 kNs/m, the base shear and the deck acceleration of the VRFPS is considerably lesser than that of the FPS at an almost similar sliding displacement. The response of the VRFPS and the PF system shows that the base shear, deck acceleration, and sliding displacement of both the PF and the VRFPS are almost similar. However, the residual displacement is considerably larger for the PF system than that of the VRFPS. The VRFPS brings the structure to its original position whereas, the structure isolated with the PF system displaces considerably from its original position after the earthquake. The response of the damping force at various damping coefficients shows that the damping force increases with the damping coefficient, and the variation of the damping force with the damping coefficient is similar for all the three types of isolators.

5. CONCLUSIONS

The effectiveness of a variable radius friction pendulum system (VRFPS) with an additional passive viscous fluid damper (VFD) to control the seismic response of a continuous bridge is studied. The performance of the proposed isolator is compared with the performance of a conventional friction pendulum system (FPS) and a pure friction (PF) system. The VRFPS does not show any resonance problem that occurs in a FPS for near-fault earthquake ground accelerations. However, the sliding displacement of the VRFPS is slightly more than the sliding displacement of the FPS due to the relatively flatter surface of the VRFPS than the FPS at a large sliding displacement. By adding a passive VFD system to the VRFPS, the sliding displacement decreases considerably, and its effectiveness increases further. In this case, the sliding displacement of both the FPS and the VRFPS systems is similar but the base shear and the deck acceleration for the VRFPS is considerably lesser than that of the FPS. Similar to the FPS, the VRFPS is also effective in bringing the structure to its original position after the earthquake. The base shear, deck acceleration, and sliding displacement of the VRFPS is similar to the PF system. However, the residual displacement of the PF system is considerably larger than the VRFPS. The VRFPS has the advantages of both the FPS and the PF system.

REFERENCES

[1] Zayas, V. A., Low, S. S., and Mahin, S. A. A simple pendulum technique for achieving seismic isolation, *Earthquake Spectra*, **6** (2), 317–333, (1990).

[2] Pranesh, M. and Sinha, R. VFPI: an isolation device for aseismic design, *Earthquake Engineering & Structural Dynamics*, **29** (5), 603–627, (2000).

[3] Lu, L. Y., Wang, J., and Hsu, C. C. Sliding isolation using variable frequency bearings for near-fault ground motions, *Proc. of the fourth International Conference on Earthquake Engineering*, Taipei, Taiwan, (2006).

[4] Tsai, C. S., Chiang, T. C., and Chen, B. J. Finite element formulations and theoretical study for variable curvature friction pendulum system, *Engineering Structures*, **25** (14), 1719–1730, (2003).

[5] Tsopelas, P. C., Constantinou, M. C., Okamota, S., Fujii, S., and Ozaki, D. Experimental study of bridge seismic sliding isolation systems, *Engineering Structures*, **18** (4), 301–310, (1996).

[6] Soneji, B. B. and Jangid, R. S. Passive hybrid systems for earthquake protection of cable-stayed bridge, *Engineering Structures*, **29** (1), 57–70, (2007).

[7] Symans, M. D. and Kelly, S. W. Fuzzy logic control of bridge structures using intelligent semi-active seismic isolation systems, *Earthquake Engineering & Structural Dynamics*, **28** (1), 37–60, (1999).

[8] Yoshioka, H., Ramallo, J. C., and Spencer, B. F. "Smart" base isolation strategies employing magnetorheological dampers, *Journal of Engineering Mechanics*, **128** (5), 540–551, (2002).

[9] Kim, H. S. and Roschke, P. N. Design of fuzzy logic controller for smart base isolation system using genetic algorithm, *Engineering Structures*, **28** (1), 84–96, (2006).

[10] Jung, H. J., Choi, K. M., Spencer, B. F., and Lee, I. W. Application of some semi-active control algorithms to a smart base-isolated building employing MR dampers, *Structural Control and Health Monitoring*, **13** (2–3), 693–704, (2006).

[11] Lu, L. Y., Lin, G. L., and Kuo, T. C. Stiffness controllable isolation system for near-fault seismic isolation, *Engineering Structures*, **30** (3), 747–765, (2008).

[12] Krishnamoorthy, A. Variable curvature pendulum isolator and viscous fluid damper for seismic isolation of structures, *Journal of Vibration and Control*, **17** (12), 1779–1790, (2011).

[13] Jangid, R. S. Stochastic response of bridges seismically isolated by friction pendulum system, *Journal of Bridge Engineering*, **13** (4), 319–330, (2008).

An Investigations of Sound Absorbance Properties of Weft Knitted Spacer Fabrics

Erhan Sancak

Marmara University Technology Faculty, Department of Textile Engineering, Istanbul, Turkey

(Received 2 November 2013; revised 22 March 2014; accepted 30 April 2014)

Nonwoven fabrics have been used for many years in different technical applications; they have particularly been used as isolation materials in vehicles in order to reduce the noise heard within them, and they. They have achieved great popularity due to low production cost and good absorbance. However, the fabrics produced by making use of the nonwoven technique have some disadvantages including low resistance, low abrasion strength, poor aesthetic appearance and thickness. In order to eliminate these disadvantages, recent studies have reported that knitted fabrics could be an alternative to nonwoven fabrics. Various studies have focused on the impact on sound absorbance that the thickness and surface structure of knitted fabrics have. In this study, a number of knitted spacer fabrics, which had five different connection angles, were manufactured by using a plain knitting machine. The sound transmission loss levels of the developed fabrics were tested and analysed by Brüel and Kjaer tube instruments. At the end of the examinations, the sound absorbance behaviors at different frequencies were demonstrated in graphics based on the type of knitting. It was determined in the study that three factors have a major impact on the sound absorbance behaviour; thickness of fabric, micro porosity between fabric surfaces and yarn linear density in the interconnection of the fabrics.

1. INTRODUCTION

In humans, the audible range of sound frequencies is usually 20 Hz to 20.000 Hz. For a sound to be heard, the sound intensity should reach a certain level. Human sounds usually cover the frequencies of 250-500-1000-2000 Hz. If these audio waves appear in a random spectrum or, in other words, if they are undesired sounds, they are called "noise".

In parallel to technological advancements, the development of metropolitan regions, and the lightening of structures, environmental impacts that affect humans are also on the rise. One of these notable impacts is the sound pollution, or environmental noise, which is irritating, undesirable, and uncomfortable. In addition to the discomfort that it causes, it also has negative impacts on the psychology, physiology, and performance of humans. Besides, noise can result in behavioral disorders, decline in working performance, hearing loss, tinnitus and psychological diseases.

In the urbanized and mobilized life style of today's world, the time spent within cars has increased. Thus, sound insulation has gained an increasing importance in the automobile industry for both the comfort of driver and the health of passenger. With the increase in the power of engines used in the automobile industry, low-frequency sound within the car has appeared to be a problematic area that needs to be resolved. Although this frequency range is generally below 4000 Hz, sounds in the range of 100–1000 Hz cause passengers to feel tired.[1]

If a sound encounters an obstacle while propagating in a medium, it behaves in three different manners as in the case of other physical phenomena. A certain part of the sound reflects from the obstacle, and the obstacle absorbs a certain amount of it while the rest passes through the obstacle. Therefore, each material has a specific absorbance coefficient. As textile materials are porous structures, they allow sound absorbance. Thus, they are used in a wide range of applications including acoustic panels used in workplaces, insulation materials for automobiles and furnishing fabrics in the concert halls.[3,4]

In industrial applications, fibreglass, foam, mineral fibres and their composite materials are used for sound insulation.

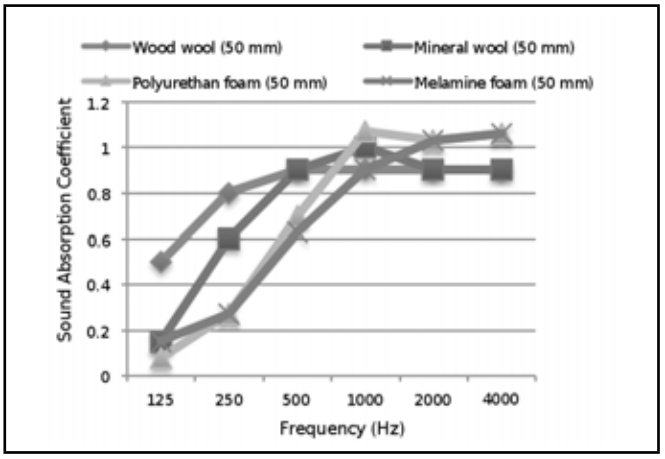

Figure 1. Sound Absorbance Behaviours of Certain Materials.[2]

Even though these materials have good heat and sound insulation properties, they have negative impacts in terms of environmental pollution and human health.

In the transportation sector, manufacturers have used three main methods for sound control and sound reduction within the car. These are the reduction of sound and vibration sources, establishing anti-sound barriers between the passenger and the sound source, and using absorbent materials for sound propagation inside and outside the car.[2]

Nonwoven textile fabrics are commonly used in automobiles for sound insulation, as they are cost effective. However, it is less likely to manufacture nonwoven textile products as preformed or in the desired form. On the other hand, knitted fabrics have an aesthetic appearance, and they provide the opportunity to be manufactured in the desired form. The sound insulation capacity of single-plate knitted fabrics is poor.[1] Thus, it is more appropriate to use double plate special patterned fabrics in the knitted fabrics for sound insulation.

Two different conclusions were drawn at the end of the measurements of the sound absorbance coefficients of the different spacer fabrics, which were manufactured out of 972 dtex yarn with double polyamide coating in the exterior face and elas-

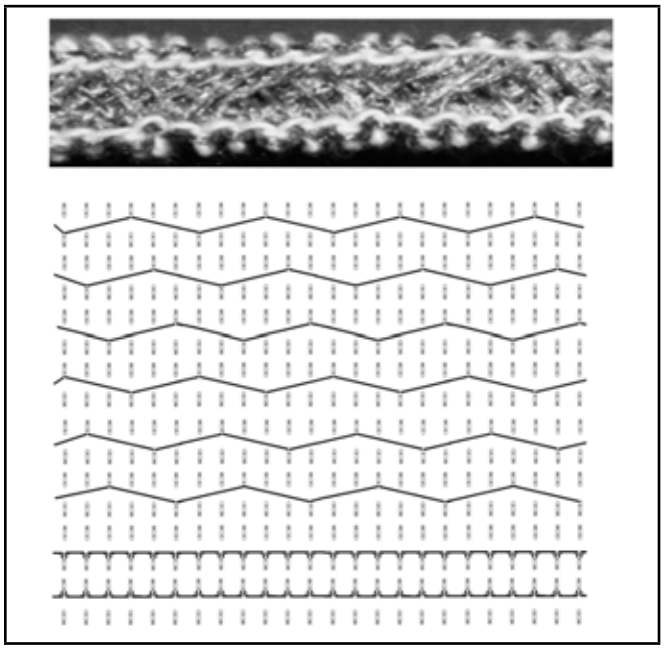

Figure 2. Technical drawings and photographs of sample fabric knits (SF-A).

tomeric material in the inner face both at the front and reverse sides and out of 430 dtex and 380 dtex polyester yarns in the interconnections. The first conclusion was that the sound absorbance coefficient increased in direct proportion to the thickness of the fabric. Secondly, it was detected that the sound absorbance coefficient increased with the decline of spaces in the front and reverse sides of the fabrics.[5]

200 dtex tencel, 167 dtex textured polyester, and 972 dtex textured polyester yarns were used in the front and reverse sides of six different spacer fabric samples. In the inter connections, 167 dtex textured polyester yarn was used. It was determined that the sound absorbance capacity tended to decrease as a result of the decrease in the surface porosity and increase in the surface density. It was also concluded that the fabric surface density was more dominant than the fabric thickness in sound absorbance.[6]

It was determined that in single jersey fabrics manufactured with polyester yarns at different loop densities, the sound absorbance capacity of the fabric with a larger space in the surface was higher than that of the fabric with a smaller space in the surface.[1] It was observed that the increases in the spaces and the thickness in the three different spacer fabrics, manufactured by using cotton yarn in the front and reverse sides and polyester yarn in the inter connections, occurred in direct proportion to the sound absorbance.[4]

2. MATERIALS

2.1. Yarn Properties

In this research, 100% Cotton Ne5/1 yarn was used in the front and reverse sides of the sample fabrics. 700 denier 100% acrylic continuous filament yarns were used in the inter connections. Prior to producing the spacer fabric structures, the fibres were conditioned for 48 h in 65% relative humidity and 20°C temperature. The physical properties of five different spacer fabrics used in the research are given in Table 1.

2.2. Fabric Constructions

The STOLL CMS (420 model no. E7) plain knitting machine was employed during the production of the fabric structures. The spacer knits with five different inter connections

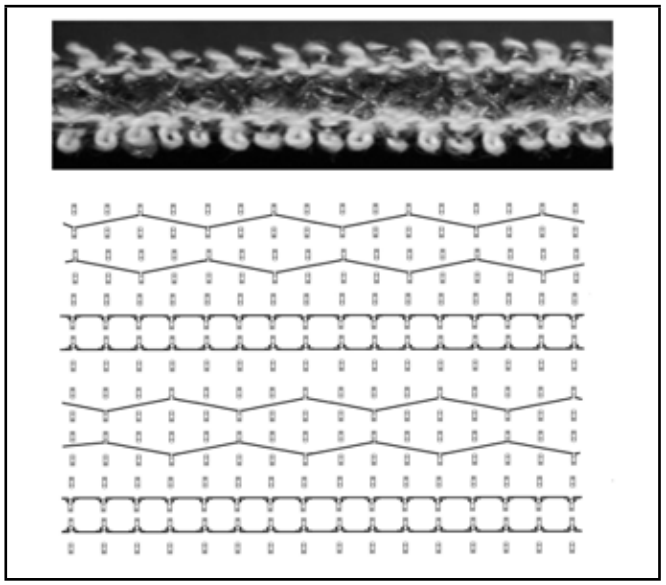

Figure 3. Technical drawings and photographs of sample fabric knits (SF-B).

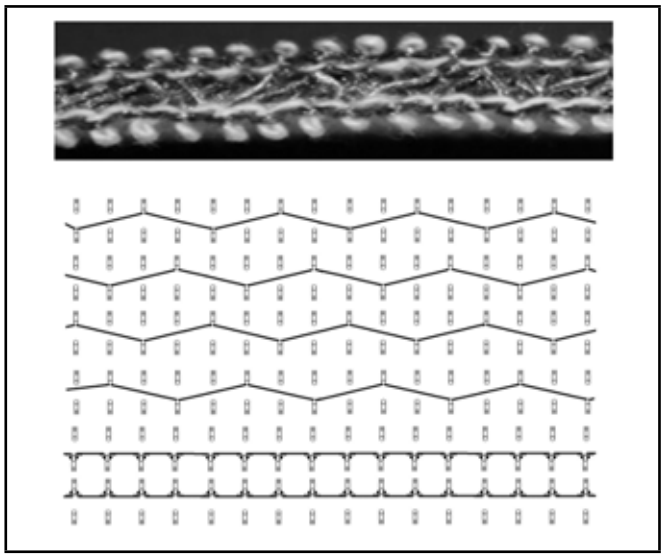

Figure 4. Technical drawings and photographs of sample fabric knits (SF-C).

were developed, and the technical drawings and the surface appearances of the patterns produced are shown in Figs. 2–6.

2.3. Measuring of Sound Absorptions

2.3.1. Theory

The use of impedance tubes for measuring the TL values of different materials has been developed in recent years. The technique was initially introduced to measure the TL of muffler systems but since has been modified for TL measurement of different materials. The theoretical principle behind this is based on the transfer matrix method.

The complex amplitudes of the sound pressure (A–D) are calculated by measuring complex pressures (p1–p2) as follows:

$$A = \frac{-i}{2} x \frac{p_1 - p_2 e^{-ik\sigma x_1}}{\sin k\sigma x_1} e^{-ik\sigma x_2}; \quad (1)$$

$$B = \frac{i}{2} x \frac{p_1 - p_2 e^{ik\sigma x_1}}{\sin k\sigma x_1} e^{ik\sigma x_2}; \quad (1a)$$

$$C = \frac{i}{2} x \frac{p_4 - p_3 e^{-k\sigma x_4}}{\sin k\sigma x_4} e^{ik\sigma x_3}; \quad (1b)$$

Table 1. Properties of fabric construction.

Fabric Code	Course (cm)	Wale (cm)	Area Density (g/m^2)	Fabric Thickness (mm)	Connecting Yarn per Course	Connecting Yarn Angle
SF-A	5	4	1159	6,24	1:6	10
SF-B	6	4	865	5,50	1:2	15
SF-C	6	4	998	5,40	1:4	15
SF-D	5	4	1040	5,77	1:2	45
SF-E	6	4	830	5,31	1:2	10

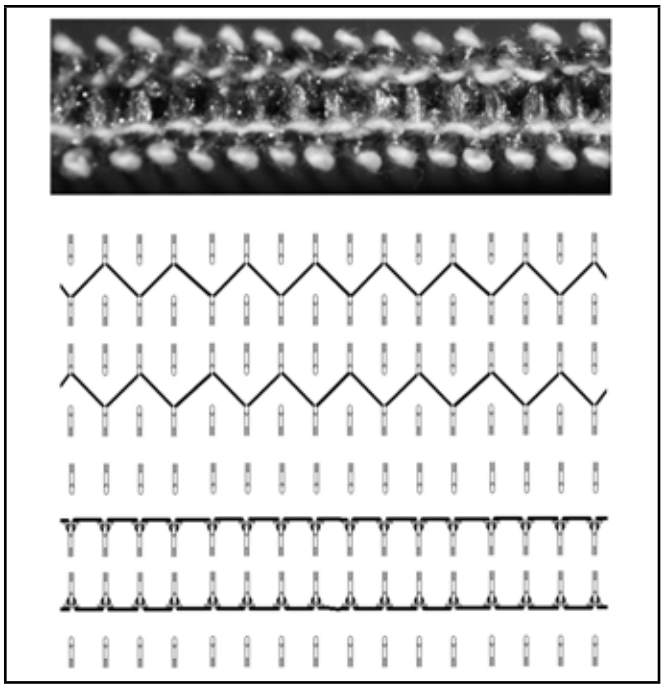

Figure 5. Technical drawings and photographs of sample fabric knits (SF-D).

$$D = \frac{-i}{2} x \frac{p_4 - p_2 e^{ik\sigma x_4}}{\sin k\sigma x_4} e^{-ik\sigma x_3}; \tag{1c}$$

Where,

$$\sigma x_1 = |x_1 - x_2|; \tag{2}$$

$$\sigma x_2 = |x_2|; \tag{2a}$$

$$\sigma x_3 = x_3; \tag{2b}$$

$$\sigma x_4 = x_4 - x_3. \tag{2c}$$

The transfer matrix is defined as the matrix that relates the above complex amplitudes of the sound pressures. Therefore,

$$\begin{Bmatrix} A \\ B \end{Bmatrix} = \begin{bmatrix} \alpha & \beta \\ \gamma & \sigma \end{bmatrix} \begin{Bmatrix} C \\ D \end{Bmatrix}. \tag{3}$$

The TL value is in fact:

$$TL = 20 \log |\alpha|. \tag{4}$$

There are two different techniques to obtain α from the measured sound pressures and then determining the TL values: the anechoic termination method and the two-load.[2–6] In this paper, a method is introduced, which combines the above techniques: the close rigid termination, and the sound absorbing termination (a thick piece of rock wool against a rigid wall) (Fig. 4). The TL value is calculated using:

$$TL = 20 \log \left| \frac{A_a D_b - A b D_a}{C_a D_b - C_b D_a} \right|; \tag{5}$$

The subscripts a and b here denote the close rigid and absorbing termination, respectively.

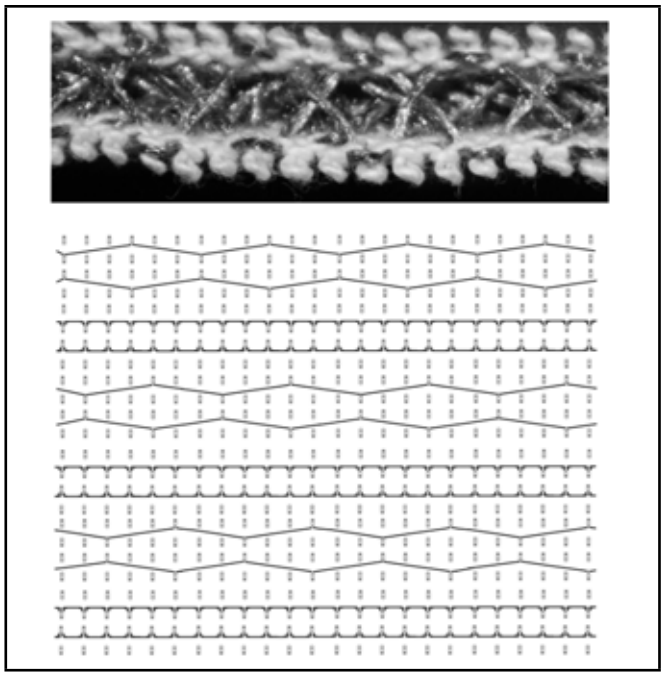

Figure 6. Technical drawings and photographs of sample fabric knits (SF-E).

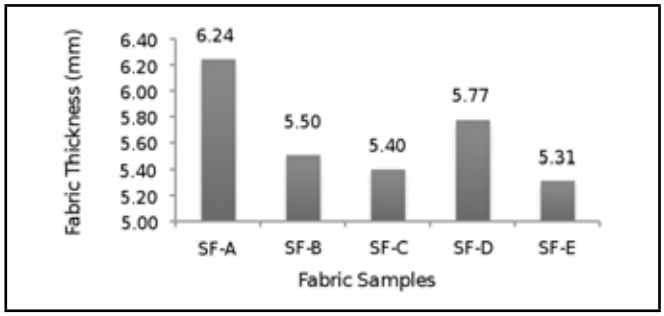

Figure 7. Thickness of fabrics.

2.3.2. Method

The material measurements are based on the two-microphone transfer-function method according to ISO 10534–2 and ASTM E1050–98 international standards, which is for the horizontal mounting of orientation-sensitive materials and the simulation of measurements on hanging ceilings, wall mountable. The testing apparatus is a part of a complete acoustic material testing system, featuring Brüel& Kjær PULSE^{TM} system (Fig. 9).[7]

2.3.3. Impedance Tube; the Two-Microphone Transfer-Function Method

A small-tube setup is used to measure the parameters for the frequency range of 50–6400 Hz. A small impedance tube kit from Brüel&Kjær Type 4206 consists of a 29 mm diameter tube (small tube) sample holder and an extension tube. A frequency-weighting unit is also provided, in which, types of weighting are selectable; high-pass for high frequency mea-

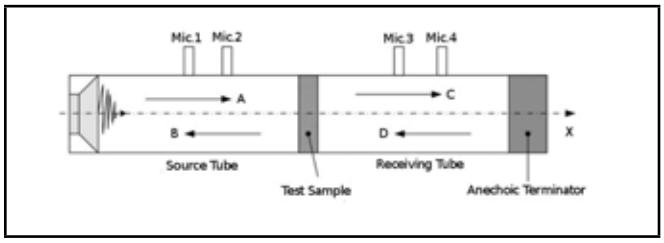

Figure 8. Schematic structure of the modified impedance tube apparatus used for the measurement of the TL values.

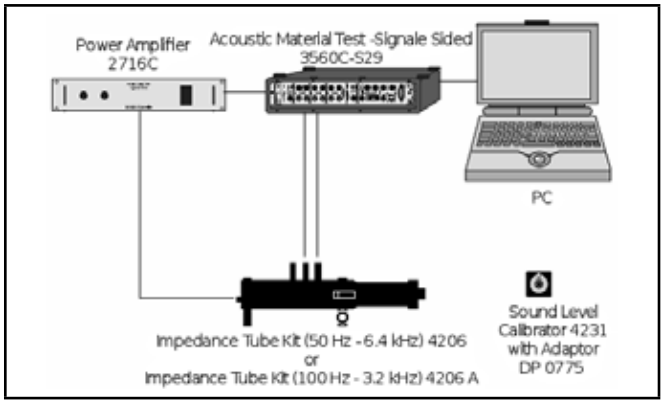

Figure 9. Test Setup.

surements in the small tube, linear for measurements in the large tube, and low-pass for extra measurement accuracy below 100 Hz. At one end of the impedance tube, a loudspeaker is mounted to act as a sound source. The testing material is placed at the other end of the tube for the testing of sound absorption properties (Fig. 10).[7]

2.3.4. Measurement Methodology and Material

A sound source is placed at one end of the impedance tube, and a sample of the material under testing is placed at the other end, mounted at a fixed distance from a rigid reflecting plate. A signal generator and an amplifier feed the loudspeaker with a broadband, stationary random noise: the sound waves propagate as plane waves in the tube, hit the sample, and are then reflected. Therefore, a standing-wave interference pattern results due to the superposition of waves travelling forward and backward inside the tube. Measuring the sound pressure at two fixed locations and calculating the complex transfer function using a two channel digital frequency analyzer, it is possible to determine the complex reflection coefficient, the sound absorption coefficient and the normal acoustic impedance of the material.[6,8] The usable frequency range depends on the diameter of the tube and the spacing between the microphone positions: with the small tube setup (diameter = 29 mm), it is possible to make measurements in the frequency range between 500 and 6400 Hz. This frequency range is fundamental

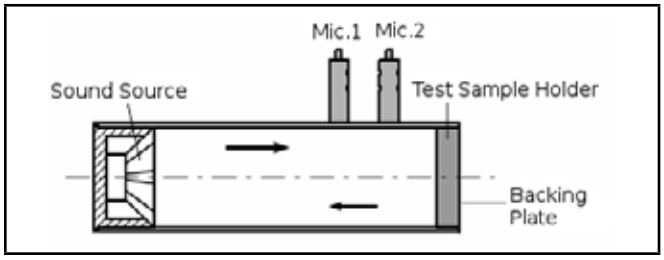

Figure 10. Impedance tube setup for the two-microphone transfer function method.

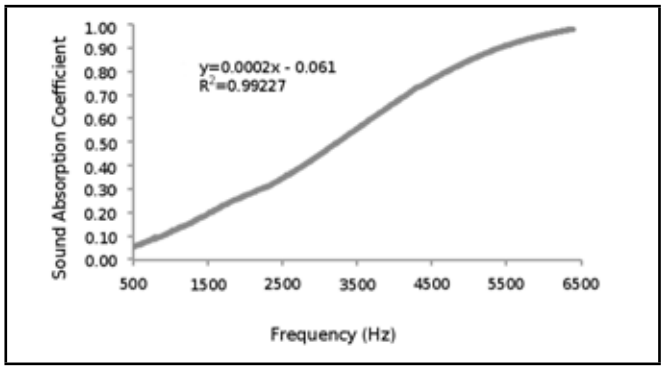

Figure 11. Acoustic absorption properties of SF-A.

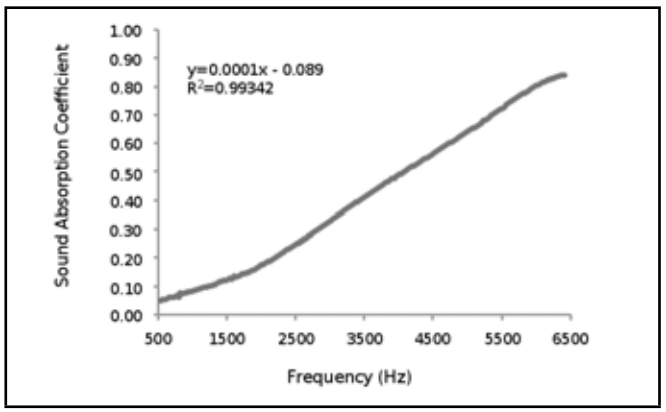

Figure 12. Acoustic absorption properties of SF-B.

with regards to traffic noise applications such as noise barriers (see for the traffic noise spectrum).[9]

3. RESULTS AND DISCUSSION

Figure 16 shows the test results related to the sound absorbance capacities of the spacer fabrics with different patterns. In the present study, the sound absorbance test was applied three times on each one of five spacer knitted structures produced with the connection types demonstrated in Fig. 1. A graphic was formed on the basis of arithmetic means of the data obtained as a result of these tests (Fig. 16). In the spacer fabric groups manufactured with all the pattern types, SF-A samples had the best sound absorbance behaviour depending on the knitting type, followed by SF-D samples. The lowest absorbance rate was detected in the SF-E sample.

When the graphic of the test results was examined, it was reported that, in all the samples, the sound absorbance coefficient increased in direct proportion to the frequency increase. In order to examine the pattern of behaviour of this increase, the separate sound absorbance graphics were drawn for all samples and Regression Analysis (R2) was made on these graphics. With the results of the Regression Analysis in Figs. 11–15, it can be seen that this increase behavior was high in all samples.

When the thickness values (Fig. 7) and the sound absorbance test results of the fabrics studied in the research were examined comparatively, a significant relationship was found between the thickness and the increase in the sound absorbance rate.

4. CONCLUSIONS

The results of this study indicate that the SF-A fabric had the highest sound absorption properties as compared to the devel-

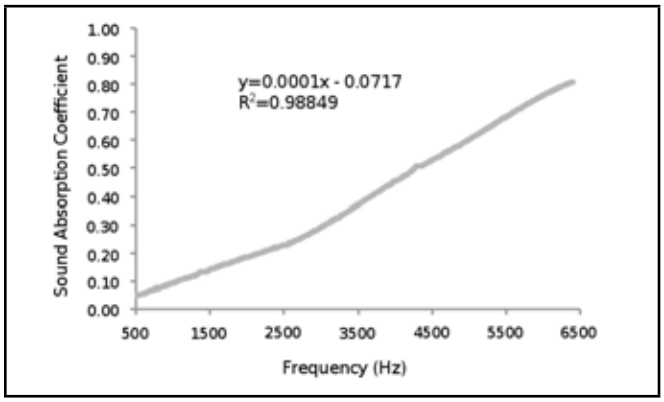

Figure 13. Acoustic absorption properties of SF-C.

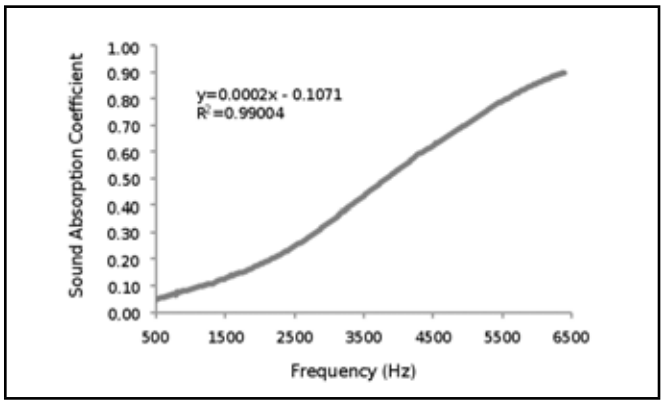

Figure 14. Acoustic absorption properties of SF-D.

oped fabrics in this study. On the other hand, it is also clearly seen that the SF-E fabric had the lowest sound absorption. Surprisingly, it was found that both SF-A and SF-E have the same technical drawings and yarn connecting angle; however, they have different fabric thicknesses. The thickness of the SF-A fabric has been found to be higher than the thickness of the SF-E fabric. A possible explanation for this is that the lower fabric thickness has caused a higher porous fabric structure, which directly affects the sound absorption properties of the fabrics. The thickness of the fabrics is related to fabric structures, the connecting yarn angle, and the yarn linear density. Another possible explanation for this is that the difference in the fabric's connecting yarn per course could also move in correlation with the yarn's linear density. These findings also suggest that when the connecting yarn angle increases, the thickness of the fabrics also increases. It can thus be suggested that the yarn connecting angle and the linear density of the yarn

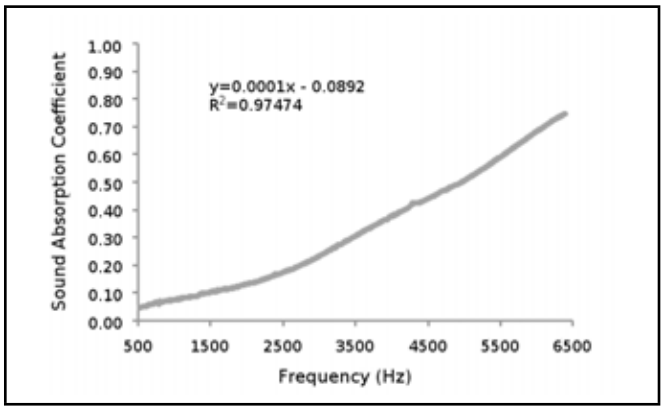

Figure 15. Acoustic absorption properties of SF-E.

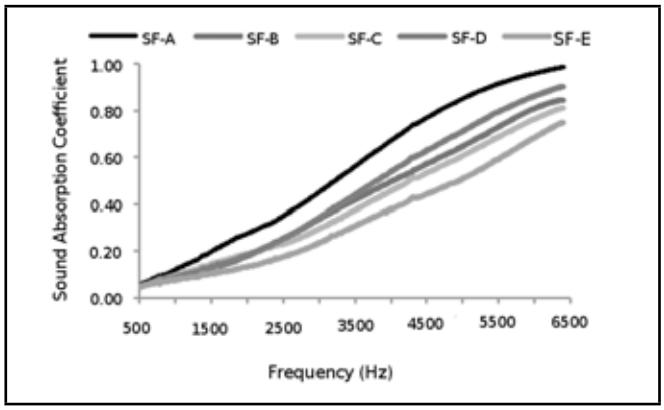

Figure 16. Acoustic absoption graphic of spacer knitted fabrics.

could be the major factors for the fabric thickness, and also a strong link may exist between the fabric thickness and the sound absorption.

The most obvious finding to emerge from this study is that a strong relationship between the thickness and the sound absorption exists. The observed increase in the sound absorption properties of the fabrics could be attributed to the increase in the fabric thickness and decrease the porous structure due to the connecting yarn angle and linear density of the yarn used. It is suggested that the association of these factors is investigated in future studies by making use of modelling software to estimate the sound absorption properties of fabrics.

REFERENCES

[1] Tao, Z. and A. F. Seybert, A review of current techniques for measuring muffler transmission loss, *in SAE 2003 Noise and Vibration Conference and Exhibition*, Grand Traverse, MI, (2003).

[2] Young, C. J. and Crocker, M. J. Prediction of transmission loss in mufflers by the finite–element method, *Journal of the Acoustical Society of America*, **57**(1), 144–148, (1975).

[3] Munjal, M. and Doige, A. Theory of a two source-location method for direct experimental evaluation of the four-pole parameters of an aeroacoustic element, *Journal of Sound and Vibration*, **141**(2), 323–333, (1990).

[4] Song, B. H. and Bolton, J. S. A transfer-matrix approach for estimating the characteristic impedance and wave numbers of limp and rigid porous materials, *Journal of the Acoustical Society of America*, **107**(3), 1131–1152, (2000).

[5] Song, B. H., Bolton, J. S., and Kang, Y. J. Effect of circumferential edge constraint on the acoustical properties of glass fiber materials, *Journal of the Acoustical Society of America*, **110**(6), 2902–2916, (2001).

[6] Pispola, G., Horoshenkov, K. V., and Asdrubali, F. Transmission loss measurement of consolidated granular media (L), *Journal of the Acoustical Society of America*, **117**(5), 2716–2719, (2005).

[7] Brüel & Kjær, Tube Material Test Product Data BP 103914 03/05, Denmark, (1998).

[8] Brüel & Kjær, Impedance Tube Model 4206 User Mannual.

[9] Ravindra, W., Capacitive fiber-meshed transducers for touch and proximity-sensing applications, *Sensors Journal, IEEE*, **5**(5), 989–994, (2005).

Statistical Evaluation of Complex Sound Environment with Background Noise

Akira Ikuta and Hisako Orimoto

Department of Management Information Systems, Prefectural University of Hiroshima, 1-1-71 Ujina-Higashi, Minamiku, Hiroshima 734-8558, Japan

Nazmul H. Siddique and Liam Philip Maguire

School of Computing and Intelligent Systems, University of Ulster, Northland Road, Londonderry BT48 7JL, United Kingdom

(Received 21 January 2013; revised 6 December 2013; accepted 7 May 2014)

In order to evaluate noise in a sound environment, it is necessary to estimate the sound levels at evaluation points based on the observations at a reference point. In this study, a method is derived based on the observations contaminated by a background noise to estimate system parameters reflecting several orders of correlation information between the evaluation and reference points in a complex sound environment. Furthermore, a statistical evaluation method for traffic noise under the existence of background noise is proposed. The effectiveness of the proposed method is experimentally confirmed by applying it to the traffic noise data measured in a complex sound environment.

1. INTRODUCTION

In the evaluation of a sound environment around a main line, it is necessary to estimate the sound levels at evaluation points based on the observations at a reference point from the viewpoint of establishing a monitor system for the actual complex sound environment. Furthermore, the internal physical mechanism of an actual sound environment is often difficult to recognize analytically, and it contains unknown structural characteristics. In a previous study,[1] it was found that complex sound environment systems are difficult to analyse by using usual structural methods based on the physical mechanism. Therefore, a nonlinear system model was derived in the expansion series form reflecting various types of correlation information from the lower order to the higher order between input and output variables.[1] The conditional probability density function contains the linear and nonlinear correlations in the expansion coefficients, and these correlations play an important role as the statistical information for the input and output relationships of sound environment systems.

On the other hand, the random noise in an actual sound environment usually exhibits multifarious and complex characteristics such as non-Gaussian distribution and non-linear and non-stationary properties relating to natural, social, and/or human factors. Furthermore, the observation data are usually contaminated by background noise with complex statistical properties. In this situation, in order to evaluate the sound environment, precise estimation of the system characteristics of the sound environment is required, considering the contaminated observed data.

In this study, a general type of complex sound environment is considered. An estimation method for the sound levels at evaluation points for the complex sound environment around a main line such as a highway and a railroad is proposed on the basis of the observations at a reference point under the existence of background noise. By adopting an expansion expression of the conditional probability distribution as the system characteristics, a method to estimate the system parameters reflecting several orders of correlation information between the evaluation and reference points is first derived. Furthermore, a prediction method for the probability distribution of traffic noise at the evaluation points is also considered.

The effectiveness of the proposed theory is experimentally confirmed by applying it to actual data of road-traffic noise measured around a national road in the city of Hiroshima and low-frequency noise observed in a complicated sound environment near the exit of a tunnel, which is generated by Shinkansen trains running through the tunnel.

2. EVALUATION OF TRAFFIC NOISE UNDER THE EXISTENCE OF BACKGROUND NOISE

2.1. Statistical Model for Sound Environment around a Main Line

In the evaluation of traffic noise in a sound environment around a main line such as a highway and a railroad, it is necessary to estimate the sound levels at multiple evaluation points based on the observation at a reference point because of the difficulties of monitoring the sound levels at all evaluation points and at every instantaneous time. Furthermore, in the measurement of the sound environment, the observation data are generally contaminated by background noise.

The intensity variables satisfying the additive property of the specific noise and the background noise are considered in this section. Let x and y be the sound intensities of a specific noise at an evaluation point and a reference point, respectively. The probability distribution of x has to be predicted on the basis of the observed data of y. Though the single evaluation point is considered, theoretically, for the simplification of the mathematical expression, the extension of the theory to the case of the multi-evaluation points is easy by considering multi-dimensional variable $\mathbf{x}$ instead of the single variable x.

All the information on linear and/or nonlinear correlations between x and y is included in the conditional probability density function $P(x|y)$.

In order to explicitly find the various correlation properties between x and y, let us expand the joint probability density function $P(x,y)$ into an orthogonal polynomial series, as follows:[2]

$$P(x,y) = P_0(x)P_0(y)\sum_{r=0}^{\infty}\sum_{s=0}^{\infty} A_{rs}\phi_r^{(1)}(x)\phi_s^{(2)}(y); \quad (1)$$

where $A_{rs} = \left\langle \phi_r^{(1)}(x)\phi_s^{(2)}(y) \right\rangle$ and $\langle\cdot\rangle$ denotes the averaging operation. $P_0(x)$ and $P_0(y)$ can be chosen arbitrarily as the probability density functions describing the dominant parts of the actual fluctuation pattern. Two functions $\phi_r^{(1)}(x)$ and $\phi_s^{(2)}(y)$ are orthogonal polynomials with the weighting functions $P_0(x)$ and $P_0(y)$. The information on the various types of linear and/or nonlinear correlations between x and y is reflected hierarchically in each expansion coefficient A_{rs}. In this section, the gamma distribution suitable for the random variables fluctuating within only the positive region such as the sound intensity is adopted.

$$P_0(x) = \frac{x^{m_x-1}}{\Gamma(m_x)s_x^{m_x}}e^{-\frac{x}{s_x}};$$
$$m_x = \frac{\mu_x^2}{\sigma_x^2}; s_x = \frac{\sigma_x^2}{\mu_x}; \mu_x = \langle x\rangle; \sigma_x^2 = \left\langle (x-\mu_x)^2\right\rangle; \quad (2)$$

$$P_0(y) = \frac{y^{m_y-1}}{\Gamma(m_y)s_y^{m_y}}e^{-\frac{y}{s_y}};$$
$$m_y = \frac{\mu_y^2}{\sigma_y^2}; s_y = \frac{\sigma_y^2}{\mu_y}; \mu_y = \langle y\rangle; \sigma_y^2 = \left\langle (y-\mu_y)^2\right\rangle; \quad (3)$$

where $\Gamma(\bullet)$ is a gamma function. Thus, orthogonal polynomials $\phi_r^{(1)}(x)$ and $\phi_s^{(2)}(y)$ are given by the Laguerre polynomial:[2]

$$\phi_r^{(1)}(x) = \sqrt{\frac{\Gamma(m_x)r!}{\Gamma(m_x+r)}}L_r^{(m_x-1)}(\frac{x}{s_x}); \quad (4)$$

$$\phi_s^{(2)}(y) = \sqrt{\frac{\Gamma(m_y)s!}{\Gamma(m_y+s)}}L_s^{(m_y-1)}(\frac{y}{s_y});$$
$$\left(L_n^{(\alpha)}(x) = \frac{e^x x^{-\alpha}}{n!}\frac{d^n}{dx^n}(e^{-x}x^{n+\alpha})\right). \quad (5)$$

By substituting Eq. (1) into the definition of the conditional probability, $P(x|y)$ can be expressed in an expansion series form as follows:

$$P(x|y) = \frac{P(x,y)}{P(y)} = \frac{P_0(x)\sum_{r=0}^{\infty}\sum_{s=0}^{\infty}A_{rs}\phi_r^{(1)}(x)\phi_s^{(2)}(y)}{\sum_{s=0}^{\infty}A_{0s}\phi_s^{(2)}(y)}; \quad (6)$$

2.2. Countermeasure for Background Noise in the Sound Environment

In the measurement of the sound environment, effects of the background noise are inevitable. Then, based on the additive property of the intensity variable, the observed sound intensity z_k at a discrete time k is expressed as

$$z_k = x_k + v_k; \quad (7)$$

where x_k and v_k are sound intensities of the specific noise and background noise at an evaluation point. We assume that the statistics of the background noise are known. In this section, an estimation method for the expansion coefficients A_{rs} in Eq. (1), reflecting the correlation information between x and y, is derived on the basis of the observed data z_k. Considering the expansion coefficients A_{rs} as unknown parameter vector $\mathbf{a}$:

$$\mathbf{a} = (a_1, a_2, a_3, ...)(= (\mathbf{a}_{(1)}, \mathbf{a}_{(2)}, ...);$$
$$\mathbf{a}_{(r)} = (A_{r1}, A_{r2}, ...); (r = 1, 2, ...); \quad (8)$$

the simple dynamical model

$$\mathbf{a}_{k+1} = \mathbf{a}_k; (\mathbf{a}_k = (a_{1,k}, a_{2,k}, a_{3,k}, ...) = (\mathbf{a}_{(1),k}, \mathbf{a}_{(2),k}, ...)); \quad (9)$$

is naturally introduced for the successive estimation of the parameter.

In order to derive the estimation algorithm of the parameter, attention is focused on Bayes' theorem for the conditional probability distribution:

$$P(\mathbf{a}_k|Z_k) = \frac{P(\mathbf{a}_k, z_k|Z_{k-1})}{P(z_k|Z_{k-1})}; \quad (10)$$

where $Z_k \equiv \{z_1, z_2, \cdots, z_k\}$ is a set of observation data up to time k. Based on Eq. (10), using a similar calculation process to the previously reported paper,[3] the estimate for an arbitrary polynomial function $f_{\mathbf{M}}(\mathbf{a}_k)$ of $\mathbf{a}_k$ with $\mathbf{M}$-th order can be derived as follows (cf. Appendix):

$$\hat{f}_{\mathbf{M}}(\mathbf{a}_k) = \langle f_{\mathbf{M}}(\mathbf{a}_k)|Z_k\rangle = \frac{\sum_{\mathbf{m}=\mathbf{0}}^{\mathbf{M}}\sum_{n=0}^{\infty}B_{\mathbf{m}n}C_{\mathbf{M}\mathbf{m}}\theta_n^{(2)}(z_k)}{\sum_{n=0}^{\infty}B_{\mathbf{0}n}\theta_n^{(2)}(z_k)}; \quad (11)$$

with

$$B_{\mathbf{m}n} = \left\langle \theta_{\mathbf{m}}^{(1)}(\mathbf{a}_k)\theta_n^{(2)}(z_k)|Z_{k-1}\right\rangle; (\mathbf{m} = (m_1, m_2, ...)). \quad (12)$$

Two functions, $\theta_{\mathbf{m}}^{(1)}(\mathbf{a}_k)$ and $\theta_n^{(2)}(z_k)$, are orthonormal polynomials with the weighting functions $P_0(\mathbf{a}_k|Z_{k-1})$ and $P_0(z_k|Z_{k-1})$. Furthermore, $C_{\mathbf{M}\mathbf{m}}$ is the coefficient when the function $f_{\mathbf{M}}(\mathbf{a}_k)$ is expanded as:

$$f_{\mathbf{M}}(\mathbf{a}_k) = \sum_{\mathbf{m}=\mathbf{0}}^{\mathbf{M}} C_{\mathbf{M}\mathbf{m}}\theta_{\mathbf{m}}^{(1)}(\mathbf{a}_k) \quad (13)$$

As the concrete expression on the fundamental probability function for the parameter $\mathbf{a}_k$ fluctuating in both a positive and negative range, a standard Gaussian distribution is adopted. Furthermore, a gamma distribution is adopted as the probability function for the sound intensity $\mathbf{z}_k$:

$$P_0(\mathbf{a}_k|Z_{k-1}) = \prod_i \frac{1}{\sqrt{2\pi\Gamma_{i,k}}}e^{-\frac{(a_{i,k}-a_{i,k}^*)^2}{2\Gamma_{i,k}}}; \quad (14)$$

$$P_0(z_k|Z_{k-1}) = \frac{z_k^{m_k^*-1}}{\Gamma(m_k^*)s_k^*}e^{-\frac{z_k}{s_k^*}}; \quad (15)$$

with

$$\begin{aligned} a_{i,k}^* &= \langle a_{i,k}|Z_{k-1}\rangle; \\ \Gamma_{i,k} &= \left\langle (a_{i,k}-a_{i,k}^*)^2|Z_{k-1}\right\rangle; \\ m_k^* &= z_k^{*2}/\Omega_k; s_k^* = \Omega_k/z_k^*; \\ z_k^* &= \langle z_k|Z_{k-1}\rangle; \Omega_k = \left\langle (z_k-z_k^*)^2|Z_{k-1}\right\rangle. \end{aligned} \quad (16)$$

Therefore, the orthogonal polynomials[2,4] with the weighting functions of Eqs. (14) and (15) are expressed as follows:

$$\theta_{\mathbf{m}}^{(1)}(\mathbf{a}_k) = \prod_i \frac{1}{\sqrt{m_i!}}H_{m_i}\left(\frac{a_{i,k}-a_{i,k}^*}{\sqrt{\Gamma_{i,k}}}\right); \quad (17)$$

$$\theta_n^{(2)}(z_k) = \sqrt{\frac{\Gamma(m_k^*)n!}{\Gamma(m_k^*+n)}}L_n^{(m_k^*-1)}\left(\frac{z_k}{s_k^*}\right). \quad (18)$$

By considering Eq. (7) and independence of x_k and v_k, two parameters z_k^* and Ω_k in Eq. (16) can be given by

$$z_k^* = \langle x_k|Z_{k-1}\rangle + \langle v_k\rangle; \quad (19)$$

$$\Omega_k = \left\langle (x_k-x_k^*)^2|Z_{k-1}\right\rangle + \left\langle (v_k-\langle v_k\rangle)^2\right\rangle. \quad (20)$$

Considering Eq. (6) and the property of conditional expectation, the right sides of the above equations are expressed as follows:

$$\begin{aligned} \langle x_k|Z_{k-1}\rangle &= \langle\langle x_k|y_k, Z_{k-1}\rangle|Z_{k-1}\rangle \\ &= \left\langle \int x_k P(x_k|y_k)dx_k|Z_{k-1}\right\rangle \\ &= \frac{\sum_{r=0}^{1} e_{1r}\mathbf{A}_{(r),k}\Phi(y_k)}{\sum_{s=0}^{\infty} A_{0s}\phi_s^{(2)}(y_k)}; \end{aligned} \quad (21)$$

$$\begin{aligned} &\left\langle (x_k-x_k^*)^2|Z_{k-1}\right\rangle \\ &= \left\langle \int (x_k-x_k^*)^2 P(x_k|y_k)dx_k|Z_{k-1}\right\rangle \\ &= \frac{\sum_{r=0}^{2} e_{2r}\mathbf{A}_{(r),k}\Phi(y_k)}{\sum_{s=0}^{\infty} A_{0s}\phi_s^{(2)}(y_k)}; \end{aligned} \quad (22)$$

with

$$\begin{aligned} \Phi(y_k) &= (\phi_0^{(2)}(y_k),\phi_1^{(2)}(y_k),...)^t; \\ \mathbf{A}_{(r),k} &= (A_{r0}, \mathbf{a}_{(r),k}^*)(r=1,2,...); \\ \mathbf{A}_{(0),k} &= \mathbf{A}_{(0)} = (A_{00}, A_{01}, A_{02}, ...); \\ \mathbf{a}_{(r),k}^* &= \left\langle \mathbf{a}_{(r),k}|Z_{k-1}\right\rangle; \end{aligned} \quad (23)$$

where t denotes the transpose of a matrix. The coefficients e_{1r} and e_{2r} in Eqs. (21) and (22) are determined in advance by expanding x_k and $(x_k-x_k^*)^2$ in the following orthogonal series forms:

$$x_k = \sum_{r=0}^{1} e_{1r}\phi_r^{(1)}(x_k); (x_k-x_k^*)^2 = \sum_{r=0}^{2} e_{2r}\phi_r^{(1)}(x_k) \quad (24)$$

Furthermore, using the definition of the Laguerre polynomial and Eqs. (6) and (7), the expansion coefficient $B_{\mathbf{m}n}$ can be calculated as in Eq. (25) (see the top of the next page), where e_{r2r} is the expansion coefficient in the following expansion series:

$$x_k^{r_2} = \sum_{r=0}^{r_2} e_{r_2 r}\phi_r^{(1)}(x_k). \quad (26)$$

From Eqs. (19)–(22) and (25), it can be found that the parameters z_k^*, Ω_k and the expansion coefficient $B_{\mathbf{m}n}$ are given by the predictions of the unknown parameter $\mathbf{a}_k$, the statistics of the background noise v_k, and the observations y_k at the reference point. By considering Eq. (9), the predictions to perform the recurrence estimation can be given for an arbitrary polynomial function $g_{\mathbf{N}}(\mathbf{a}_{k+1})$, with $\mathbf{N}$ th order of $\mathbf{a}_{k+1}$, can be expressed as:

$$\begin{aligned} g_{\mathrm{N}}^*(\mathbf{a}_{k+1}) &= \langle g_{\mathbf{N}}(\mathbf{a}_{k+1})|Z_k\rangle \\ &= \langle g_{\mathbf{N}}(\mathbf{a}_k)|Z_k\rangle = \hat{g}_{\mathbf{N}}(\mathbf{a}_k). \end{aligned} \quad (27)$$

2.3. Prediction of Specific Noise at the Evaluation Point

Because the conditional probability density function $P(x|y)$ can be considered as an invariant system characteristic, reflecting mainly the proper correlation relationship between the two sound intensities y and x at the reference and evaluation points, the probability distribution $P_s(x)$ of the sound intensity at the evaluation point corresponding to the random noise observed at the reference point can be predicted, as: $P_s(x) = \langle P(x|y)\rangle_y$. Thus, based on Eq. (6) and using the estimated parameter $\hat{\mathbf{a}}_k = \left(\hat{A}_{11}, \hat{A}_{12}, \cdots\right)$, the probability density function $P_s(x)$ at the evaluation point can be predicted from the observed data y at the reference point, as follows:

$$P_s(x) = P_0(x)\sum_{r=0}^{\infty}\left\langle \frac{\sum_{s=0}^{\infty}\hat{A}_{rs}\phi_s^{(2)}(y)}{\sum_{s=0}^{\infty}A_{0s}\phi_s^{(2)}(y)}\right\rangle_y \phi_r^{(1)}(x). \quad (28)$$

3. APPLICATION TO TRAFFIC NOISE IN AN ACTUAL SOUND ENVIRONMENT

The effectiveness of the proposed theory in Section 2 is confirmed experimentally by applying it to the actual data of road-traffic noise and low-frequency noise observed in a complicated sound environment near a national road and the entrance of a tunnel.

In order to evaluate the sound environment around the main line such as a highway and a railroad, the sound level at an evaluation point has to be estimated on the basis of the observation at a reference point. For the road-traffic noise, the reference point and the evaluation point were chosen at the positions being 1 m and 20 m apart from one side of the road as shown in Fig. 1. Since there are fences, a river, and buildings between the reference point and the evaluation point, the surrounding environment shows very complex characteristics, and it is difficult to identify the sound propagation characteristics based on the physical mechanism. By applying the proposed method, the probability density function of the sound level at the evaluation point was predicted on the basis of the observation at the reference point. Road-traffic noise was measured

$$B_{\mathbf{m}n} = \sqrt{\frac{\Gamma(m_k^*)n!}{\Gamma(m_k^*+n)}} \sum_{r_1=0}^{n} (-1)^{r_1} \left(\begin{array}{c} n \\ r_1 \end{array} \right) \frac{1}{n!} \frac{\Gamma(m_k^*+n)}{\Gamma(m_k^*+r_1)} \frac{1}{s_k^*}$$
$$\cdot \sum_{r_2=0}^{r_1} \sum_{r=0}^{r_2} \frac{e_{r_2 r} \left\langle \theta_{\mathbf{m}}^{(1)}(\mathbf{a}_k)(A_{r0}, \mathbf{a}_{(r),k}) | Z_{k-1} \right\rangle \Phi(y_k)}{\sum_{s=0}^{\infty} A_{0s} \phi_s^{(2)}(y_k)} \left\langle v_k^{r_1-r_2} \right\rangle ; \quad (25)$$

Table 1. Statistics of the specific noise and the background noise.

Specific Noise		Background Noise	
Mean [watt/m^2]	Standard Deviation [watt/m^2]	Mean [watt/m^2]	Standard Deviation [watt/m^2]
1.7185×10^{-6}	2.0567×10^{-6}	1.7185×10^{-6}	6.734×10^{-8}

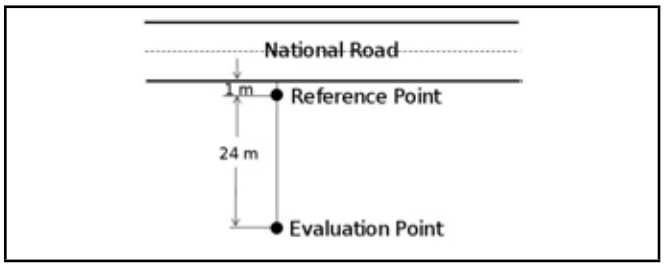

Figure 1. A schematic drawing of the experiment in a road traffic noise environment near a national road.

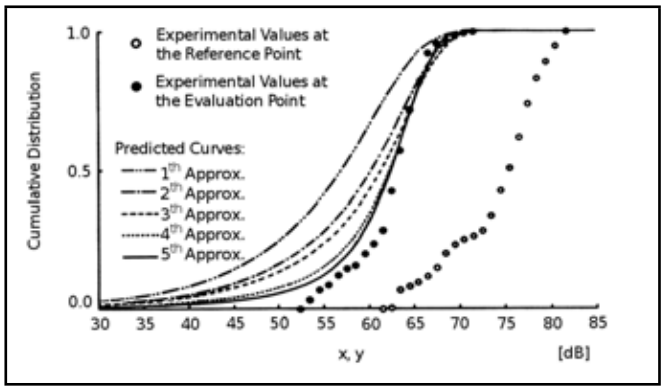

Figure 2. A comparison between predicted curves and experimental values of the probability distribution at the evaluation point for road-traffic noise.

at every 0.2 s using a sound-level meter (model NL-06 integral standard type, Rion Co.) under an A-characteristic and FAST response with a time constant of 0.125 s in an RMS circuit. Applying the proposed algorithm developed in Section 2 on the 400 data sample, the expansion coefficients in Eq. (1) were estimated. The statistics of the road-traffic noise and the background noise are shown in Table 1. In order to confirm the effectiveness of the proposed method, it is necessary to apply it to the data with the large amplitude of the background noise. Therefore, after separately recording the specific noise and background noise into a data recorder, by replaying the recorded two noises and mixing them in an anechoic chamber, the observation data were measured. Then, we adjusted the amplitude of background noise so as to have the same mean value as the specific noise.

Using Eq. (28) and the estimated expansion coefficients, the probability distribution at the evaluation point was predicted from the observation at the reference point. The 300 sampled data following the data used for the estimation of the expansion coefficients were adopted for predicting the probability distribution of the sound level at the evaluation point. For the purpose of confirming the prediction accuracy of the proposed method, it was only applied to the data during a short time interval as a trial. In the real assessment for the noise environment, the proposed method has to be applied to the data in appropriate time intervals, according to the purpose of real noise evaluation. Figure 2 shows the comparison between the theoretically predicted curves and the experimentally sampled points on the probability distribution. The cumulative distributions of sound level related to noise evaluation quantities L_x ($(100 - x)$ percentile level) are shown. In the evaluation of the noise environment, the prediction of the cumulative distribution connected with the noise evaluation index L_x is important.[5] The "1st Approx." considers only the first term in Eq. (28), and the predicted curves from the "2nd Approx." to the "5th Approx." consider the estimated expansion coefficients $\hat{A}_{11}$, $\hat{A}_{12}$, $\hat{A}_{21}$, and $\hat{A}_{22}$, additionally. It can be observed that the theoretically predicted curves approach the experimental values when expansion coefficients of several higher orders are considered. Several noise evaluation quantities L_x evaluated from Fig. 2 are shown in Table 2. It is obvious that the proposed method provides accurate predictions within ± 1 dB permissible errors in the measurement of environmental noises, and the effectiveness of the proposed method has been confirmed numerically.

Table 2. Comparison between the experimental values and theoretically predicted values for several noise evaluation quantities in dB evaluated from Fig. 2.

Noise Evaluation Quantities	L_5	L_{10}	L_{50}	L_{90}	L_{95}
Experimental Values	67.3	66.1	62.9	55.6	53.6
Predicted Curve (1st Approx.)	66.2	64.7	56.7	41.7	35.5
Predicted Curve (2nd Approx.)	68.2	66.7	60.0	45.5	40.0
Predicted Curve (3rd Approx.)	68.6	67.3	61.1	47.3	41.1
Predicted Curve (4th Approx.)	67.9	66.7	62.1	52.0	46.4
Predicted Curve (5th Approx.)	67.6	66.7	62.3	53.9	49.8

For the low-frequency noise generated by the Shinkansen trains running through the tunnel, a reference point and an evaluation point were chosen at the positions that were 10 m and 25 m apart from the entrance of the tunnel as shown in Fig. 3. By applying the proposed method in Section 2, the probability density function of the low-frequency noise at the evaluation point was predicted. Four kinds of low-frequency noise data was generated from the Shinkansen trains: 1) Up "Hikari", 2) Down "Hikari", 3) Up "Nozomi", and 4) Down "Nozomi" were measured by using a ceramic microphone with a low-frequency sound pressure level meter (model NA18A, Rion Co.) under a FLAT-characteristic (i.e., a flat frequency

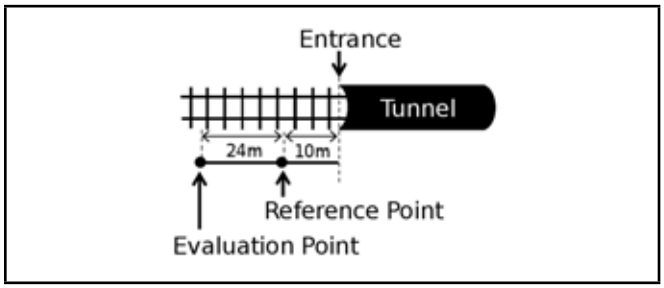

Figure 3. A schematic drawing of the experiment in low-frequency noise near an entrance of a tunnel.

Table 3. Statistics of the specific noise.

Train	Mean [watt/m^2]	Standard Deviation [watt/m^2]
Up "Hikari"	2.5295×10^{-5}	3.3607×10^{-5}
Down "Hikari"	3.0542×10^{-5}	4.6687×10^{-5}
Up "Nozomi"	3.3074×10^{-5}	6.8644×10^{-5}
Down "Hikari"	4.5607×10^{-5}	9.7969×10^{-5}

characteristic within the range of 1 Hz to 100 Hz) at every 0.1 s. In the measurement of low-frequency noise, the effects of a wind noise are inevitable.[6–8] Therefore, by applying the proposed estimation algorithm in Eq. (11) to the observation data for the Up "Hikari" train affected by a wind noise, the expansion coefficients in Eq. (1) were first estimated. The statistics of the low-frequency noise and the background noise are shown in Tables 3 and 4, respectively. Based on the estimates of the expansion coefficients, the probability distributions for the sound level of the low-frequency noises generated from the i) Down "Hikari", ii) Up "Nozomi" and iii) Down "Nozomi" trains were predicted by measuring the sound-level data at the reference point and using Eq. (28). Figures 4, 5 and 6 show comparisons between the theoretically predicted curves and experimental values for the probability distributions at the evaluation point for the Down "Hikari" train, Up "Nozomi" train, and Down "Nozomi" train, respectively. The cumulative distributions of the sound level are shown in these figures. When cboxa sufficient number of expansion coefficients of higher order are taken into consideration, the theoretically predicted curves approach the experimentally sampled values for the probability distribution of the low-frequency noise.

Furthermore, in order to discuss the precision of the proposed prediction method of the probability distribution, comparisons between the theoretically predicted values and the experimental values for noise evaluation quantities L_x (x =5, 10, 50, 90, 95) obtained from Figs. 4, 5 and 6 are shown in Tables 5, 6 and 7. In an evaluation for low-frequency noise with the fluctuation, L_5, and L_{10} correspond approximately to the peak or maximum values of the fluctuation, and L_{50} corresponds to the median. Furthermore, L_{90} and L_{95} correspond to the background noise levels. From these results, the effectiveness of the proposed prediction method for the probability distribution at evaluation points has been confirmed numerically.

4. CONCLUSION

In this paper, an evaluation method of traffic noise in a complex sound environment under the existence of a background noise has been proposed. More specifically, a prediction method of the sound level at evaluation points based on the observations at a reference point has been theoretically derived. By paying attention to the intensity variables satisfying the additive property of the specific noise and the background noise, a method predicting the probability distribution of the sound intensity at evaluation points has been proposed. The proposed prediction method has been realized by introducing a sound environment model of the conditional probability type. The proposed method has then been applied to the estimation and prediction of actual road-traffic noise and low-frequency noise, and it has been experimentally verified that good results have been achieved with this method.

Table 4. Statistics of the wind noise.

Mean [watt/m^2]	Standard Deviation [watt/m^2]
1.2629×10^{-5}	4.5943×10^{-5}

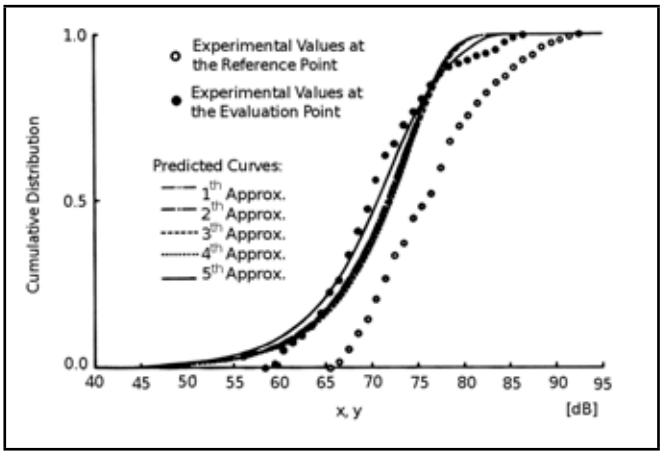

Figure 4. A comparison between predicted curves and experimental values of the probability distribution at the evaluation point for a low-frequency noise by Down "Hikari".

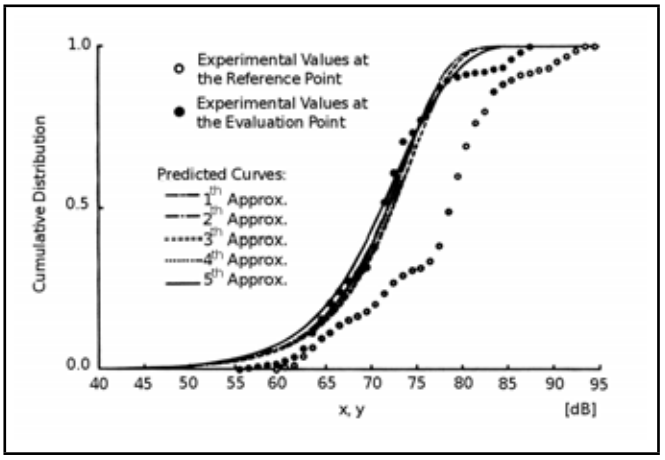

Figure 5. A comparison between predicted curves and experimental values of the probability distribution at the evaluation point for a low-frequency noise by Up "Nozomi".

Table 5. Comparison between the experimental values and theoretically predicted values for several noise evaluation quantities in dB evaluated from Fig. 4.

Noise Evaluation Quantities	L_5	L_{10}	L_{50}	L_{90}	L_{95}
Experimental Values	82.9	78.5	70.0	62.6	60.5
Predicted Curve (1st Approx.)	78.9	78.0	72.3	62.3	58.6
Predicted Curve (2nd Approx.)	79.1	77.7	72.1	62.1	58.4
Predicted Curve (3rd Approx.)	78.9	77.6	71.8	61.8	58.2
Predicted Curve (4th Approx.)	78.6	77.4	71.7	61.7	57.7
Predicted Curve (5th Approx.)	80.2	78.2	70.7	60.6	57.0

$$\hat{f}_{\mathbf{M}}(\mathbf{a}_k) = \int\int\ldots\int f_{\mathbf{M}}(\mathbf{a}_k)P(\mathbf{a}_k|Z_k)d\mathbf{a}_k = \frac{\int\int\ldots\int \sum_{\mathbf{m'}=\mathbf{0}}^{\mathbf{M}} C_{\mathbf{Mm'}}\theta^{(1)}_{\mathbf{m'}}(\mathbf{a}_k)P_0(\mathbf{a}_k|Z_{k-1}) \sum_{\mathbf{m}=\mathbf{0}}^{\infty}\sum_{n=0}^{\infty} B_{\mathbf{m}n}\theta^{(1)}_{\mathbf{m}}(\mathbf{a}_k)\theta^{(2)}_n(z_k)d\mathbf{a}_k}{\sum_{n=0}^{\infty} B_{\mathbf{0}n}\theta^{(2)}_n(z_k)}. \tag{A3}$$

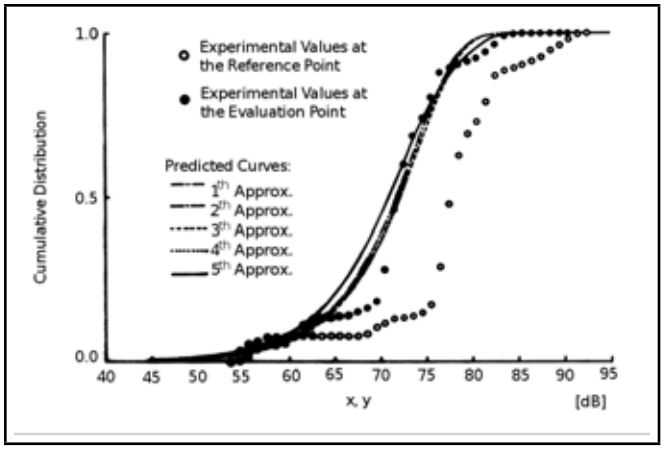

Figure 6. A comparison between predicted curves and experimental values of the probability distribution at the evaluation point for a low-frequency noise by Down "Nozomi".

Table 6. Comparison between the experimental values and theoretically predicted values for several noise evaluation quantities in dB evaluated from Fig. 5.

Noise Evaluation Quantities	L_5	L_{10}	L_{50}	L_{90}	L_{95}
Experimental Values	85.3	88.9	71.4	63.2	62.0
Predicted Curve (1st Approx.)	79.7	78.3	72.4	62.9	58.7
Predicted Curve (2nd Approx.)	79.7	78.3	72.3	62.6	58.7
Predicted Curve (3rd Approx.)	78.7	77.7	71.8	62.1	58.6
Predicted Curve (4th Approx.)	78.9	77.7	71.7	62.1	58.0
Predicted Curve (5th Approx.)	80.6	88.8	71.2	61.2	57.1

ACKNOWLEDGMENTS

The authors would like to thank Emeritus Professor M. Ohta for his valuable discussion and assistance during this study.

REFERENCES

[1] Ohta, M., and Ikuta, A. An acoustic signal processing for generalized regression analysis with reduced information loss based on data observed with amplitude limitation, *Acustica*, **81**, 129–135, (1995).

[2] Ohta, M., and Koizumi, T. General treatment of the response of a non-linear rectifying device to a stationary random input, *IEEE Trans. Inf. Theory*, **IT-14**, 595–598, (1968).

[3] Ohta, M., and Yamada, H. New methodological trials of dynamical state estimation for the noise and vibration environmental system–Establishment of general theory and its application to urban problems, *Acustica*, **55**, 199–212, (1984).

[4] Ohta, M., Ikuta, A., and Takaki, N. An evaluation method for an arbitrary probability distribution with digital level observation in sound and vibration systems, *Acustica*, **67**, 73–85, (1988).

[5] Mitani, Y., and Ohta, M. A Calculation of L_x and L_{eq} noise evaluation indices by use of statistical information on the noise level fluctuation, and its microcomputer-aided on-line measurement, *Applied Acoustics*, **25**, 33–47, (1988).

[6] Morgan, S., and Raspet, R. Investigation of the mechanisms of low-frequency wind noise generation outdoors, *J. Acoust. Soc. Am.*, **92**, 1180–1183, (1992).

[7] Shields, F. D. Low-frequency wind noise correlation in microphone arrays, *J. Acoust. Soc. Am.*, **117**, 3489–3496 (2005).

[8] G. P van den Berg, Wind-induced noise in a screened microphone, *J. Acoust. Soc. Am.*, **119**, 824–833, (2006).

Table 7. Comparison between the experimental values and theoretically predicted values for several noise evaluation quantities in dB evaluated from Fig. 6.

Noise Evaluation Quantities	L_5	L_{10}	L_{50}	L_{90}	L_{95}
Experimental Values	81.7	78.2	71.7	60.9	58.5
Predicted Curve (1st Approx.)	79.1	77.9	72.1	62.4	58.5
Predicted Curve (2nd Approx.)	79.1	77.9	72.1	62.4	58.5
Predicted Curve (3rd Approx.)	78.8	77.6	71.7	61.8	58.5
Predicted Curve (4th Approx.)	78.8	77.6	71.7	61.8	58.5
Predicted Curve (5th Approx.)	80.2	78.2	70.8	60.9	57.0

APPENDIX. DERIVATION OF THE ESTIMATE

The conditional joint probability density function of the parameter $\mathbf{a}_k$ and the observation z_k can be generally expanded in a statistical orthogonal expansion series:

$$P(\mathbf{a}_k, z_k|Z_{k-1}) = P_0(\mathbf{a}_k|Z_{k-1})P_0(z_k|Z_{k-1}) \sum_{\mathbf{m}=\mathbf{0}}^{\infty}\sum_{n=0}^{\infty} B_{\mathbf{m}n}\theta^{(1)}_{\mathbf{m}}(\mathbf{a}_k)\theta^{(2)}_n(z_k); \tag{A1}$$

Substituting Eq. (A1) into Eq. (10), the following expression can be obtained.

$$P(\mathbf{a}_k|Z_k) = \frac{P_0(\mathbf{a}_k|Z_{k-1}) \sum_{\mathbf{m}=\mathbf{0}}^{\infty}\sum_{n=0}^{\infty} B_{\mathbf{m}n}\theta^{(1)}_{\mathbf{m}}(\mathbf{a}_k)\theta^{(2)}_n(z_k)}{\sum_{n=0}^{\infty} B_{\mathbf{0}n}\theta^{(2)}_n(z_k)}. \tag{A2}$$

By using the above equation and the relationship in Eq. (13), and taking the conditional expectation of the function $f_{\mathbf{M}}(\mathbf{a}_k)$, the estimate of $f_{\mathbf{M}}(\mathbf{a}_k)$ can be expressed as Eq. (A3). Furthermore, by using the orthonormal condition for the function $\theta^{(1)}_m(\mathbf{a}_k)$:

$$\int\int\ldots\int \theta^{(1)}_{\mathbf{m}}(\mathbf{a}_k)\theta^{(1)}_{\mathbf{m'}}(\mathbf{a}_k)P_0(\mathbf{a}_k|Z_{k-1})d\mathbf{a}_k = \delta_{\mathbf{mm'}}; \tag{A4}$$

Eq. (11) can be derived.

High Helmholtz Sound Prediction Generated by Confined Flows and Propagation within Ducts

Morteza Bayati and Mehran Tadjfar

Aerospace Engineering Department, Amirkabir University of Technology, Tehran 15875-4413, Iran

(Received 1 January 2013; revised 26 October 2013; accepted 5 March 2014)

A hybrid method for the computation of noise radiation by a confined flow is used in this study. The proposed approach is appropriate and quite powerful for high Helmholtz numbers (i.e. when the turbulence/body interaction region is acoustically non-compact). The validation of this method is checked by comparing it with the analytical results of the tailored Green's function to the spinning of two vortex filaments in an infinite 2-D duct. The method is applied to the prediction of sound in a duct obstructed by a diaphragm. The sound sources generated by the fluctuations in the flow field are computed by means of an incompressible Large Eddy Simulation (LES). These sources are fed into a 2-D acoustic propagation Boundary Element Model (BEM). The predicted total acoustic power is 1.8 dB higher than the result obtained in the literature by Direct Numerical Calculation (DNC) and extrapolated experimental data for the same pipe configuration.

NOMENCLATURE

c_0	Sound speed
ϕ	Field variable
$()_0$	Reference quantities
u_i	Velocity components
$()_L$	Flow quantity
$()'$	Fluctuation
$()_a$	Acoustic quantity
n_i	Normal vector
δ_{ij}	Kronecker delta
T_{ij}	Lighthill tensor
H_0^1	Hankel function of the first kind
$C(x)$	Solid angle
x	Source position (vector $\vec{x}$)
y	Listener position (vector $\vec{y}$)
p	Pressure
V_ε	Exclusion volume
f	Frequency
δ_e	Momentum thickness
I	Acoustic intensity
P	Acoustic power
ω	Angular frequency ($\omega = 2\pi f$)
G	Green function

1. INTRODUCTION

In many practical applications, sound is generated by the interaction of turbulent flow with solid walls. In this situation, the sound wave experiences multiple reflections before propagation to a far field. Therefore, the sound spectrum exhibits rich frequencies content consisting of broadband and tonal components. To predict the acoustics field in these situations, a general aero-acoustic framework is required. More importantly, the employed method must often avoid many simplifying assumptions about geometry, compactness, or frequency content of sound sources.

The prediction of flow-induced noise requires accounting for the physics of both unsteady flow and the sound wave, simultaneously, since both are a solution of the compressible Navier-Stokes equation. The basic difficulties for such computations are numerous disparities between energies and length-scale in the turbulent flow and the sound field. Sound waves carry only a minuscule fraction of the flow energy, and a high-order numerical scheme is required to keep the sound wave intact. These fundamental differences are exacerbated in a low Mach number flow,[1] where the radiated acoustic power is smaller than the hydrodynamic flow power by roughly $O(M^4)$. In addition, the acoustic CFL number imposes extremely small time steps on the numerical solution in order to resolve both acoustics and hydrodynamics. That is why it is commonly accepted that hybrid methods are more appropriated for low Mach number flows. An example of a two-step or hybrid method for nearly incompressible flows is Lighthill,[2] who formally separated acoustics from hydrodynamics by introducing his acoustic analogy. It was shown that the flow mechanism that produced noise could be expressed in the form of equivalent sources in a uniform medium at rest, chosen as a representation of the propagation region surrounding the listener. The idea of equivalent sources has proven to be quite powerful at low Mach numbers. Curle[3] extended the Lighthill analogy to predict the sound of turbulent-body interaction by introducing a dipole source. Ffowcs Williams and Hawkings[4] generalized previous analogies to account for moving sources and the resulting Doppler effects.

Most of the works in literature are exterior problems. In the present work, we are concerned with the noise generated by confined flows and its propagation within the ducting. The interaction of pipe flow with singularities like diaphragm, valve contractions, or pipe junctions are sources of internal noise in industrial duct networks.[5,6] The problem of aerodynamics sound generation in pipes, allowing the aeroacoustics analogy by Davies and Ffowcs Williams,[7] showed that the acoustic efficiency of turbulence within a straight infinite duct varies with frequency from a dipole-like behaviour below the cut-off fre-

quency to free-field quadrupolar efficiency as soon as a few transverse modes are cut-on. Nelson,[8] Peters,[9] and Piellard[10] have focused on the prediction of noise generated by duct geometrical discontinuities.

Low frequencies are often considered,[11] which has two advantages: firstly, the source is acoustically compact; secondly, for frequencies below the duct cut-off, the one-dimensional Green's function can be employed. However, in many engineering products that contain ducts, the spectrum of interest often extends beyond the transverse cut-off frequency, up to several KHz. Mak[12] and Han and Mak[13] formulated the sound powers produced by the interaction of multiple in-duct elements at frequencies below and above the first transverse duct mode cut-on frequency.

The configuration of the present study corresponds to experiments of Van Herp et al.,[14] and the DNC result of Gloerfelt and Lafon.[15] The general scope of this work is to develop and validate a numerical tool for aeroacoustics noise prediction above the first cut-off frequency. This method is suitable for the determination of acoustic scattering by using an incompressible flow model in order to extend the applicability of Curle's analogy for non-compact and high Helmholtz numbers $He = 2\pi f D/c_0$. Schram[16] has shown that the derivation of a BEM variant of Curle is able to predict the aeroacoustics above the first cut-off frequency and could be employed for non-compact cases. A hybrid method was introduced for acoustic computation in the entire frequency range resolved by the flow solver for compact/non-compact sources. The flow-generated sound sources are computed using an LES solver. These sources are then used as the input data for the aeroacoustic solver, which is a boundary integral equation of Curle's analogy in the frequency domain, assuming a Hankel function as the 2-D Green's function that was solved using a boundary element method introduced by Khalighi and Bodony.[17]

The paper is organized as follows: first a derivation of the BEM variant of Curle's analogy is given, and then validation studies of this method for the spinning of two vortex filaments in an infinite straight duct for non-compact high Helmholtz numbers are put forth. Finally, we demonstrate the applicability of the method to engineering problems by computing the sound of internal confined flow through a diaphragm in a duct.

2. METHODOLOGY

An acoustic analogy for the prediction of the acoustics field radiation by an unsteady flow consists of a forced wave equation:

$$\left(\nabla^2 - \frac{1}{c_0^2}\frac{\partial^2}{\partial t^2}\right)\phi(x,t) = q(x,t); \tag{1}$$

where c_0 is the sound speed, and ϕ is a field variable, which can be the pressure or the density perturbation. Subscript $(\,)_0$ denotes the reference quantities. The source q can be estimated independently by an exact recombination of the continuity and momentum equations which yield to:

$$q = -\frac{1}{c_0^2}\frac{\partial^2 T_{ij}}{\partial x_i \partial x_j}; \tag{2}$$

in which $T_{ij} = \rho u_i u_j + (p' - c_0^2\rho')\delta_{ij} - \sigma_{ij}$ defines the Lighthill tensor in terms of velocity components u_i, Reynolds stresses, non-isentropic processes, and viscous stresses σ_{ij}. If we consider duct configurations with a high enough Reynolds number for the acoustic contribution of the wall-normal dipoles to dominate over the viscous stresses and for low Mach numbers, the convection and refraction of the sound wave is negligible compared to the scattering by duct geometry.

By implementing these assumptions, the wave propagation equation is integrated in time and space and after convolution by Green's function $G(t, x|\tau, y)$, the following is defined:

$$\begin{aligned}\rho'(x,t) = &\int_{-\infty}^{t}\iiint_V \frac{\partial^2 T_{ij}}{\partial y_i \partial y_j} G\, d^3y\, d\tau - \\ &c_0^2\int_{-\infty}^{t}\iiint_V \left(\rho'\frac{\partial^2 G}{\partial y_i^2} - G\frac{\partial^2 \rho'}{\partial y_i^2}\right) d^3y\, d\tau + \\ &\int_{-\infty}^{t}\iiint_V \left(\rho'\frac{\partial^2 G}{\partial \tau^2} - G\frac{\partial^2 \rho'}{\partial \tau^2}\right) d^3y\, d\tau;\end{aligned} \tag{3}$$

which would consist of treating the turbulent field as a monopole. A more appropriate formulation is obtained by performing integration by part of the volume integral of Eq. (3) to highlight the quarupolar character of free turbulence. The third integral of Eq. (3) vanishes by virtue of causality after integration by part. This yields:

$$\begin{aligned}\rho'(x,t) = &\int_{-\infty}^{t}\iiint_V T_{ij}\frac{\partial^2 G}{\partial y_i \partial y_j}\, d^3y\, d\tau - \\ &\int_{-\infty}^{t}\iint_{\partial V}\left(c_0^2\frac{\partial \rho'}{\partial y_i}G + \left(p' - c_0^2\rho'\right)\frac{\partial G}{\partial y_i}\right) n_i\, d^2y\, d\tau - \\ &c_0^2\int_{-\infty}^{t}\iint_{\partial V}\left(\rho'\frac{\partial G}{\partial y_i} - G\frac{\partial \rho'}{\partial y_i}\right) n_i\, d^2y\, d\tau.\end{aligned} \tag{4}$$

The free-field Green's function:

$$G(x,t|y,\tau) = \frac{\delta(t - \tau - |x-y|/c_0)}{4\pi c_0^2|x-y|} \tag{5}$$

is used in Eq. (4).

A crucial step in the derivation of Curle's analogy is the cancellation of the scattering integral with the density perturbation term of the second integral in Eq. (4). This yields the classical result:

$$\begin{aligned}\rho'(x,t) = &\int_{-\infty}^{t}\iiint_V T_{ij}\frac{\partial^2 G}{\partial y_i \partial y_j}\, d^3y\, d\tau - \\ &\int_{-\infty}^{t}\iint_{\partial V} p'\frac{\partial G}{\partial y_i} n_i\, d^2y\, d\tau.\end{aligned} \tag{6}$$

The pressure of the solid boundary appears through the dipole source. The derivation of Curle's analogy assumes that the flow model used to quantify the equivalent sources accounts for compressibility effects, including acoustic scattering. This, however, is usually not the case for a low Mach number, for which incompressible flow modelling is much more

efficient and, therefore, preferred. The analogy is valid for a low Helmholtz number or for a compact case for which acoustical effects can be approximately described by an incompressible model. For high Helmholtz numbers, the incompressible flow model must be complemented by an acoustic correction to obtain a realistic sound. For an idealized case, the analytical tailored Green's function with zero normal gradients at the boundary surface can correct the acoustic sound prediction, but in most industrial applications and ranges of frequencies, the problem is not amenable to an analytical solution. For internal problems, combining Curle's analogy with the boundary element method brings the acoustical correction when using an incompressible flow model.

To do this, we start from the inhomogeneous wave propagation equation in the Fourier domain, which takes the form of the Helmholtz equation:

$$\nabla^2 \hat{p}_a + k^2 \hat{p}_a = \hat{q}; \tag{7}$$

where $k = \omega/c_0$ is the wave number, and $\hat{q} = \frac{\partial^2 \hat{T}_{ij}}{\partial x_i \partial x_j}$ is the Lighthill tensor. In what follows, the hat notation indicating the Fourier component will be dropped for the sake of readability.

Convoluting Eq. (7) with a free-field Green's function yields:

$$\iiint_{V\backslash V_\varepsilon} \left(\nabla^2 p_a G - p_a \nabla^2 G\right) d^3y = \iiint_{V\backslash V_\varepsilon} q_L G \, d^3y + \iiint_{V\backslash V_\varepsilon} p_a \delta(x-y) \, d^3y. \tag{8}$$

In Eq. (8), the appropriate Fourier domain free-field Green's function is $G = \exp(-ikr)/(4\pi r)$ for the three-dimensional, and the Hankel function of the first kind $G = \frac{i}{4} H_0^1(kr)$ for the two-dimensional simulation. At this, $r = |x-y|$ is the distance between the source point to listener position.[18] Subscript $(\,)_L$ has been added to quantities that are provided through the flow and subscript $(\,)_a$ to signify acoustic quantity.

In the derivation of Curle's analogy, the listener is defined well apart from the source field at a uniform and quiescent region. On the contrary, the resolution of the boundary integral equation is performed by collocation (i.e. by placing the listener on the source region). The singularity is excluded by removing an exclusion volume V_ε at Eq. (8). Its contribution will be evaluated by letting the exclusion volume shrink to zero. The point x is excluded from the integration volume $V\backslash V_\varepsilon$, therefore the third integral of Eq. (8) is zero.

Applying the Green theorem and integration by parts yields:

$$C(x)P_a(x) = \iiint_V T_{ij} \frac{\partial^2 G}{\partial y_i \partial y_j} \, d^3y + \iint_{\partial V} \left(-c_0^2 \frac{\partial \rho_L}{\partial n} G - \left(p_L - c_0^2 \rho_L\right) \frac{\partial G}{\partial n} \right) d^2y - C(x)\left(p_L - c_0^2 \rho_L\right) + \iint_{\partial V} \left(\frac{\partial p_a}{\partial n} G - p_a \frac{\partial G}{\partial n} \right) d^2y. \tag{9}$$

Factor $C(x)$ is the solid angle equal to 1 when x is within the volume and equal to $\frac{1}{2}$ when x lies over a smooth surface and is equal to zero elsewhere. From the compressibility effects, we have $c_0^2 \rho_L = p_a$ and Eq. (9) becomes:

$$C(x)P_L(x) = \iiint_V T_{ij} \frac{\partial^2 G}{\partial y_i \partial y_j} \, d^3y - \iint_{\partial V} p_L \frac{\partial G}{\partial n} \, d^2y. \tag{10}$$

Equation (10) is fairly similar to the classical analogy of Curle,[6] with some differences related to the change from the time domain to the frequency domain, including the factor c_0^2 due to a different Green's function in the time and frequency domains. At Eq. (6), which is the analogy of Curle, the listener is often assumed to be in a uniform and quiescent propagation region well apart from the sound production region. That is usually employed to obtain the acoustic component only while Eq. (10) yields the full-pressure fluctuation, hydrodynamic, and acoustic pressure. This results from allowing the listener to enter the source domain, unlike the Curle's analogy.

For high Helmholtz numbers, the case would be non-compact, and with low Mach numbers, the incompressible flow is preferred, and Eq. (10) yields erroneous results, as shown by Schram.[19] In a general case, the pressure is expressed as a sum of hydraulic and acoustic components:

$$p_L = p_h + p_a. \tag{11}$$

Also, the integration domain is decomposed in two parts, corresponding respectively to volume V_1 and V_2 and their boundaries ∂V_1 and ∂V_2. The domain V_1 is localized around the collection point x with dimensions acoustically compact. The solution of Eq. (10) can resolve the hydrodynamic part of pressure p_L. The domain V_2 is defined as $v\backslash V_1$. The substitution of Eq. (11) into Eq. (10) and subtracting the hydrodynamic pressure of domain V_1 yields:

$$\begin{aligned} C(x)P_a(x) &= -\iint_{\partial V_1} p_a \frac{\partial G}{\partial n} \, d^2y + \iiint_{V_2} T_{ij} \frac{\partial^2 G}{\partial y_i \partial y_j} \, d^3y - \iint_{\partial V_2} (p_h + p_a) \frac{\partial G}{\partial n} \, d^2y \\ &= -\iint_{\partial V} p_a \frac{\partial G}{\partial n} \, d^2y + \iiint_{V_2} T_{ij} \frac{\partial^2 G}{\partial y_i \partial y_j} \, d^3y - \iint_{\partial V_2} p_h \frac{\partial G}{\partial n} \, d^2y; \end{aligned} \tag{12}$$

where the boundary integrals involving the acoustic pressure p_a have been grouped together. The wall pressure is the sum of the hydrodynamic component from an incompressible flow model and an acoustical component, which is the solution of Eq. (12).

From the boundary element solution[20] of Eq. (12), the first resolved acoustic component of wall pressure then must be summed up with hydrodynamic pressure to give the total dipole source of Eq. (6). The classic formulation of Eq. (6) is used to obtain the acoustic field at the listener's position in the propagation region.

3. VALIDATION

The acoustic pressure calculated by the hybrid approach is validated against the analytical solution of the tailored Green's function.[19,21] The benchmark is a two-dimensional case of two filament vortices spinning within an infinite duct with height h. Through the simplicity of this test cast, both the flow and acoustic field along the duct can be derived from an analytical calculation. The sound prediction is obtained in two ways. The first approach consists of using the tailored Green's function built from the duct mode.[7] This approach provides the reference solution. The second method is our hybrid formulation, using a free-field Green's function, which it is the Hankel function of the first kind. The quadrupole source terms and unsteady hydrodynamic pressure are obtained from an analytical derivation from the vortex model. An incompressible flow description is derived from the Biot-Savart induction of the two spinning vortices by a distance of $h/2$. The relevant Mach number is 0.5 with a speed of sound of $c_0 = 340$ ms^{-1}. The velocity formula of the computational domain and the trajectories of the two vortices and unsteady pressure distribution at the wall are formulated in Appendix A.

The simplicity of this configuration allows for the analytical solving of the 2-D Helmholtz equation:

$$\nabla^2 G_1 + k^2 G_1 = \delta(x - x_0)\delta(y - y_0). \tag{13}$$

With boundary condition $\partial G/\partial n = 0$, the 2-D tailored Green's function G_1 can be expressed as an infinite sum over the duct modes:

$$G_1(x, y|x', y') = \frac{i}{h}\sum_{n=0}^{\infty}\frac{1}{k_n}\cos\Big(\frac{n\pi y}{h}\Big)e^{\mp ik_n(x-x')}\cos\Big(\frac{n\pi y'}{h}\Big). \tag{14}$$

With $k_n = \big(k^2 - \mu_n^2\big)^{\frac{1}{2}}$, $\mu_n = n\pi y/h$ and the $-$ and $+$ sign correspond to waves propagating, respectively to the right and left from the source. Substituting the tailored Green's function Eq. (14) into Eq. (13) yields the acoustic pressure:

$$\begin{aligned} P_a(x, y, \omega) &= \iiint_V T_{ij}\frac{\partial^2 G}{\partial x'\partial y'}\,dx'dy' \\ &= \frac{1}{h}\iint_{\partial V}\sum_{n-0}^{\infty} e^{\mp ik_n(x-x')}\cos\Big(\frac{n\pi y}{h}\Big) \\ &\quad\Big\{-ik_n\cos\Big(\frac{n\pi y'}{h}\Big)T_{11}(x', y', \omega) - \\ &\quad\frac{i\pi^2 n^2}{h^2 k_n}\cos\Big(\frac{n\pi y'}{h}\Big)T_{22}(x', y', \omega) \pm \\ &\quad\frac{2\pi n}{h}\sin\Big(\frac{n\pi y'}{h}\Big)T_{12}(x', y', \omega)\Big\}dx'dy'. \end{aligned} \tag{15}$$

The series is truncated beyond a sufficient number of evanescent modes. Equation (15) is an exact solution of the ducted vortex spinning problem.

The duct extends in the axial direction between $x/h = -5$ and 5, and has a unit height $h = 1$. The first cut-on frequency in the x-direction corresponds to the Helmholtz number $He = \pi$, and the second cut-on is 2π. An acoustical impedance boundary condition $Z = \rho_0 c_0$ at both ends of the duct is applied to have non-reflection boundary conditions at the hybrid numerical method in order to permit comparison with the infinite duct reference solution. Figure 1 shows the real acoustic pressure at the upper wall from the hybrid and exact numerical solutions at the Helmholtz number equal to $He = 2$. The hybrid method covers the results of the exact solution.

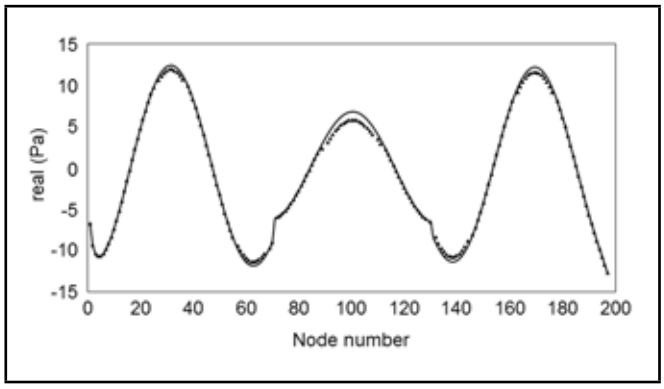

Figure 1. The real part of acoustical pressure at the upper wall of the duct, $He = 2$; ▲ exact solution; — hybrid method.

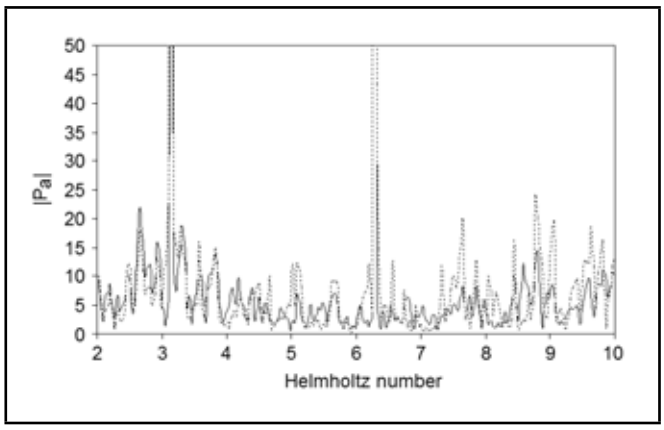

Figure 2. Acoustical pressure evaluated at a listener position $(x/h, y/h) = (2.025, 0.175)$. — exact solution; - - - hybrid method.

The acoustic pressure from the hybrid method and the analytical method are compared for frequencies covering the range of the Helmholtz number from 1 to 10. Figure 2 shows the acoustical pressure calculated from hybrid and exact methods at the coordinate of (2.025, 0.175). At frequencies below the first transverse duct mode, as shown in Fig. 1, the hybrid method results are very close to the results of the analytical solution. By increasing the frequency to above the frequency of the first and second transverse duct modes, the accuracy of the hybrid sound prediction method will begin to deteriorate as shown in Fig. 2. The acoustic pressure contours below and above the cut-on frequencies, and Helmholtz numbers of 2, 2.4, and 4.8 are presented respectively in Fig. 3, where the results from the hybrid method and the exact solution are compared.

Figure 1 and Fig. 3(a) are at $He = 2$, where the hybrid method is in excellent agreement with the results of the exact solution. However at $He = 2.4$, some difference can be observed, and at $He = 4.8$ the differences increase, but the comparison is still acceptable. Hence, by comparing the results of the hybrid method to that of the exact solution of this test

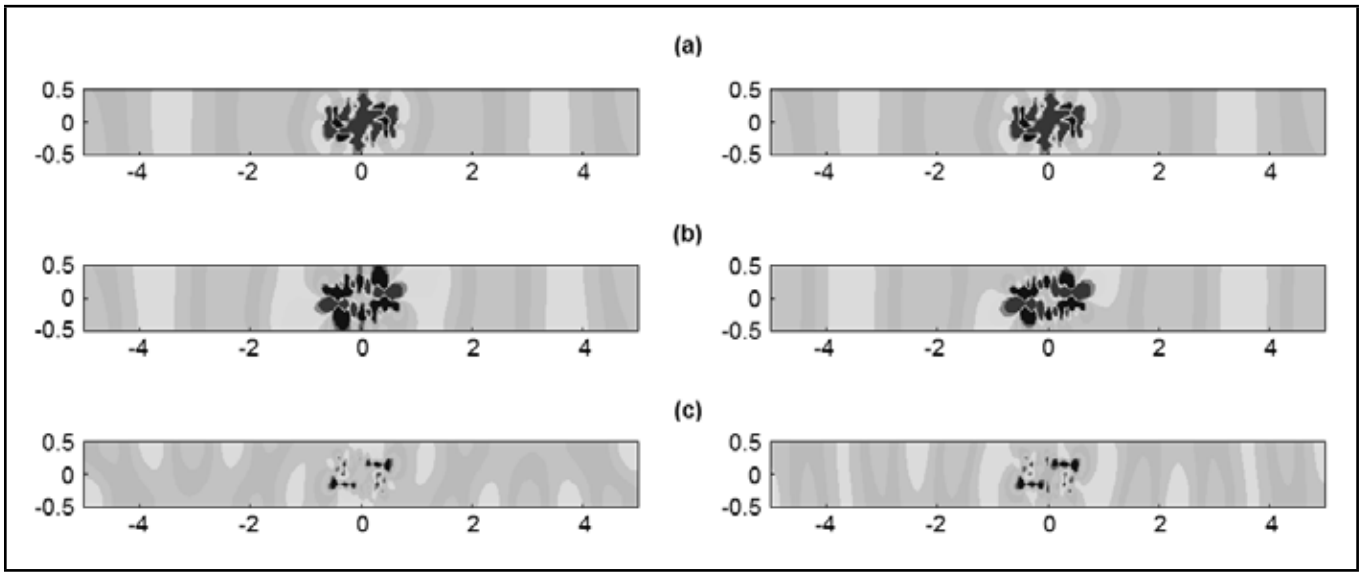

Figure 3. Imaginary part of acoustic pressure at Helmholtz number: (a) $He = 2$, (b), $He = 2.4$, (c) $He = 4.8$. Left column: hybrid method, right column: exact method; levels between -16 and 16.

case, the reliability of this hybrid method can be concluded. For industrial applications, the geometries and problems are sufficiently complicated so that the analytical formulation cannot be performed to derive an exact solution of the problems. Therefore, using the hybrid approach is forced. In this work, we utilize our hybrid solution of the sound wave equation for the prediction of sound generated by a diaphragm through a duct. Since the flow field is also quite complicated, a computational fluid dynamic is needed to simulate the flow through the diaphragm. In this way, we can compute the sound source terms needed in the acoustic calculations. In order to accurately predict the flow quantities, such as the velocities and pressure fluctuations, Large Eddy Simulation (LES) is the most feasible choice.

4. SOUND GENERATION

This section presents the applicability of the hybrid method to the computation of noise by a turbulent flow through a diaphragm in a duct at low Mach numbers. Direct noise computation for flow over this configuration was carried by Gloerfelt and Lafon.[15] The source fluctuations in the flow are first computed by a Large Eddy Simulation (LES) of an incompressible fluid with the Dynamic Smagorinsky Model,[22–24] and then they are fed to the following hybrid acoustical computation as input data.

4.1. Governing Equation

The flow field is computed with a three-dimensional incompressible Large Eddy Simulation (LES) using a finite-volume code to simulate the aerodynamic field. The underlying numerical scheme consists of a fully conservative second-order FV space discretization with a collocated arrangement of variables on a non-orthogonal grid. For the time discretization, an implicit second-order scheme is employed, while a nonlinear multi-grid scheme, in which the pressure correction method acts smoother on the different grid levels, is used for convergence acceleration. In LES, the flow field is decomposed into a large-scale or grid scale (GS) component and a sub-grid scale (SGS) component, given for a field variable $\phi = (\overline{\phi})_{\mathrm{GS}} + (\phi')_{\mathrm{SGS}}$.

The GS component is obtained by filtering the entire domain using a grid filter function. The filtering operation removes the SGS turbulence from the Navier-Stokes equation. The resulting governing equations are then solved directly for the GS turbulence motions, while the effect of the SGSs is computed using an SGS model, such as the classical Smagorinsky model used in this work.[22]

The governing equations of the LES are spatially filtered as:

$$\frac{\partial \overline{u}_i}{\partial x_i} = 0; \tag{16}$$

$$\frac{\partial \overline{u}_i}{\partial t} + \frac{\partial}{\partial x_j}\left(\overline{u}_i\overline{u}_j + \tau_{ij}\right) = -\frac{1}{\rho}\frac{\partial p}{\partial x_i} + \frac{\partial}{\partial x_j}\left\{\nu\left(\frac{\partial \overline{u}_i}{\partial x_j} + \frac{\partial \overline{u}_j}{\partial x_i}\right)\right\}; \tag{17}$$

where u and p are the grid-scale components, and ν is the kinematics' viscosity. The viscous stress tensor τ_{ij} is modelled as a Newtonian fluid $\tau_{ij} = 2\mu S_{ij}$, where μ is the dynamic molecular viscosity, and S_{ij} is the deviatoric part of the deformation stress tensor. The sub-grid scale (SGS) stress tensor τ_{ij} is defined by:

$$\tau_{ij} = \overline{u_i u_j} - \overline{u}_i\overline{u}_j. \tag{18}$$

The Smagorinsky closure is applied to the SGS stress τ_{ij}:

$$\tau_{ij} - \frac{1}{3}\delta_{ij}\tau_{kk} = -2\nu_{\mathrm{SGS}}\overline{S}_{ij}; \tag{19}$$

where $\nu_{\mathrm{SGS}} = (C_s\Delta)^2|\overline{S}|$, $|\overline{S}| = \sqrt{2\overline{S}_{ij}\overline{S}_{ij}}$, $\overline{S}_{ij} = \frac{1}{2}\left(\frac{\partial \overline{u}_i}{\partial x_j} + \frac{\partial \overline{u}_j}{\partial x_i}\right)$.

The quantity Δ is the size of the grid filter and C_s is the Smagorinsky coefficient that is computed with the Dynamic Smagorinsky Model (DSM) where modification by Lilly is

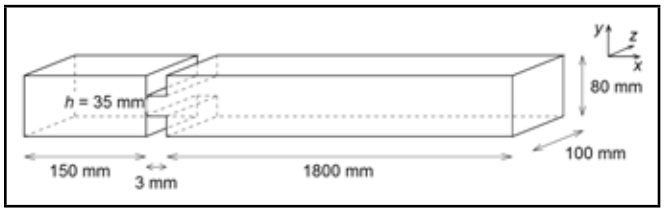

Figure 4. Computation domain.

used:

$$C_s = \frac{1}{2}\frac{\langle M_{ij}L_{ij}\rangle}{\langle M_{ij}L_{ij}\rangle}; \tag{20}$$

$$M_{ij} = \widetilde{\Delta}^2|\widetilde{\overline{S}}|\widetilde{\overline{S}}_{ij} - \overleftrightarrow{\Delta^2|\overline{S}|\overline{S}_{ij}}; \tag{21}$$

$$L_{ij} = \overleftrightarrow{\overline{u}_i\overline{u}_j} - \widetilde{\overline{u}}_i\widetilde{\overline{u}}_j. \tag{22}$$

The symbol '$\sim$' represents a test filtering operation where $\widetilde{\Delta}/\Delta \approx 2$ and '$\langle\,\rangle$' represent an averaging operation. The filter is the Laplacian operation.[25] The chosen configuration was shown in Fig. 4.

The cross-sectional area $h_c \times l_c = 80 \times 100$ mm^2. The slip-shaped aperture of the diaphragm has a height, $h = 35$ mm, and spans the transverse width of the duct. The mesh used is a non-uniform Cartesian grid with 813,500 cells. The diaphragm is located at the 42$^{\text{nd}}$ grid point in the x-direction and extends over 15 points horizontally and 19 points vertically. The duct length downstream the diaphragm is then at 1.8 m. The grid is refined near the rectangular aperture and then stretched with the rate of 6%. The grid in the y-direction is uniform over the diaphragm aperture with $\Delta y = 2$ mm. The mesh size in the span-wise z-direction is $\Delta z = 2$ mm. A CFL number of 0.9 and $\Delta x_{\text{min}} = 0.375$ mm near the rectangular aperture leads to a time step $\Delta t = \text{CFL} \times \Delta x_{\text{min}}/c_0 = 9.75 \times 10^{-7}$ s. Approximately 200,000 time steps (i.e. 0.2 s of physical time) are performed. The inlet velocity is 6 ms^{-1} and the Reynolds number based on the height of the diaphragm is $Re_h = 14000$. The Reynolds number based on the height of the duct is $Re_h = 33000$. The cut-off frequency according to a maximum mesh size of $\Delta x_{\text{max}} = 18$ mm at the outlet is about 2500 Hz.

The flow parameters used in the experimental setup[14] are $p_\infty = 10^5$ Pa, $\rho_\infty = 1.168$ kg/m^3, $c_\infty = 346.15$ m/s, which are the freestream pressure, density, and sound speed, respectively. The kinematic viscosity of the air is $\nu_\infty = 1.46 \times 10^{-5}$ m^2/s.

The component of the average velocities in Fig. 5 illustrates that the flow through the diaphragm can be separated into three regions: first, the uniform flow in the upstream duct, second, the jet-type flow emanating from the diaphragm where most acoustic energy is produced, and third, the uniform flow in the downstream duct segment after $x = 0.4$ m.

An asymmetric flow, in spite of the symmetric test section and symmetric inlet and outlet, called the Coanda effect[26] occurred in this case. An increase of velocity near one wall is accompanied with a decrease in the pressure, and then a pressure difference is established across the duct, this will maintain the asymmetry of the flow. This break in the symmetry can be associated to a pitchfork bifurcation. At lower Reynolds numbers, experiments and stability analyses show that a constricted channel has a unique symmetric solution below a prescribed

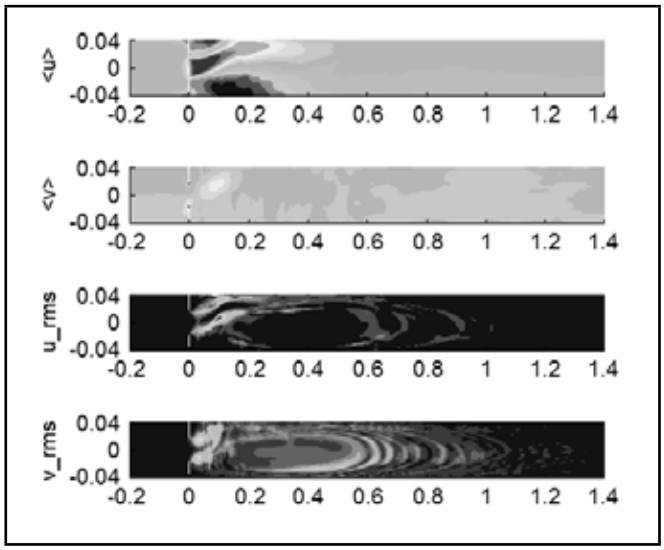

Figure 5. Average velocities $\overline{u}$ (levels between -10 and 20 m/s), $\overline{v}$ (levels between –7 and 7 m/s), u_{rms} (levels between 0 and 7 m/s), and v_{rms} (levels between 0 and 5 m/s).

Reynolds number, dependent on the contraction ratio and on the shape of the contraction. Above this critical Reynolds number, a pitchfork bifurcation results in a stable asymmetric flow. In the present simulation, the reattached point from the jet was about $x = 170$ mm at the upper wall. For comparison, an attachment point was near $x = 175$ mm in the work of Gloerfelt,[15] and an attachment point near $x = 150$ mm has been measured by particle image velocimetry (PIV) for the same geometry but with an incoming velocity of 14 m/s.[27] The choice of one side or the other is dependent on the subtle details of the initialization and transient history of the flow, which can place the flow in the domain of attraction of one or the other solutions in the multidimensional state space.

Power Spectral Densities (PSD) of vertical velocity at several locations in the upper shear layer are shown in Fig. 6. Data are evaluated for 2400 samples with a resolution of $\Delta f = 10.6$ Hz and a sampling rate of 25 kHz. The similarity parameter $\eta = (y - y_{0.5})/\delta_\theta$ shows that the mean stream-wise velocity profiles collapse for $\delta_\theta = 1$ mm instead of 0.7 mm[15] (See Fig. 7). This momentum thickness corresponds to the Strouhal number $St_{\delta_\theta} = f\delta_\theta/U_m$ equal to 0.019, close to the value of 0.017 for the most unstable frequency of a hyperbolic tangent velocity profile in the linear stability analysis.[28] In the similarity parameter, $y_{0.5}$ corresponds to $\overline{u} = 0.5U_m$ and U_m is 19 m/s at different longitudinal locations.

A peak centred around the Strouhal number 0.019 corresponding to the frequency 368 Hz is presented at $(x, y, z) = (0.04, 0.01, 0.0)$. This peak therefore indicates the presence of Kelvin-Helmholtz instability in the jet shear layer. Other points exhibit a more broadband content correlating to the periodic shedding and collapse of large-scale jet column instabilities.

4.2. Acoustic Simulation

At a 2-D slice of the duct, in the central plane of the diaphragm, the acoustic pressure was computed with the hybrid method. An acoustic computation is performed based on the acoustic source terms computed by LES simulation. Since

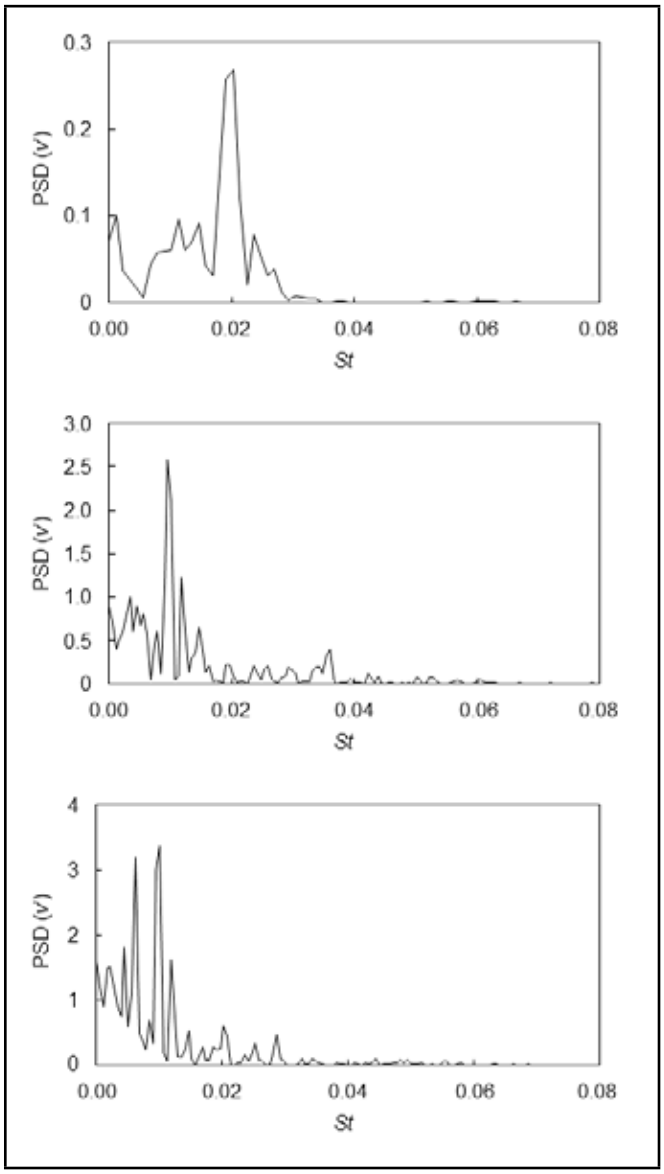

Figure 6. PSD of instantaneous vertical velocity fluctuations v' in $m^2/s^2/Hz$ vs. Strouhal number. From top to bottom, measured points located at $y = 0.01$, $z = 0$, $x = 0.04$, 0.12, and 0.16.

the flow field is simulated as three-dimensional, the acoustic source terms are calculated at the central surface of the duct in the xy plane. Then they are fed to the aeroacoustic solver code for the prediction of the noise generated by the turbulence flow inside a duct.

Spatial filtering[29] according to Eq. (23) is applied to the smooth source outgoing from the source region.

$$w(x) = \begin{cases} 1 & x \le x_1 \\ 1 - \frac{x - x_1}{L_1} & x > x_1 \end{cases}; \tag{23}$$

where x_1 is defined as the position from which the weighting is applied, and L_1 is the length of the subdomain where the weighting is applied.

The acoustic power is obtained from acoustic intensity I in the outlet section of the duct:

$$P_{\text{dB}} = 10 \log \left(\frac{I}{I_{\text{ref}}} \times S \right) \tag{24}$$

$$I = \frac{1}{\rho_0 C_0} \int \left[\text{PSD}(p') \right](f)\, df; \tag{25}$$

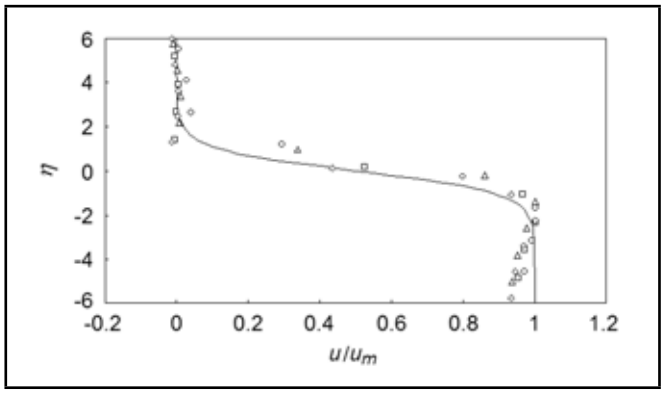

Figure 7. Mean streamwise velocity profiles. — hyperbolic tangent profile $(1-\tanh)/2$, □: $x = 1.5$ mm, ◇: $x = 3$ mm, △: $x = 6$ mm, ○: $x = 9.5$ mm.

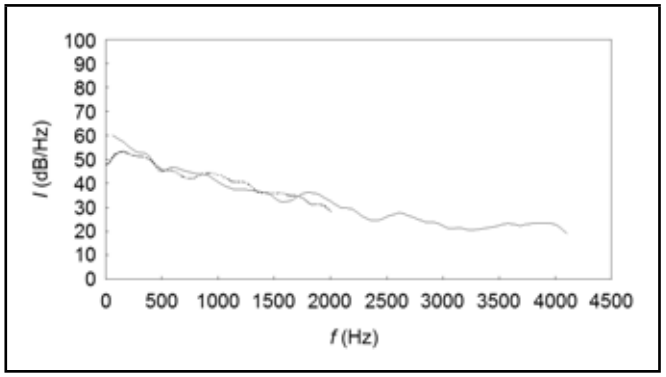

Figure 8. Power spectral at the outlet section. - - - DNC result,[15] — hybrid method.

where $I_{\text{ref}} = 10^{-12}$ Wm^2. At the inlet and outlet of the duct, the acoustic power is equal to 71.5 dB and 80.3 dB, respectively, which are close to the 69 dB and 78.8 dB from the DNC result of Gloerfelt and Lafon.[15] The total acoustic power is obtained by summing the acoustic intensities in the inlet and outlet sections. From our hybrid method of prediction of sound, the total radiated power 80.8 dB are calculated, that the value of 79 dB was referred in the work of Gloerfelt[15] and 79.3 dB in the empirical U^4 law based on the experimental work of Van Herpe.[14] The power acoustic result predicted by the hybrid method at the outlet boundary is compared with the DNC results in Fig. 8. The measured power spectrum is an average of ten samples. The DNC result only exists up to a frequency equal to 2000 Hz, which is lower than 2163 Hz, which is the cutting frequency associated to the duct height, D.

The acoustic pressure maps in the computational domain of the diaphragm are shown in Fig. 9. This shows the imaginary part of the acoustic pressure in the Fourier domain at above and below the first frequency of the cut-off mode in the ducted diaphragm. Figure 9(a) is at $f = 2000$ Hz, which is below the cut-off frequency, and Fig. 9(b) shows the imaginary part of the acoustic pressure at $f = 3500$ Hz, which is above the cut-off frequency. The change in the formation of the acoustic pressure map below and above the first transverse mode of the duct is clearly obvious at Fig. 9. The acoustic pressure contours corresponding to the imaginary part of the acoustic pressure contours for the straight duct were shown in Fig. 3.

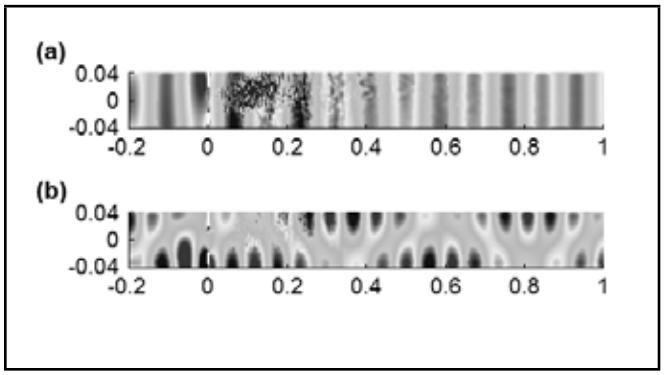

Figure 9. Imaginary part of acoustic pressure at: (a) $f = 2000$ Hz, (b) $f = 3500$ Hz. Levels between -0.002 and $+0.002$.

5. CONCLUSIONS

This work proposes a hybrid method that consists of an incompressible flow solver and boundary element method (BEM) for accurate prediction of sound generated by complex flows at low Mach numbers.

This approach was carefully validated for two spinning vortex filaments in an infinite two-dimensional duct. The results show excellent agreement between the hybrid method and the analytical acoustic field.

The proposed approach can predict the acoustic field in geometries of arbitrary extent and complexity, compact or non-compact, and high Helmholtz numbers.

As a demonstration of an engineering application, the sound generation over a diaphragm, which is applicable in heating, ventilating, and air-conditioning (HVAC) systems of automotive industries, was studied. The result of the hybrid approach was in good comparison with the DNC results in the frequency range adequately resolved by the numerical method.

REFERENCES

[1] Crighton, D. G. Computational aeroacoustics for low Mach number flows, *Computational Acoustics*, J. C. Hardin, M. Y. Hussaini (Eds.), Springer, New York, (1992), 50–68.

[2] Lighthill, M. J. On sound generated aerodynamically: I. General theory, *Proceedings of the Royal Society A*, **221**, 564–587, (1952).

[3] Curle, N. The influence of solid boundaries upon aerodynamic sound, *Proceedings of the Royal Society A*, **231**, 505–514, (1955).

[4] Ffowcs Williams, J. E., Hawkings, D. L. Sound generated by turbulence and surfaces in arbitrary motion, *Philosophical Transactions of the Royal Society A*, **264**, 321–342, (1969).

[5] Ryu, J., Cheong, C., Kim, S., Lee, S. Computation of internal aerodynamic noise from a quick-opening throttle valve using frequency-domain acoustic analogy, *Applied Acoustics*, **66**, 1278–1308, (2005).

[6] Yasuda, T., Wua, Ch., Nakagawa, N., Nagamura, K. Predictions and experimental studies of the tail pipe noise of an automotive muffler using a one dimensional CFD model, *Applied Acoustics*, **71**, 701–707, (2010).

[7] Davies, H. G., Ffowcs Williams, J. E. Aerodynamic sound generation in a pipe, *Journal of Fluid Mechanics*, **32**, 765–778, (1968).

[8] Nelson, P. A., Morfey, C. L. Aerodynamic sound production in low speed ducts, *Journal of Sound and Vibration*, **79**, 263–289, (1981).

[9] Peters, M. C. A. M., Hirschberg, A. Acoustically induced periodic vortex shedding at sharpedged open channel ends: Simple vortex models, *Journal of Sound and Vibration*, **161**, 281–299, (1993).

[10] Piellard, M., Bailly, C. Several computational aeroacoustics solutions for the ducted diaphragm at low Mach number, *16th AIAA/CEAS Aeroacoustic Conference*, AIAA paper 2010–3996, (2010).

[11] Venkatesham, B., Tiwari, M., Munjal, M. L. Prediction of breakout noise from a rectangular duct with compliant walls, *International Journal of Acoustics and Vibration*, **16** (4), 180–190, (2011).

[12] Mak, C. M. A prediction method for aerodynamic sound produced by multiple elements in air ducts, *Journal of Sound and Vibration*, **287**, 395–403, (2005).

[13] Han, N., Mak, C. M. Prediction of flow-generated noise produced by acoustic and aerodynamic interactions of multiple in-duct elements, *Applied Acoustics*, **69**, 566–573, (2008).

[14] Van Herp, F., Crighton, D. G., Lafon, P. Noise generation by turbulent flow in a duct obstructed by a diaphragm, *16th Aeroacoustic Conference*, AIAA paper 95–035, (1995).

[15] Gloerfelt, X., Lafon, P. Direct computation of the noise induced by a turbulent flow through a diaphragm in a duct at low Mach number, *Computers & Fluids*, **37**, 388–401, (2008).

[16] Schram, C. A boundary element extension of Curle's analogy for non-compact geometry at low Mach number, *Journal of Sound and Vibration*, **322**, 264–281, (2009).

[17] Khalighi, Y., Bodony, D. J. Improved near-wall accuracy for solution of the Helmholtz equation using the boundary element method, *CTR Annual Research Briefs*, 313–322, (2006).

[18] Gloerfelt, X., Perot, F., Bailly, C., Juve, D. Flow induced cylinder noise formulated as a diffraction problem for low Mach numbers, *Journal of Sound and Vibration*, **287**, 129–151, (2005).

[19] Schram, C., Anthoine, J., Hirschberg, A. Calculation of sound scattering using Curle's analogy for non-compact bodies, *11th AIAA/CEAS Aeroacoustic Conference*, AIAA paper 2005–2836, (2005).

[20] Von Estorff, O. *Boundary Elements in Acoustics: Advances and Applications*, WIT Press, (2000).

[21] Dowling, A. P., Ffowcs Williams, J. E. *Sound and Sources of Sound*, Ellis Horwood, (1983).

[22] Smagorinsky, J. General circulation experiments with the primitive equations I. The basic experiment, *Monthly Weather Review*, **91**, 99–164, (1963).

[23] Germano, M., Piomelli, U., Moin, P., Cabot, W. H. A dynamic subgrid-scale eddy viscosity model, *Physics of Fluids A*, **3**, 1760–1765, (1991).

[24] Lilly, D. K. A proposed modification of the Germano subgrid-scale closure method, *Physics of Fluids A*, **4**, 633–635, (1992).

[25] Kato, C., Yamade, Y., Wang, H., Guo, Y., Miyazawa, M., Takaishi, T., Yoshimura, S., Takano, Y. Numerical prediction of sound generated from flows with a low Mach number, *Computers & Fluids*, **36**, 53–68, (2007).

[26] Cherdron, W., Durst, F., Whitelaw, J. H. Asymmetric flows and instabilities in symmetric ducts with sudden expansion, *Journal of Fluid Mechanics*, **84**, 13–31, (1978).

[27] Crouzet, F., Lafon, P., Buchal, T., Laurence, D. Aerodynamic noise prediction in internal flows using LES and linear Euler equations, *8th AIAA/CEAS Aeroacoustic Conference & Exhibit*, AIAA paper 2002–2568, (2002).

[28] Danaila, I., Dusek, J., Anselmet, F. Coherent structures in a round, spatially evolving, unforced, homogeneous jet at low Reynolds numbers, *Physics of Fluids*, **9**, 3323–3342, (1997).

[29] Oberai, A. A., Roknaldin, F., Hughes, T. J. R. Computational procedures for determining structural-acoustic response due to hydrodynamic sources, *Computer Methods in Applied Mechanics and Engineering*, **190**, 345–361, (2000).

APPENDIX A

An incompressible flow description is obtained by integrating the reciprocal Biot-Savat induction of the two spinning vortices. The 2-D velocity field (u, v) induced by the two spinning vortex filaments is derived from the complex velocity potential: $u - iv = dw/dz$, where $z = x + iy$ is the complex coordinate. The complex velocity potential is $w(z) = \Phi + i\Psi$, where, Φ is the real velocity potential, and Ψ is the stream function. The resulting velocity potential due to the vortex n at the coordinate z_n is therefore:

$$w(z) = -\frac{i\Gamma}{2\pi}\Big\{ \log(z-z_n) - \log\big[z-(z_n+ih-2iy_1)\big] + \log\big[z-(z_n-2ih)\big] - \ldots - \log\big[z-(z_n-ih-2iy_1)\big] + \log\big[z-(z_n+2ih)\big] + \ldots \Big\}; \quad (A.1)$$

where $\Gamma = 85$ m^{2}s^{-1} is the circulation of each vortex. The duct height $h = 1$ m and the density $\rho = 1.225$ kg/m^3 are used to normalize the other quantities. The vortex filaments are initially placed over the duct axis, separated by a distance $d = h/2$. The relevant velocity and Mach number are $U = \Gamma/d$ and $M = \Gamma/(dc_0) = 0.5$ with a speed of sound $c_0 = 340$ m/s. The velocity field and the wall pressure inside the duct, induced by the two spinning vortex filaments, is performed in two steps. In the first step, the trajectories of the two vortices are integrated in time, by evaluating the velocity field induced at each vortex position by the other filament. The velocity field over the whole duct domain can then be obtained from the complex potential induced by the two vortices at each time step. The ODE function of Matlab was used to solve the trajectory of the two vortices by time-marching the equations for the position of each vortex filament m, induced by its potential and the potential due to the other vortex n, accounting for their images:

$$u_m = -\frac{\Gamma}{4h}\Bigg\{ \frac{\sin\left[\frac{\pi(y_m-y_n)}{h}\right]}{\cosh\left[\frac{\pi(x_m-x_n)}{h}\right] - \cos\left[\frac{\pi(y_m-y_n)}{h}\right]} + \frac{\sin\left[\frac{\pi(y_m+y_n)}{h}\right]}{\cosh\left[\frac{\pi(x_m-x_n)}{h}\right] + \cos\left[\frac{\pi(y_m+y_n)}{h}\right]} + \frac{\sin\left[\frac{2\pi y_m}{h}\right]}{1+\cos\left[\frac{2\pi y_m}{h}\right]} \Bigg\}; \quad (A.2)$$

$$v_m = -\frac{\Gamma}{4h}\Bigg\{ \frac{-\sinh\left[\frac{\pi(x_m-x_n)}{h}\right]}{\cosh\left[\frac{\pi(x_m-x_n)}{h}\right] - \cos\left[\frac{\pi(y_m-y_n)}{h}\right]} + \frac{\sinh\left[\frac{\pi(x_m-x_n)}{h}\right]}{\cosh\left[\frac{\pi(x_m-x_n)}{h}\right] + \cos\left[\frac{\pi(y_m+y_n)}{h}\right]} \Bigg\}; \quad (A.3)$$

for $m, n = 1, 2$ $(m \neq n)$. Integrating the unsteady Bernoulli equation:

$$\frac{\partial\Phi}{\partial t} + \frac{|V|^2}{2} + \int \frac{dp}{\rho} = 0. \quad (A.4)$$

Along each wall, yields the unsteady pressure distribution at the wall, which is related to the local value of the velocity potential and slip velocity:

$$p_w = -\rho\left(\frac{\partial\Phi_w}{\partial t} + \frac{u_m^2}{2}\right). \quad (A.5)$$

Once the kinematics of the vortices have been integrated, the velocity field at any point within the duct, except at the filament position, can be obtained from the summed velocity potentials of the vortices (A.1) with $n = 1, 2$. At every time step, velocity fields corresponding to the azimuthal velocity within a core size δ from the vortex filament considered as:

$$u = -\frac{\Gamma}{2\pi}\frac{y}{x^2+y^2+\delta^2}; \quad v = \frac{\Gamma}{2\pi}\frac{x}{x^2+y^2+\delta^2}. \quad (A.6)$$

The core sizes are kept small compared to the distance between the vortices to be consistent with filament-based mutual induction model, therefore it is considered to be equal to $\delta = h/50$.

About the Authors

Mouleeswaran Senthil Kumar is an associate professor in the Department of Production Engineering at PSG College of Technology, Coimbatore, India. He obtained his bachelors degree in mechanical engineering in 1994, his masters degree in engineering design in 1996, and his PhD in active suspension systems in 2008. He has about 17 years of teaching experience and one year of industrial experience. He has authored 75 journal papers and about 60 conference papers. He has been awarded with the ISTE-Anna University National Award for Best Academic 2013. He earlier received the ISTE award in 2006 for Best Research in the field of Machine Design and Vibration by a Young Teacher. He also received the AICTE Career Award for Particle Damping in 2009. He received the Outstanding Academician award from PSG College of Technology, India. He has completed several sponsored research projects worth about $1.5 million. He has been actively involved in many consultancy works in the fields of machine design and vibration control.

M. Vikram is currently doing his BE mechanical sandwich at PSG College of Technology, Coimbatore, Tamil Nadu, India. The author is a chairman of ASME, student section at PSG College of Technology. He has conducted a training programme on the design of automation systems for Ashok Leyland graduate engineering trainees. He has conducted many seminars for students on pneumatic circuit design, sensor interfacing using LabVIEW, etc. He has conducted a workshop on sensors & interfaces during the National Conference on Energy Efficient Mechanical System Design and Manufacturing held at PSG College of Technology. He has done an internship at TELCON Construction Equipment Company Limited, a joint venture of TATA-HITACHI in Jamshedpur, and he did a project on the productivity improvement of EX-1200 backhoe boom.

B. Pradeep is currently doing his BE mechanical sandwich at PSG College of Technology, Coimbatore, Tamil Nadu, India. He has conducted a training programme on the design of automation systems for Ashok Leyland graduate engineering trainees. The author has conducted a workshop on sensors & interfaces during the National Conference on Energy Efficient Mechanical System Design and Manufacturing held at PSG College Technology. He has done an internship at Goodrich Aerospace Services Pvt. Ltd, Bangalore. He has participated in the Contraption, and he won first place at Matrix 2010 at Kumaraguru College of Technology, Coimbatore and Srishti 2010 at PSG College of Technology, Coimbatore.

Pruthviraj Namdeo Chavan received his bachelors degree in mechanical engineering from Shivaji University, Kolhapur in 2009. He received his masters in machine design engineering from the Indian Institute of Technology, Hyderabad in 2012. He joined Mahindra and Mahindra Ltd. in 2012, and since then, he has been working in the field of noise and vibration at the Research and Development Centre, Chennai.

B. Venkatesham is an assistant professor at the Indian Institute of Technology, Hyderabad. He earned his Doctorate from the Indian Institute of Science, Bangalore, specializing in duct acoustics. He worked as a lead engineer for around 10 years at the General Electric Global Research Centre before joining IIT, Hyderabad. At GE, he worked on research projects and product development programs in industries spanning the fields of energy, appliances, business equipment, and locomotives. He has published eight papers in international journals, 21 conference papers, and has two patents in the area of engineering acoustics. His main research interests are in the areas of break-out noise modelling, acoustic-structural coupling systems, noise control engineering applications, and sound quality.

Cristóbal Ruiz-Cárcel studied Mechanical Engineering at Universidad Politcnica de Valencia (Spain, 2005-2010) and received his MSc Eng degree in the design of rotating machines from Cranfield University (UK) in 2011. Currently Cristbal is a PhD student and an early stage researcher in the Energy and Power Division at Cranfield University, working in the development and assessment of new algorithms for condition monitoring applied to large-scale industrial sites.

Enrique Hernani-Ros studied aeronautical engineering at Universidad Politcnica de Valencia (Spain, 2006-2012) and received his MSc Eng degree in the design of rotating machines from Cranfield University (UK) in 2012. In January 2013, he joined East Kilbride Engineering Services GmbH (EKES) as a stress engineer. EKES GmbH provides support to Rolls-Royce Deutschland in the design and production of modern civil and military turbine engines. His tasks include the lifting and stress analysis of high pressure compressor rotating components.

Yi Cao received his MSc degree in control engineering from the Zhejiang University, China in 1985 and his PhD degree in engineering from the University of Exeter, United Kingdom in 1996. He is a senior lecturer at the School of Engineering, Cranfield University. His research interests are in advanced process control, including plant-wide process control, nonlinear system identification, nonlinear model predictive control, and process monitoring.

Michael Corsar graduated from the University of Edinburgh in 2007 with an MEng in Mechanical Engineering. He followed this with an MSc from Cranfield University in 2008. He is a research fellow at Cranfield where his research interests are in turbo-machinery including tidal turbines, axial compressors, and combustion.

David Mba is a professor of rotating machines technology and a renowned expert on machine health monitoring, diagnostics, and prognostics. He is also actively involved with high-speed rotor dynamics (compressors, pumps, etc.), gearbox dynamics, and machine design. In the national and international asset management and condition monitoring community, Professor Mba has played a key role in the representation of the community worldwide– evident through his role as convenor for an ISO (International Standards Organisation) working group (ISO TC108 SC5 WG14). He has also contributed to several working groups within the British Standards Institute (BSI) and the British Institute of Non-Destructive Testing (BINDT) on condition monitoring and vibration analysis and diagnosis. Professor Mba has published over 200 journal and conference papers. In 2010, he was awarded the Ludwig Mond Prize in recognition of the best contribution to the progress of mechanical engineering of interest to the chemical industry.

About the Authors

Pramesh Chandra is an engineering professional specializing in the aerospace industry. Pramesh has a BEng (Hons) degree in aerospace systems engineering from Coventry University and an MSc degree in the design of rotating machines from Cranfield University. In his current role as project engineer at Moog Aircraft Group Wolverhampton (MAGWO), Pramesh is responsible for all the civil legacy projects at the Wolverhampton site, including actuation systems on Airbus A300, A330/A340, A380, BAE 146, Boeing 737, 767, 777, 787 aircrafts for project management, technical, and assembly and test aspects. In his previous roles as lead development engineer at MAGWO, Pramesh was responsible for all of the qualification testing programmes on the civil projects; these included Boeing 787-8, 787-9, and 787-10, and Airbus A380, A340, and A300. The role required verification & validation of customer requirements, preparing a qualification matrix, preparing test plans, compiling test reports, presenting technical data to customers, and developing test rigs. Pramesh is a Moog authorised test entry inspector.

A. Krishnamoorthy has obtained a BE in civil engineering, a ME in foundation engineering, and a PhD in Civil Engineering. Currently, he is working as professor in the Department of Civil Engineering, Manipal Institute of Technology, Manipal, Karnataka, India. He has about twenty-five years of undergraduate and post-graduate teaching experience and about tweny years of research experience. He pas published about thirty papers in journals. His areas of research include vibration isolation techniques for bridges and building structures, fluid-structure interaction analysis, soil-structure interaction analysis, and the numerical modelling of soil using the finite element method for non-linear and consolidation analysis. He has supervised many post-graduate theses as well three PhD theses.

Erhan Sancak grew up in stanbul,Turkey. He studied at the Afyon Kocatepe University Department of Textile Engineering for four years, graduating in 2001. He completed his PhD at Marmara University in 2013 where he also completed his post-graduate studies in 2004. He has been working as a research assistant at Marmara University since 2002.

Akira Ikuta received his BE and ME degrees from Kyushu Institute of Technology in 1976 and 1978, respectively, and he received his DEng degree from Hiroshima University in 1981. After being a research associate of electrical engineering at Hiroshima University and an assistant professor of mechanical systems engineering of Kinki University, he is now a professor in the Department of Management Information Systems, Prefectural University of Hiroshima. His research interests include digital signal information processing and wave motion environment (sound, vibration, and electromagnetic waves). He is on the editorial board of *Advances in Acoustics and Vibration*.

Hisako Orimoto received her BSc degree from Hiroshima Prefectural Womens University in 2003, her MSc degree from Prefectural University of Hiroshima in 2008, and her DEng degree from Hiroshima University in 2009. After being a system engineer of the System Development Division, NTT DATA Chugoku Co. and a research associate of Hiroshima National College of Maritime Technology, she is now an assistant professor in the Department of Management Information Systems, Prefectural University of Hiroshima. Her research interests include digital signal information processing and data processing.

Nazmul Siddique obtained his Dipl.-Ing degree from Dresden University of Technology, Germany in cybernetics and automation engineering in 1989. He obtained his MSc Eng degree in computer science from Bangladesh University of Engineering and Technology (BUET) in 1995. He received his PhD degree in intelligent control from the Department of Automatic Control and Systems Engineering, University of Sheffield, England in 2003. He has been a lecturer in the School of Computing and Intelligent Systems, University of Ulster Magee Campus, UK since 2001. He has published over 120 research papers in the broad area of cybernetics, intelligent control, computational intelligence, and robotics including three books and seven book chapters. He is the editor-in-chief of the *International Journal of Automation and Control Engineering*, editor of the *Journal of Behavioural Robotics*, associate editor of *Engineering Letters*, and also on the editorial advisory board of the *International Journal of Neural Systems*. He is a senior member of the IEEE, and a member of the executive committee of IEEE SMC UK-RI Chapter.

Liam Maguire received MEng and PhD degrees in electrical and electronic engineering from the Queens University of Belfast in 1988 and 1991. He is a professor and currently Head of the School of Computing and Intelligent Systems at the University of Ulster. He is also director of the Intelligent Systems Research Centre which encompasses the research activities of approximately 100 researchers. His research interests are in developing new bio-inspired intelligent systems and the application of existing intelligent techniques. He is the author of over 200 research papers including 70 journal papers. He has an established track record of securing research funding and has also supervised 15 PhD and 3 MPhil students to completion.

Mehran Tadjfar has beenan associate professor of aerospace engineering at Amirkabir University of Technology (Tehran Polytechnic) from 2004 to present. He received his BS degree from Northeastern University (1982), his MS degree from Case Western Reserve University (1985), and his PhD in aerospace engineering from The Ohio State University. He worked at NASA Ames Research Centre from 1990 to 1994. He was an assistant professor at Amirkabir University of Technology from 1994 to 1999. He worked at RIKEN Research Center in Wako, Japan from 1999–2004. He has worked in many areas of fluid mechanics including: UAV aerodynamics, transition and turbulence, aeroacoustics, and biological flows. He can be contacted at mtadjfar@aut.ac.ir.

Morteza Bayati is a PhD student of aerospace engineering at Amirkabir University of Technology. He received his BS degree from Amirkabir University (2004) and his MS degree from Sharif University (2006). He has worked in the areas of aeroacoustics and aerodynamics. He can be contacted at mbayati@aut.ac.ir

Adaptive Feed-Forward Control of Low Frequency Interior Noise

By: Thomas Kletschkowski
Springer, 2012, 330 p., 182 illus. (116 in color), Hardcover
Series: Intelligent Systems, Control and Automation: Science and Engineering, Vol. 56
ISBN 978-94-007-2536-2
Price: US $209

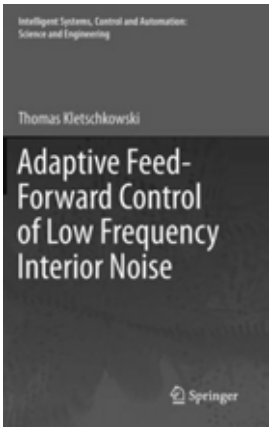

The book *Adaptive Feed-Forward Control of Low Frequency Interior Noise* by Thomas Kletschkowski presents a comprehensive and detailed view on adaptive techniques for interior active noise reduction. The book provides an excellent collection of references for the background sciences of active noise control (ANC), including the fundamental concepts of mechanics, acoustics, and signal processing. Contents span from theories and mathematical formulations of noise control to detailed design and implementation of existing ANC systems. Most practical examples address air-cabin noise issues, but the author provides formal generalization and modelling, which enables the application in any interior space. Although the topics are developed starting from basic concepts, such as the definition of signals and acoustic field equations, the reader is expected to be familiar at the academic or professional level with the relevant backgrounds. The book presents a "mechatronic" perspective on ANC, which considers the enclosed air-filled volume, the microphones, the loudspeakers, and the digital signal processing as components of a single system. The background knowledge enables the author to introduce a generic and cross-domain methodology for the design of ANC. The good organization of the contents across chapters facilitates the reading. Moreover, the introduction of new topics is generally well motivated and connected with the previous sections.

The first part of the book provides the reader with a generic introduction to the problem of noise control, detailing a mechanical formalization of active structural acoustic control (ASAC), active vibration control (AVC), and active noise control (ANC) for the cabin of a propeller-driven aircraft. These approaches are compared thereafter, while the benefits of ANC are highlighted. This section of the book is relatively short. Additional application examples and models for comparing the benefits/limitations of ASAC, AVC, and ANC would be of interest to readers, especially for those less familiar with the spring-mass model used to represent the aircraft.

The second part of the book consists of a comprehensive and cross-disciplinary presentation of ANC. The mathematical formulation of the noise control methodologies is very detailed and progressively explained, accessible also to those readers lacking in the few required backgrounds. The introduction to the sensors and actuators for noise control is well explained, and it further contributes to the holistic character of the book. Practical considerations of microphones and loudspeakers are provided to readers involved in the real implementations of ANC systems. Starting with the optimal tonal control of broadband noise, the author derives algorithms for multichannel adaptive control for stochastic noise. The mathematical model of feed-forward control is scalable to an arbitrary number of input/output, and the algorithms are reduced to "DSP-friendly" notation. Noteworthy for real ANC design is the comparison of implementation, computational load, and real-time constraints for different adaptive algorithms (FxLMS, MfxLMS, FeLMS, FEFxLMS) illustrated in textual and graphical forms. Possible evaluation and control strategies are reviewed as well in this part of the book. The readability here is less smooth, especially in those sections with many formulae and references. Additional description of the key formulae along with their practical/physical relevance would definitely improve the accessibility of the presented contents.

Part three of the book presents a theory and practical methodology for ANC system design. The initial performance estimation is well introduced and motivated as a key design step before prototype implementation. The author summarizes and compares different estimation approaches and practical implementation variables, such as transducer placement and sampling frequencies. The aim here is to define cross-domain iterative and cooperative design between mechanical, electrical, and electronic engineers for obtaining a common and optimized conception design for ANC systems.

Finally, part four of the book reviews both the systematic design method and prototype implementation of five different types of ANC systems. The individual chapter goes into deep details of case specific challenges, and how these were addressed by designers with preliminary simulation and emulations. The feasibility study included in each chapter is of a particular interest. The description of the mechatronic design process is accurate and meticulous, and it also includes specifications on the hardware used in each context. The chapter is very readable and well balanced. Plenty of illustrations are provided to support the design, measurements, and evaluation results. Readers will appreciate how specific noise control issues are addressed in diverse scenarios. This part of the book can be seen as a tutorial on the design of interior adaptive feed-forward ANC.

We noticed a misspelling in this book. The method for numerical quadratic optimization is usually referred to in literature as "steepest *descent*" and not "steepest *decent*" (as in the book).

Stefano Fasciani, PhD
Nanyang Technological University, Singapore